

Accurate, Meshless Methods for Magneto-Hydrodynamics

Philip F. Hopkins¹* & Matthias J. Raives¹

¹TAPIR & The Walter Burke Institute for Theoretical Physics, Mailcode 350-17, California Institute of Technology, Pasadena, CA 91125, USA

Submitted to MNRAS, April, 2015

ABSTRACT

Recently, we developed and explored a pair of new, meshless finite-volume Lagrangian methods for hydrodynamics: the “meshless finite mass” (MFM) and “meshless finite volume” (MFV) methods; these capture many advantages of both smoothed-particle hydrodynamics (SPH) and grid-based or adaptive mesh-refinement (AMR) schemes. Here, we extend these to include ideal magneto-hydrodynamics (MHD). Similar to the hydro method, the MHD equations are second-order consistent and conservative. We augment these with a divergence-cleaning scheme, which maintains $\nabla \cdot \mathbf{B} \approx 0$ to high accuracy. We implement and test these in the code GIZMO, together with a state-of-the-art implementation of SPH MHD. We consider a large suite of test problems, and show that on all problems the new methods are competitive with moving-mesh and AMR schemes using constrained transport (CT) to ensure $\nabla \cdot \mathbf{B} = 0$. They are able to correctly capture the growth and structure of the magneto-rotational instability (MRI), the launching of magnetic jets in collapsing protostellar cores, and the structure of MHD turbulence, in some cases converging more rapidly than state-of-the-art AMR codes. Compared to “modern” SPH, the MFM/MFV methods exhibit proper convergence at fixed kernel neighbor number, dramatically reduced noise, divergence errors, & numerical diffusion, & sharper shock-capturing. Still, “modern” SPH is able to handle most of our test problems, at the cost of much larger kernels and some “by hand” adjustment of artificial diffusion parameters. Compared to non-moving meshes, the new, meshless methods here exhibit some enhanced “grid noise,” but reduce advection errors and numerical diffusion, easily include self-gravity and cosmological integration, feature velocity-independent numerical errors, and superior angular momentum conservation. As a result they converge more slowly on some problems (involving smooth, slowly-moving flows), but more rapidly on others (involving advection or rotation). In all cases, we confirm that divergence-cleaning (or constrained transport) beyond the simple Powell 8-wave approach is necessary, or else all methods we consider can systematically converge to incorrect (and often unphysical) answers, even at infinite resolution.

Key words: methods: numerical — hydrodynamics — instabilities — turbulence — cosmology: theory

1 INTRODUCTION: THE CHALLENGE OF EXISTING NUMERICAL METHODS

Magnetic fields are an essential component in astrophysical hydrodynamics, and for many astrophysical problems can be reasonably approximated by ideal (infinite conductivity) magnetohydrodynamics (MHD). The MHD equations are inherently nonlinear, however, and most problems require numerical simulations. But this poses unique challenges, especially for numerical methods which are Lagrangian (i.e. the mesh elements follow the fluid), rather than Eulerian (solved on a fixed grid).

In the simplest discretization, evolving the MHD equations in time will lead to a violation of the “divergence constraint” (the requirement that $\nabla \cdot \mathbf{B} = 0$). Unfortunately, this cannot simply be ignored or treated as a “standard” numerical error term which should converge away with increasing resolution, because certain errors introduced by a non-zero $\nabla \cdot \mathbf{B}$ are numerically unstable: they will eventually destroy the correct solution (even at infinite resolution) and/or produce unphysical results (e.g. negative pressures). Arguably the most elegant solution is the so-called “constrained transport” (CT) method of Evans & Hawley (1988), which maintains $\nabla \cdot \mathbf{B}$ to machine precision; however, while there is no obvious barrier *in principle* to implementing this in meshless and unstructured mesh methods (see recent developments by Mocz et al. 2014a), it has thus far only been practical to implement for real problems in regular, Cartesian grid (or adaptive-mesh refinement; AMR) codes. But for many problems in astrophysics, Lagrangian, mesh-free codes have other advantages: they minimize numerical diffusion and over-mixing, move with the fluid so automatically

provide enhanced resolution with the mass (in a continuous manner, which avoids low-order errors necessarily introduced by AMR refinement boundaries), couple simply and accurately to cosmological expansion and N -body gravity codes, easily handle high Mach numbers, conserve angular momentum and naturally handle orbiting disks without prior knowledge of the disk geometry, avoid “grid alignment” and carbuncle instabilities (where the grid imprints preferred directions on the gas), and feature errors which are independent of the fluid bulk velocity (so can converge more rapidly when the fluid moves).

A variety of approaches have been developed to deal with these errors. The simplest commonly-used method, the so-called “Powell 8-wave cleaning,” simply subtracts the unstable error terms resulting from a non-zero $\nabla \cdot \mathbf{B}$ from the equation of motion (Powell et al. 1999). This removes the more catastrophic numerical instabilities, but does *not* solve the convergence problem – many studies have shown that certain types of problems, treated with only this method, will simply converge to the wrong solution (Tóth 2000; Mignone & Tzeferacos 2010; Mocz et al. 2014a). And the subtraction necessarily violates momentum conservation, so one would ideally like the subtracted terms (the $\nabla \cdot \mathbf{B}$ values) to remain as small as possible. Therefore more sophisticated “cleaning” schemes have been developed, the most popular of which have been variants of the Dedner et al. (2002) method: this adds source terms which transport the divergence away (in waves) and then damp it. This has proven remarkably robust and stable.

However, applications of these techniques in Lagrangian codes in astrophysics have remained limited. The most popular Lagrangian method, smoothed-particle hydrodynamics (SPH), suffers from several well-known errors that make MHD uniquely challenging. The SPH equations are not consistent at any order (meaning

* E-mail:phopkins@caltech.edu

they contain the “E0” zeroth-order errors, which are independent of resolution; Morris 1996; Dilts 1999; Read et al. 2010); this introduces noise which converges away very slowly and causes particular problems for divergence-cleaning. Also, naive implementations of the equations are vulnerable to the tensile and particle pairing instabilities. And artificial diffusion terms, with ad-hoc parameters, are required in SPH to deal with discontinuous fluid quantities. As such, many previous implementations of MHD in SPH were unable to reproduce non-trivial field configurations, were extremely diffusive, or were simply unable to numerically converge; in turn key qualitative phenomena such as the magneto-rotational instability (MRI) and launching of magnetic jets could not be treated (see Swegle et al. 1995; Monaghan 2000; Børve et al. 2001; Maron & Howes 2003; Price & Rosswog 2006; Rosswog & Price 2007; Price & Bate 2008; Dolag & Stasyszyn 2009).

Recently, however, a number of breakthroughs have been made in Lagrangian hydrodynamics, with the popularization of moving-mesh and mesh-free finite-volume Godunov methods. Springel (2010); Duffell & MacFadyen (2011); Gaburov et al. (2012) have developed moving-mesh MHD codes, which capture many of the advantages of both AMR and SPH, using the Dedner et al. (2002) cleaning method. Meanwhile, Lanson & Vila (2008a,b); Gaburov & Nitadori (2011); Hopkins (2014) have developed a class of new, mesh-free finite volume methods which are both high-order consistent (convergent) and fully conservative. These are very similar to moving-mesh codes (in fact, Voronoi moving-meshes are technically a special case of the method). In Hopkins 2014, these are developed for hydrodynamics in the multi-method, hydrodynamics+gravity+cosmology code GIZMO, which is an extension of the N -body gravity and domain decomposition algorithms from GADGET-3 (Springel 2005) to include a variety of new hydrodynamic methods.¹ In Hopkins (2014), a huge range of test problems are considered, and it is shown that these also capture most of the advantages of AMR and SPH, while avoiding many of their disadvantages. Particularly important, these eliminate the low-order errors, numerical instabilities, and artificial diffusion terms which have plagued SPH. Gaburov & Nitadori (2011) considered a range of MHD test problems and found very encouraging preliminary results; they showed that these mesh-free methods could handle complicated non-linear problems like the MRI with accuracy comparable to state-of-the-art grid codes. Meanwhile, tremendous improvements have also been made in SPH (Ritchie & Thomas 2001; Price 2008; Wadsley et al. 2008; Cullen & Dehnen 2010; Read & Hayfield 2012; Saitoh & Makino 2013; Hopkins 2013; Tricco & Price 2012, 2013).

Therefore, in this paper, we extend the mesh-free MFM and MFV Lagrangian hydrodynamics in GIZMO to include MHD, and consider a systematic survey of a wide range of test problems, and compare state-of-the-art grid-based (AMR) codes, MFM, MFV, and SPH MHD methods, implemented in the same code. This includes problems such as the MRI and MHD jets which have been historically challenging. We show in all cases that the new mesh-free methods exhibit good convergence and stable behavior, and are able to capture all of the important behaviors, even at low resolu-

¹ A public version of this code, including the full MHD implementation used in this paper, is available at <http://www.tapir.caltech.edu/~phopkins/Site/GIZMO.html>. Users are encouraged to modify and extend the capabilities of this code; the development version of the code is available upon request from the author.

tion. On some problem classes, we show they converge faster than state-of-the-art AMR codes using CT.

2 NUMERICAL METHODOLOGY

2.1 Review of the New Meshless Methods

Paper I derives and describes the pure-hydrodynamic version of the numerical methods here in detail, including self-gravity and cosmological integration. This is almost entirely identical in MHD; therefore we will not repeat it. However we will very briefly review the new numerical methods.

The equations we solve are the standard finite-volume Godunov-type equations: the fundamental difference between our meshless methods and a moving-mesh is simply that the definition of the volume partition (how the volume is divided among different mesh-generating points or “cells/particles”) is distinct. The further difference between this and a fixed-grid code is, of course, that the mesh-generating points/cells move, and that their arrangement can be irregular (as opposed to a Cartesian grid).

In a frame moving with velocity $\mathbf{v}_{\text{frame}}$, the homogeneous Euler equations in ideal MHD (and pure hydrodynamics, which forms the special case $\mathbf{B} = 0$) can be written as a set of hyperbolic partial differential conservation equations of the form

$$\frac{\partial \mathbf{U}}{\partial t} + \nabla \cdot (\mathbf{F} - \mathbf{v}_{\text{frame}} \otimes \mathbf{U}) = \mathbf{S} \quad (1)$$

where $\nabla \cdot \mathbf{F}$ refers to the inner product between the gradient operator and tensor \mathbf{F} , \otimes is the outer product, \mathbf{U} is the “state vector” of conserved (in the absence of sources) variables, the tensor \mathbf{F} is the flux of conserved variables, and \mathbf{S} is the vector of source terms

$$\mathbf{U} = \begin{pmatrix} \rho \\ \rho \mathbf{v} \\ \rho e \\ \mathbf{B} \\ \rho \psi \end{pmatrix} \quad \mathbf{F} = \begin{pmatrix} \rho \mathbf{v} \\ \rho \mathbf{v} \otimes \mathbf{v} + P_T \mathcal{I} - \mathbf{B} \otimes \mathbf{B} \\ (\rho e + P_T) \mathbf{v} - (\mathbf{v} \cdot \mathbf{B}) \mathbf{B} \\ \mathbf{v} \otimes \mathbf{B} - \mathbf{B} \otimes \mathbf{v} \\ \rho \psi \mathbf{v} \end{pmatrix} \quad (2)$$

where ρ is mass density, $e = u + |\mathbf{B}|^2/2\rho + |\mathbf{v}|^2/2$ is the total specific energy (u the internal energy), $P_T = P + |\mathbf{B}|^2/2$ is the sum of thermal and magnetic pressures, and ψ is a scalar field defined below.

The meshless equations of motion are derived in Paper I in standard Galerkin fashion beginning from the integral form of the conservation laws, after multiplying Eq. 1 by a test function ϕ

$$0 = \int_{\Omega} \left(\frac{d\mathbf{U}}{dt} \phi - \mathbf{F} \cdot \nabla \phi - \mathbf{S} \phi \right) d\Omega + \int_{\partial\Omega} (\mathbf{F} \phi) \cdot \hat{\mathbf{n}}_{\partial\Omega} d\partial\Omega \quad (3)$$

Here the domain Ω is such that $d\Omega = d^{\nu} \mathbf{x} dt$, where ν is the number of spatial dimensions, $df/dt \equiv \partial f/\partial t + \mathbf{v}_{\text{frame}}(\mathbf{x}, t) \cdot \nabla f$ is the co-moving derivative of any function f , and $\hat{\mathbf{n}}_{\partial\Omega}$ is the normal vector to the surface $\partial\Omega$, and the test function is an arbitrary differentiable Lagrangian function.

To transform this into a *discrete* set of equations, must chose how to partition the volume (for the “averaging/integration” step). If we choose a uniform Cartesian grid between uniformly spaced points, then we will recover the standard Godunov-type finite-volume grid-based equations of motion (like that in ATHENA and many popular AMR codes). If we choose a Voronoi tessellation between moving mesh-generating points, we recover a moving-mesh method similar to AREPO. For the new methods in Paper I, we partition the volume according to a *continuous* weighting function f , such that the fraction of the differential volume $d^{\nu} \mathbf{x}$ at the point \mathbf{x}

associated with the mesh-generating point at $\mathbf{x} = \mathbf{x}_i$ is given by

$$f_i(\mathbf{x}) \equiv \frac{W(\mathbf{x} - \mathbf{x}_i, h(\mathbf{x}))}{\sum_j W(\mathbf{x} - \mathbf{x}_j, h(\mathbf{x}))} \quad (4)$$

Where W is any kernel/weight function and h is a “kernel length.” Note that this guarantees a “partition of unity” (the volume is perfectly divided into cell-volumes V_i), and leads to a Voronoi-like partition, but with slightly smoothed boundaries between cells (which leads to some advantages, and some disadvantages, compared to moving meshes, where the boundaries are strict step functions). In the limit where W goes to a delta function, the method becomes exactly a Voronoi-type moving-mesh method.²

This choice is combined with a second-order accurate moving-least squares matrix-based gradient operator, which has been utilized in many other methods (including grid-based codes; see Maron et al. 2012; Tiwari & Kuhnert 2003; Liu et al. 2005; Luo et al. 2008; Lanson & Vila 2008a,b; Mocz et al. 2014b). Eq. 3 can then be expanded and analytically integrated to yield a second-order accurate set of discrete evolution equations:

$$\frac{d}{dt}(V\mathbf{U})_i + \sum_j \tilde{\mathbf{F}}_{ij} \cdot \mathbf{A}_{ij} = (V\mathbf{S})_i \quad (5)$$

This is identical to the standard Godunov-type finite-volume equations. The term $V_i \mathbf{U}_i$ is simply the cell-volume integrated value of the conserved quantity to be carried with cell/particle i (e.g. the total mass $m_i = V_i \rho_i$, momentum, or energy associated with the cell i); its time rate of change is given by the sum of the fluxes $\tilde{\mathbf{F}}_{ij}$ into/out of an “effective face area” \mathbf{A}_{ij} , plus the volume-integrated source terms. The full mathematical derivation and expression for the \mathbf{A}_{ij} is given in Paper I (§ 2.1).

We then use a standard MUSCL-Hancock type scheme for finite-volume Godunov methods to solve Eq. 5. This is commonly used in grid and moving-mesh codes (van Leer 1984; Toro 1997; Teyssier 2002; Fromang et al. 2006; Mignone et al. 2007; Cunningham et al. 2009; Springel 2010); it involves a slope-limited linear reconstruction of face-centered quantities from each mesh generating point (cell “location”), with a first-order drift/predict step for evolution over half a timestep, and then the application of a Riemann solver to estimate the time-averaged inter-cell fluxes for the timestep. See Paper I (§ 2 and Appendices A & B) for details. The points then move with the center-of-mass gas velocity.

In Paper I, we derive two variants of this method and implement them in GIZMO. First, the meshless finite-volume (MFV) method. This solves the Riemann problem between cells assuming the effective faces move with the mean cell velocity; this is analogous to a moving-mesh code, and includes mass fluxes between cells. Second, the meshless finite-mass (MFM) method. This solves the Riemann problem assuming the face deforms in a fully Lagrangian fashion; in this case there are no mass fluxes. The two

² Here and throughout this paper, we will define the kernel size h_i at the location of cell/particle i as the effective cell side-length, based on the cell volume V_i . In 1D/2D/3D, this is $h_i = V_i$, $h_i = (V_i/\pi)^{1/2}$, $h_i = (3V_i/4\pi)^{1/3}$, respectively. The volume V_i is calculated directly from the neighbor positions defining the volume partition (see Paper I). This *exactly* reproduces the grid spacing if the particles are arranged in a Cartesian grid. Note that, in principle, $W(\mathbf{x}, h)$ can be non-zero at $|\mathbf{x}| > h$. In MFM/MFV methods this has *nothing* to do with the effective cell/particle volume/size (conserved quantities are *not* “smoothed” over the kernel, but only averaged inside the a single cell of volume V_i just like in a grid code), but instead reflects the size of the stencil (number of neighbor cells) between which fluxes are computed.

are formally identical up to a difference in the non-linear (second-order) error terms in the fluxes, provided the cells move with the gas velocity. In practice, each has some advantages and disadvantages, discussed below.

2.2 Code Modifications for MHD

Everything described above is identical in hydodynamics and MHD; and all details of the code (except those specifically described below) are unchanged from Paper I.

As usual for finite-volume Godunov schemes, we explicitly evolve the conservative variables $(V\mathbf{B})_i$ (integrated magnetic field over the volume partition corresponding to a mesh-generating point) and $(m\psi)_i = \int \rho\psi dV_i$; primitive variables and gradients are then constructed from these (e.g. $\mathbf{B}_i \equiv (V\mathbf{B})_i/V_i$ as in Paper I).

2.2.1 The Riemann Solver

As in Paper I, we solve the 1D, un-split Riemann problem in the rest-frame of the effective face between the cells. However we require a Riemann solver that allows $\mathbf{B} \neq 0$. Since in the hydro case we use the HLLC solver, here we adopt the widely-used HLLD solver (Toro 1999). This is accurate at the order required, and extremely well-tested (see e.g. Teyssier 2002; O’Shea et al. 2004; Miyoshi & Kusano 2005; Stone et al. 2008).

The frame motion is calculated for both the MFM and MFV methods as in Paper I. We emphasize that for our MFM method, it is *required* that we use a solver which explicitly includes the contact wave (i.e. the contact discontinuity, on either side of which mass is conserved). This is because in MFM we always solve the Riemann problem with frame moving exactly with the contact wave; attempting to simply find a frame where the mass flux vanishes in a simpler (such as the HLL or Rusanov) approximation leads to incorrect, and in many cases unphysical solutions.

2.2.2 Signal Velocities and Time-Stepping

As in Paper I, we limit timesteps with a standard local Courant-Fridrich-Levy (CFL) timestep criterion; in MHD we must replace the sound speed with the fast magnetosonic speed:

$$\Delta t_{\text{CFL},i} = 2C_{\text{CFL}} \frac{h_i}{|v_{\text{sig},i}|} \quad (6)$$

$$v_{\text{sig},i}^{\text{MAX}} = \text{MAX}_j \left[v_{\text{f},ij} + v_{\text{f},ji} - \text{MIN} \left(0, \frac{(\mathbf{v}_i - \mathbf{v}_j) \cdot (\mathbf{x}_i - \mathbf{x}_j)}{|\mathbf{x}_i - \mathbf{x}_j|} \right) \right] \quad (7)$$

$$(v_{\text{f},ij})^2 \equiv \frac{1}{2} \left[c_{s,i}^2 + v_{A,i}^2 + \sqrt{(c_{s,i}^2 + v_{A,i}^2)^2 - 4c_{s,i}^2 v_{A,i}^2 (\hat{\mathbf{B}}_i \cdot \hat{\mathbf{x}}_{ij})^2} \right] \quad (8)$$

Here $\mathbf{x}_{ij} \equiv \mathbf{x}_i - \mathbf{x}_j$ is the separation between two points, $\hat{\mathbf{x}}$ is the unit vector $\mathbf{x}/|\mathbf{x}|$, $c_{s,i}$ is the sound speed, v_A is the Alfvén speed, h_i is the effective cell size defined above, MAX_j refers to the maximum over all interacting neighbors j of i , and v_{sig} is the signal velocity (Whitehurst 1995; Monaghan 1997).

2.2.3 Divergence-Cleaning

Ideally, this would complete the method; but the above method cannot ensure the divergence constraint. To do this, we must add the

following source terms:

$$\mathbf{S} = \mathbf{S}_{\text{Powell}} + \mathbf{S}_{\text{Dedner}} \quad (9)$$

$$= -\nabla \cdot \mathbf{B} \begin{pmatrix} 0 \\ \mathbf{B} \\ \mathbf{v} \cdot \mathbf{B} \\ \mathbf{v} \\ 0 \end{pmatrix} - \begin{pmatrix} 0 \\ 0 \\ \mathbf{B} \cdot (\nabla \psi) \\ \nabla \psi \\ (\nabla \cdot \mathbf{B}) \rho c_h^2 + \rho \psi / \tau \end{pmatrix} \quad (10)$$

The first term ($\mathbf{S}_{\text{Powell}}$) represent the Powell et al. (1999) or “8-wave” cleaning, and subtracts the numerically unstable terms from non-zero $\nabla \cdot \mathbf{B}$. This is necessary to ensure numerical stability and Galilean invariance – most problems will crash or converge to incorrect solutions without this. The second term ($\mathbf{S}_{\text{Dedner}}$) follows the method of Dedner et al. (2002), who introduce a conservative scalar field ψ which transports divergence away from the source and damps it. This is necessary to keep $\nabla \cdot \mathbf{B}$ low, minimizing the resulting errors.

Following Dedner et al. (2002) and Gaburov & Nitadori (2011), it is straightforward to show that this leads to the following form for the discrete terms in our equation of motion (Eq. 5):³

$$(V\mathbf{S})_i = -(V\nabla \cdot \mathbf{B})_i^* \begin{pmatrix} 0 \\ \mathbf{B}_i \\ \mathbf{v}_i \cdot \mathbf{B}_i \\ \mathbf{v}_i \\ 0 \end{pmatrix} - \begin{pmatrix} 0 \\ 0 \\ \mathbf{B}_i \cdot (V\nabla \psi)_i^* \\ (V\nabla \psi)_i^* \\ (V\nabla \cdot \mathbf{B})_i^* \rho_i c_{h,i}^2 + (m\psi)_i / \tau_i \end{pmatrix} \quad (11)$$

$$(V\nabla \cdot \mathbf{B})_i^* \equiv -\sum_j \bar{B}'_{x,ij} |\mathbf{A}_{ij}| \quad (12)$$

$$(V\nabla \psi)_i^* \equiv -\sum_j \bar{\psi}_{ij} \mathbf{A}_{ij} \quad (13)$$

where the \bar{B}' and $\bar{\psi}$ terms are defined below.

We have some freedom to choose $c_{h,i}$ and τ_i . Following Tricco & Price (2012), we take $c_{h,i} = \sigma_h^{1/2} v_{\text{sig},i}^{\text{MAX}} / 2$, where $v_{\text{sig},i}^{\text{MAX}}$ is the maximum signal velocity as described above. The value $v_{\text{sig},i}^{\text{MAX}} / 2$ is close to the fast magnetosonic wave speed, but also accounts for supersonic cell approach velocities, which is critical for good behavior in highly supersonic compressions. We have experimented with variations in the dimensionless parameter σ_h , and find the best results for $\sigma_h = 1$ (values $\sigma_h \ll 1$ produce ineffective cleaning, values $\gg 1$ lead to numerical instability). We take $\tau_i = h_i / (\sigma_p c_{\tau,i})$ (where h_i

³ Eq. 9 is the continuum equation; we stress that we are *not* free to choose how we discretize it. To actually ensure numerical stability, the form of the $\nabla \cdot \mathbf{B}$ terms must exactly match those terms from our Riemann solver solution which are unstable (e.g. the tensile terms). Likewise, the divergence cleaning must act specifically to reduce $\nabla \cdot \mathbf{B}$ *defined in the same manner*, or it does not serve any useful purpose. It might be tempting, for example, to use the value of $\nabla \cdot \mathbf{B}$ calculated from our second-order accurate matrix gradient estimator for the Powell terms, or to construct a pair-wise symmetrized version of Eq. 11 which manifestly maintains momentum conservation. However, these will not actually eliminate the unstable terms, and we have confirmed that they lead to catastrophic errors in our tests.

is the effective cell length defined above).⁴ For $c_{\tau,i}$ (the damping speed), we have considered several choices, all of which give very similar results. These are detailed in Appendix C; our default choice is Eq. C6, which is closely related to the local fastest possible signal velocity. We have also experimented extensively with σ_p , and find a best compromise between stability and diffusivity for values $\sigma_p \sim 0.05 - 0.3$; we adopt $\sigma_p = 0.1$ as our default in all problems here.

We caution that the discrete source terms, particularly the Powell terms which subtract i -centered quantities, are not manifestly antisymmetric between cell pairs ij . This means that momentum and energy conservation in MHD are only accurate up to integration accuracy, times a term proportional to $\nabla \cdot \mathbf{B}$ (unlike in hydrodynamics, where conservation can be ensured at machine accuracy).⁵ Controlling $\nabla \cdot \mathbf{B}$ is critical to minimize these errors.

These source terms also modify the Riemann problem. When we perform the reconstruction to obtain the left and right states \mathbf{U}_L (j -side) and \mathbf{U}_R (i -side), we can define a convenient coordinate system where $\hat{\mathbf{A}}_{ij} = \mathbf{A}_{ij}$ (i.e. the x -axis is normal to the effective face between cells i and j). In this coordinate system, the normal-component of the B -fields B'_x , will in general not be equal. But equal values (i.e. non-zero $\nabla \cdot \mathbf{B}$ in the 1D problem) are required for a physical solution. Without divergence-cleaning (Powell-only), this is handled by simply replacing $B'_{x,L}$ and $B'_{x,R}$ with the mean value $\bar{B}'_{x,ij} \equiv (B'_{x,L} + B'_{x,R}) / 2$. Dedner et al. (2002) showed that with the source terms of Eq. 9, the infinitely-sharp discontinuity leads to a physical solution $B'_{x,L} \rightarrow B'_{x,R} \rightarrow \bar{B}'_{x,ij}$, $\psi_L \rightarrow \psi_R \rightarrow \bar{\psi}_{ij}$, in infinitesimally small time:

$$\bar{B}'_{x,ij} = \frac{1}{2} (B'_{x,L} + B'_{x,R}) + \frac{1}{2\tilde{c}_{h,ij}} (\psi_L - \psi_R) \quad (14)$$

$$\bar{\psi}_{ij} = \frac{1}{2} (\psi_L + \psi_R) + \frac{\tilde{c}_{h,ij}}{2} (B'_{x,L} - B'_{x,R}) \quad (15)$$

$$\tilde{c}_{h,ij} = \text{MAX}[v_{f,L}, v_{f,R}] \quad (16)$$

$$v_{f,L}^2 = \frac{1}{2} \left[c_{s,L}^2 + v_{A,L}^2 + \sqrt{(c_{s,L}^2 + v_{A,L}^2)^2 - 4c_{s,L}^2 B'_{x,L}^2 \rho_L} \right] \quad (17)$$

here $\tilde{c}_{h,ij}$ is the fastest wave speed *in the local 1D problem*, which can be computed only from the i and j values (it does not necessarily correspond to $c_{h,i}$ in Eq. 9 above).⁶ This is separable from the full Riemann solution. So, in the Riemann problem, we first update B'_x and ψ according to the above, *then* compute the full Riemann solution using the updated values (and usual $B'_{y,L,R}$ and $B'_{z,L,R}$). The flux of B'_x is then $\tilde{F}_{ij,B'_x} = v'_{x,\text{face}} \bar{B}'_{x,ij}$, where $v_{x,\text{face}}$ is the normal face velocity in the boosted frame (in which we solve the Riemann problem). Because ψ is advected with the fluid, we follow Gaburov & Nitadori (2011) and simply take the ψ flux to be $\tilde{F}_{ij,\psi} = \tilde{F}_{ij,\rho} \psi_L$

⁴ In timestepping, we update $(m\psi)_i$ for the τ_i term with the implicit solution $(m\psi)_i \propto \exp(-\Delta t_i / \tau_i)$; this allows us to take larger timesteps without numerical instability.

⁵ Some of the Dedner terms can be made anti-symmetric without destroying the numerical stability of the scheme; for example the ψ -flux correction described below, and the $(V\nabla \cdot \mathbf{B}) c_h^2$ term (by using a single wavespeed $c_{h,i} = c_h$ for the whole problem). However in all our tests the conservation errors from those terms are always sub-dominant to the error from the (inescapable) Powell $(V\nabla \cdot \mathbf{B})_i^* \mathbf{v}_i$ term (and all these errors vanish when $\nabla \cdot \mathbf{B} \rightarrow 0$). So we find the best overall conservation properties result from using the most accurate possible cleaning scheme, rather than a partially-conservative (but less accurate) cleaning.

⁶ We have also explored an alternative, two-wavespeed formulation of the \bar{B} and $\bar{\psi}$ terms, discussed in Appendix E. For all tests here, the difference is small.

for $\tilde{F}_{ij,\rho} > 0$, and $\tilde{F}_{ij,\psi} = \tilde{F}_{ij,\rho} \psi_R$ for $\tilde{F}_{ij,\rho} < 0$, where $\tilde{F}_{ij,\rho}$ is the mass flux (so this vanishes for our MFM method).⁷

The HLLD solver requires an initial guess for the left and right wavespeeds, to compute a solution. If we define v'_x as the normal-component of the reconstructed velocities, then we use $S_L = \text{MIN}[v'_{x,L}, v'_{x,R}] - \text{MAX}[v'_{f,L}, v'_{f,R}]$, where v'_{f} is the *updated* fast magnetosonic wavespeed using the updated normal $B'_{x,ij}$:

$$(v'_{f,L})^2 = \frac{1}{2} \left[c_{s,L}^2 + v_{A,L}^2 + \sqrt{(c_{s,L}^2 + v_{A,L}^2)^2 - 4c_{s,L}^2 B'_{x,ij}^2 / \rho_L} \right] \quad (18)$$

and $S_R = \text{MAX}[v'_{x,L}, v'_{x,R}] + \text{MAX}[v'_{f,L}, v'_{f,R}]$.⁸

Finally, as in Paper I, we solve the Riemann problem in the boosted frame $\mathbf{v}_{\text{frame}}$ corresponding to the mean motion of the quadrature point between mesh-generating points. We must therefore boost back to the simulation frame. The de-boosted fluxes for cells follow Paper I, for the hydro terms, but with the additional terms for \mathbf{B} (for the fluxes to cell- i):

$$(\tilde{\mathbf{F}}_{ij}(\mathbf{B}) \cdot \mathbf{A}_{ij})_i \rightarrow \tilde{\mathbf{F}}_{ij}(\mathbf{B}) \cdot \mathbf{A}_{ij} - \bar{B}'_{x,ij} |\mathbf{A}_{ij}| \mathbf{v}_{\text{frame}} \quad (19)$$

$$(\tilde{\mathbf{F}}_{ij}(e) \cdot \mathbf{A}_{ij})_i \rightarrow \tilde{\mathbf{F}}_{ij}(e) \cdot \mathbf{A}_{ij} - \bar{B}'_{x,ij} |\mathbf{A}_{ij}| \mathbf{v}_{\text{frame}} \cdot \mathbf{B}_i \quad (20)$$

The second equation just accounts for the energy flux associated with the corrected \mathbf{B} -flux.

2.3 The SPH MHD Implementation in GIZMO

As described in Paper I, GIZMO is a multi-method code: users can run with the MFM or MFV hydrodynamic methods, or SPH, if desired. We therefore update our SPH implementation to include MHD. The exact SPH equations are given in Appendix A.

Briefly, the non-magnetic implementation of SPH follows the “modern” P-SPH method developed in Hopkins (2013) and extended in Paper I. This includes state-of-art re-formulations of the SPH hydrodynamics equations to eliminate the known “surface tension” errors (Saitoh & Makino 2013; Hopkins 2013), Lagrangian-derived terms to account for variable smoothing lengths (Springel & Hernquist 2002), addition of artificial diffusion terms for thermal energy (Price 2008; Wadsley et al. 2008), higher-order switches for artificial diffusion terms to minimize unnecessary dissipation (Cullen & Dehnen 2010), the use of higher-order kernel functions to allow larger SPH neighbor numbers and reduce the zeroth-order SPH errors (Dehnen & Aly 2012), switches to prevent disparate time-stepping between neighbor particles (Saitoh & Makino 2009), introduction of more accurate matrix-based gradient estimators (García-Senz et al. 2012), and conservative, more accurate coupling of SPH to gravity (Price & Monaghan 2007; Barnes 2012).

⁷ We have experimented with using $\bar{\psi}_{ij}$ for the ψ -flux. However, this yields no improvement on any test problem, and the $(B'_{x,L} - B'_{x,R})$ term from $\bar{\psi}_{ij}$ can introduce numerical instability under some circumstances. Therefore we use the simpler ψ -flux.

⁸ The HLLD solver can fail in some very rare circumstances if “bad” guesses are used. We therefore check whether our first estimate produces a solution where the pressure is everywhere positive. If this fails, then we instead compute the Roe-averaged velocity v_{Roe} and fast magnetosonic speed c_{Roe} , and try $S_L = \text{MIN}[v'_{x,L} - v'_{f,L}, v_{\text{Roe}} - c_{\text{Roe}}]$ and $S_R = \text{MAX}[v'_{x,R} + v'_{f,R}, v_{\text{Roe}} + c_{\text{Roe}}]$. We then check again; if this fails (which does not occur in any test problem here) we test a Lax-Friedrich estimate ($S_L = -S_R$, with S_R from our first guess). If this somehow fails still, we go back and re-compute the interface using a piecewise-constant (first-order) approximation, then check the series of wavespeeds again. If this fails, the code exits with an error (this only occurs when unphysical values are input into the solver).

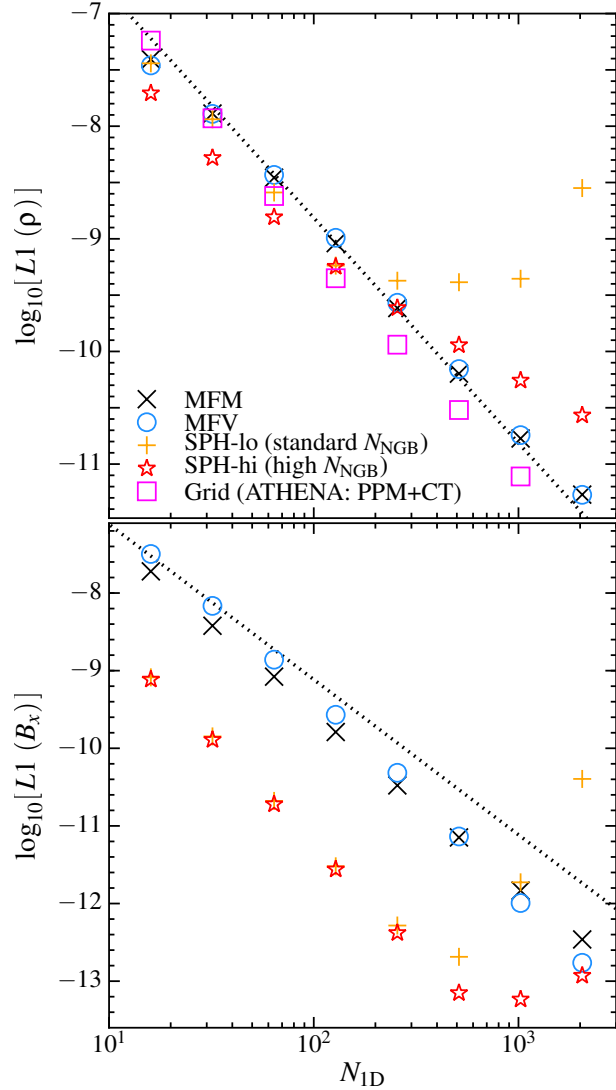


Figure 1. Linear magnetosonic wave test problem (see § 3.1). Here a traveling, one-dimensional fast magnetosonic wave is propagated one wavelength; we then define the L_1 norm as the mean absolute error relative to the known analytic solution in density (top) or magnetic field B_x (bottom; error here is equivalent to the numerical $\nabla \cdot \mathbf{B} \neq 0$ errors). We compare our new, meshless Lagrangian finite-volume Godunov methods (“meshless finite-mass” or MFM, and “meshless finite-volume” or MFV) from Paper I (see § 2.1), to the best current implementation of SPH MHD (see § 2.3), and to state of the art grid codes, here ATHENA run as a third-order PPM code using constrained transport (CT) to ensure $\nabla \cdot \mathbf{B} = 0$ to machine precision. Dotted line shows second-order convergence ($L_1 \propto N^{-2}$); MFM/MFV and grid/PPM methods converge at this rate, as expected. Convergence is also good ($L_1 \propto N^{-2.3}$) in MFM/MFV for the divergence errors ($\langle B_x \rangle = 1$, so these are fractionally very small). SPH shows some (slower) convergence until its known zeroth-order (E0) errors dominate; then errors flatten and start to increase with resolution. This can only be reduced in SPH by increasing the kernel size. “SPH-lo” (standard N_{NGB}) uses the equivalent of $N_{\text{NGB}} = 32$ in 3D (our default choice in all MFM/MFV runs). “SPH-hi” uses a 3D-equivalent $N_{\text{NGB}} = 120$.

The SPH MHD implementation combines these improvements to SPH with the MHD algorithms from the series of papers by Tricco & Price (2012, 2013). These introduce artificial diffusion for magnetic fields (artificial resistivity), with a similar “switch” to reduce unnecessary dissipation, and re-discretize the MHD equations from the particle Lagrangian included the Dedner et al. (2002)

and Powell et al. (1999) terms, so that the divergence cleaning actually acts on the tensile-unstable terms and these terms are properly subtracted (unlike most previous SPH-MHD implementations). We make some further improvements: following Price et al. (2012); Bate et al. (2014) and directly evolving the conserved quantities $(\mathbf{V}\mathbf{B})_i$ and $(m\psi)_i$, and slightly modifying the artificial resistivity terms to allow the method to capture cosmological field growth and MHD fluid-mixing instabilities.

3 TEST PROBLEMS

3.1 Linear Magnetosonic Waves: Testing Convergence

We begin by considering a simple linear one-dimensional magnetosonic wave.⁹ The problem is trivial, but since virtually all numerical schemes become first-order at discontinuities, smooth linear problems with known analytic solutions are necessary to measure formal convergence. Following Stone et al. (2008), we initialize a unit-length (in the x -direction), periodic domain, with polytropic $\gamma = 5/3$ gas, density $\rho = 1$, pressure $P = 1/\gamma$, and magnetic field $\mathbf{B}/\sqrt{4\pi} = (1, \sqrt{2}, 1/2)$. We add to this a traveling fast magnetosonic wave with amplitude $\delta\rho/\rho = 10^{-6}$, and allow the wave to propagate one wavelength; we then define the L1 error norm for the density (or any other variable) $L1(\rho) = N^{-1} \sum_i |\rho(x_i, t) - \rho(x_i, t=0)|$.

All methods we consider are able to evolve the wave. Fig. 1 plots the L1 norm for density (the velocity variables look similar), and B_x . In ρ , we see that both our MFM and MFV methods converge – as expected – with second-order accuracy. We compare to a state-of-the-art grid code, here ATHENA, run in the most accurate possible mode: PPM (formally a third-order reconstruction method), with the CTU integrator, and CT used to ensure $\nabla \cdot \mathbf{B} = 0$. Despite the higher order of ATHENA and the fact that it uses CT to ensure $\nabla \cdot \mathbf{B}$ errors remain at the machine-error level, the errors are nearly identical to our MFM/MFV results. The L1 norm for B_x directly measures the divergence errors; since we do not use CT, these are non-zero. However they are (1) very small, and (2) converge away appropriately – in fact, we see super-convergence ($L1 \propto N^{-2.3}$) for our MFM/MFV methods. As in Paper I, the convergence rate in all variables is *independent* of the kernel neighbor number in MFM/MFV: the choice only controls the *normalization* of the errors (larger neighbor numbers reduce noise, but increase diffusion). Based on our experiments in Paper I, we find roughly optimal results using a 3D-equivalent neighbor number $N_{\text{NGB}} = 32$ ($N_{\text{NGB}} \approx 4$ in 1D).

For SPH, we see slower convergence in ρ , but it is reasonable at low resolution; but at high-resolution, the SPH zeroth-order (E0) errors begin to dominate, and the errors flatten (or even increase!) with resolution. This is much more severe if we use a low neighbor number; going to higher-order kernels and higher neighbor numbers suppresses the errors, but they still eventually appear. For true convergence, N_{NGB} must increase with N , as is well-known (see Zhu et al. 2014, and references therein). Here we compare 3D-equivalent $N_{\text{NGB}} = 32$ (our default MFM/MFV choice used in *all* runs in this paper), henceforth referred to as “SPH-lo,” to 3D $N_{\text{NGB}} = 120$ (henceforth “SPH-hi”).

For more extensive convergence tests, see Paper I.

⁹ See <http://www.astro.princeton.edu/~jstone/Athena/tests/linear-waves/linear-waves.html>

3.2 Brio-Wu Shocktube: Capturing MHD Discontinuities & Controlling Noise

Next we consider the Brio & Wu (1988) shocktube; this tests whether the code can accurately represent uniquely MHD shocks, rarefactions, and contact discontinuities. We initialize a 2D periodic box (size $0 < x < 4$, $0 < y < 0.25$, with 896×56 cells/particles) with left-state $(\rho, v_x, v_y, v_z, B_x, B_y, B_z, P) = (1, 0, 0, 0, 0.75, 1, 0, 1)$, and right-state $(0.125, 0, 0, 0, -1, 0, 0.1)$, with $\gamma = 2$. Figs. 2-3 compare the results at time $t = 0.2$.

At this resolution, the CT-based grid code is well-converged, except for some post-shock “ringing” most visible in v_x . In MFM & MFV methods, the agreement with the exact solution is good at this resolution. At $4x$ higher-resolution, we find that the MFM/MFV results are nearly indistinguishable from the exact solution. At lower resolution, there is some “overshoot” at the density discontinuity, with MFM – this is discussed in detail in Paper I; it is mostly sensitive to the choice of slope-limiter (not the basic numerical method). The effects are much smaller in MFV, owing to mass fluxes allowing more sharply-captured density discontinuity. This also causes a small pressure “blip” in MFM at the contact discontinuity, but this converges away. Shock jumps and discontinuities are captured across ~ 2 cells/particles in each direction; comparable to high-order grid methods.

As an indicator of the $\nabla \cdot \mathbf{B}$ errors, we plot the dimensionless magnitude of $h_i |\nabla \cdot \mathbf{B}|_i / |\mathbf{B}|_i$; our divergence cleaning keeps this generally at low values ($\ll 10^{-4}$), except at the magnetic shocks (the large discontinuities in B_y); but even there, the *maximum* value is still $< 10^{-2}$. The good divergence-cleaning is also manifest in B_z ; at the same shocks, there are some jumps in B_z generated, but this is returned to the correct value across ~ 2 particles, and the magnitude of the deviations from the analytic $B_z = 0.75$ is typically at the sub-percent level, at this resolution.

With *no* divergence corrections whatsoever, the problem crashes. However, Fig. 3 shows that if we run with *only* the Powell terms in Eq. 9 (i.e. do not include the Dedner et al. (2002) divergence-cleaning and damping terms), this particular problem is not badly corrupted in most respects. As expected the divergence and deviation in B_x are larger. More seriously, though, a systematically incorrect jump in u appears, which *does not converge away* without divergence cleaning, even at $10x$ higher resolution in the x -direction. This problem occurs in MFM, MFV, and SPH.

SPH captures all the qualitative features. However, if we run with the same neighbor number (kernel size) as in our MFM/MFV methods, the noise is extremely large. This is shown in Fig. 3. If we instead use the equivalent of a 3D neighbor number of ~ 120 (as opposed to the ~ 32 we use for MFM/MFV), the noise is greatly reduced. However, there is still much larger noise and post-shock ringing (compared to MFM/MFV), and serious overshoot in the velocities at the rarefactions. The shock jump in u is captured on one side, but “decays” on the other side owing to a combination of artificial conductivity and resistivity acting where they should not. Divergence-cleaning works in SPH, but is much less effective, especially around the contact discontinuity, where the divergence errors reach $\sim 10\%$.

We have also compared the Ryu & Jones (1995) MHD shocktube, which exhibits all seven MHD waves simultaneously. The qualitative results and differences between methods are the same as in the Brio-Wu test, so we do not show it here.

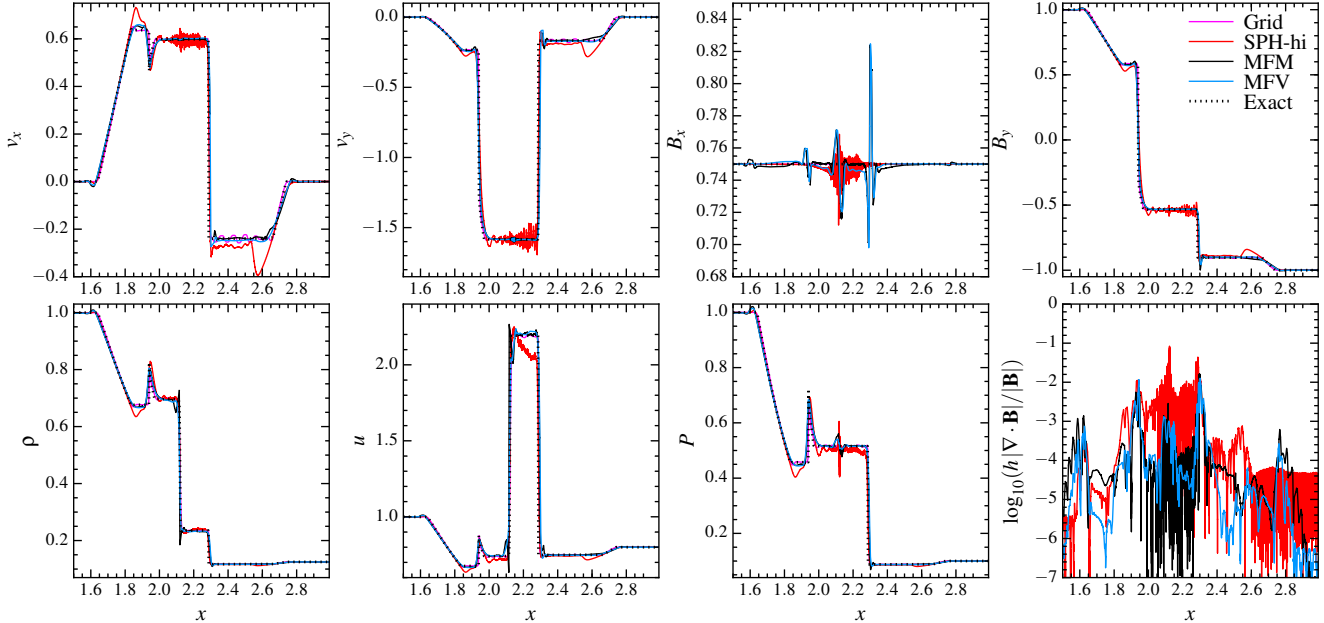


Figure 2. Brio-Wu shocktube (§ 3.2), at time $t = 0.2$; we compare the exact solution to that computed at finite resolution (plotted region contains ~ 300 elements across the x -direction) with different methods. High-order grid methods have converged well at this resolution, except for post-shock ringing in v_x . MFM/MFV methods also show good convergence; but at this resolution, MFM still shows some small ‘overshoot’ in the jumps at $x \approx 2.1, 2.3$ (more sensitive to our slope-limiter than the method itself), and both show some small (percent-level) errors in B_x owing to the $\nabla \cdot \mathbf{B}$ errors; however the fractional magnitude of $\nabla \cdot \mathbf{B}$ is controlled well by our cleaning scheme (typical errors $\sim 10^{-4}$ at this resolution; still below 10^{-2} at jumps). Discontinuities are well-captured across ~ 2 cells/particles in the linear direction. SPH (with high N_{NGB}) captures all the key features, but at this resolution shows much larger noise, large ($\sim 20\%$ -level) overshoots in v_x, v_y, B_y, P at rarefactions ($x \approx 1.9, 2.6$), suppression of internal energy around $x \approx 2.3$ (owing to more smeared-out dissipation from divergence-cleaning), and significantly larger $\nabla \cdot \mathbf{B}$ errors (reaching $\sim 10\%$); these converge away more slowly.

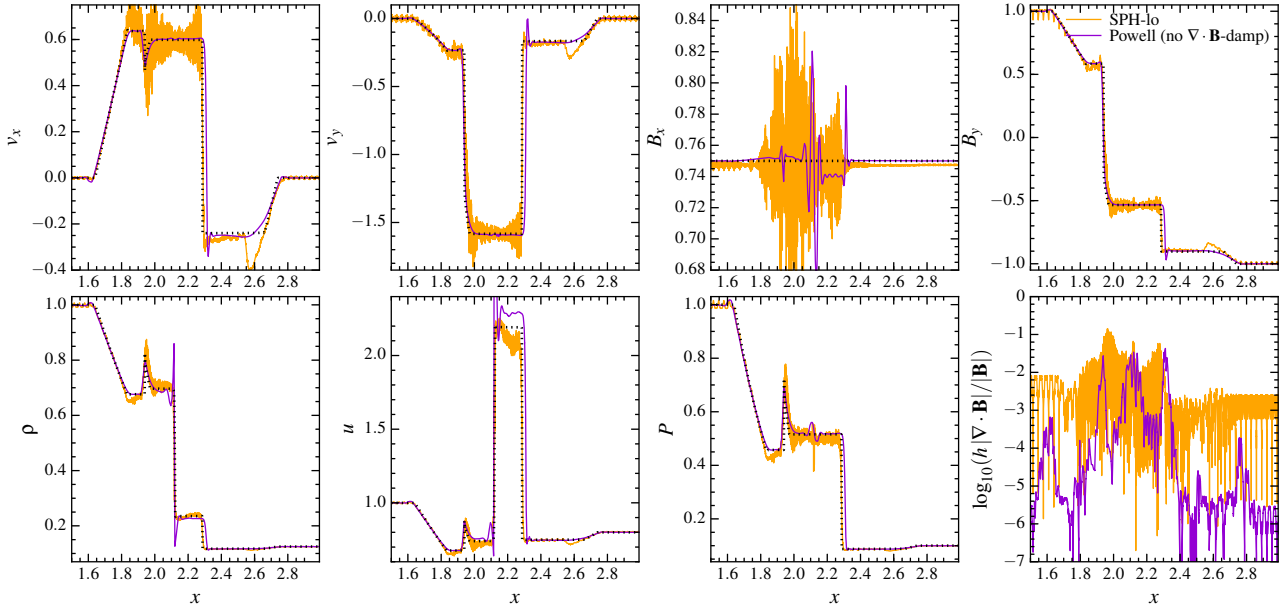


Figure 3. Brio-Wu shocktube, as Fig. 2, but in ‘bad’ formulations of MHD. If we consider MFM/MFV using only the Powell et al. (1999) source terms to stabilize MHD, but no Dedner et al. (2002) divergence-control (as has often been done in the literature), we obtain incorrect shock jumps; most noticeably in u & B_x . This error does not converge away. This is despite the fact that the formal $\nabla \cdot \mathbf{B}$ errors are still small; the key is the terms in the Dedner et al. (2002) scheme that enter the Riemann problem and act specifically at discontinuities. We also compare SPH run with the same (much lower) neighbor number as our MFM/MFV methods; here the noise is much larger (as expected), reaching order-unity fractional levels.

3.3 Toth Shocktube: The Critical Need for Divergence Cleaning Beyond Powell

Next we consider the Tóth (2000) shocktube; this tests super-sonic MHD shocks. It is particularly important because Mignone & Tzeferacos (2010) showed that a hyperbolic divergence-cleaning scheme such as the Dedner et al. (2002) method (or CT) is nec-

essary to get the correct shock jump conditions at any resolution, in grid-based methods. We initialize a 2D periodic box (size $0 < x < 4$, $0 < y < 0.25$, with 896×56 cells) with left-state $(\rho, v_x, v_y, v_z, B_x, B_y, B_z, P) = (1, 10, 0, 0, 5/\sqrt{4\pi}, 5/\sqrt{4\pi}, 0, 20)$, and right-state $(1, -10, 0, 0, 5/\sqrt{4\pi}, 5/\sqrt{4\pi}, 0, 1)$ and $\gamma = 5/3$.

Fig. 4 compares the results at time $t = 0.08$ (for clarity, we

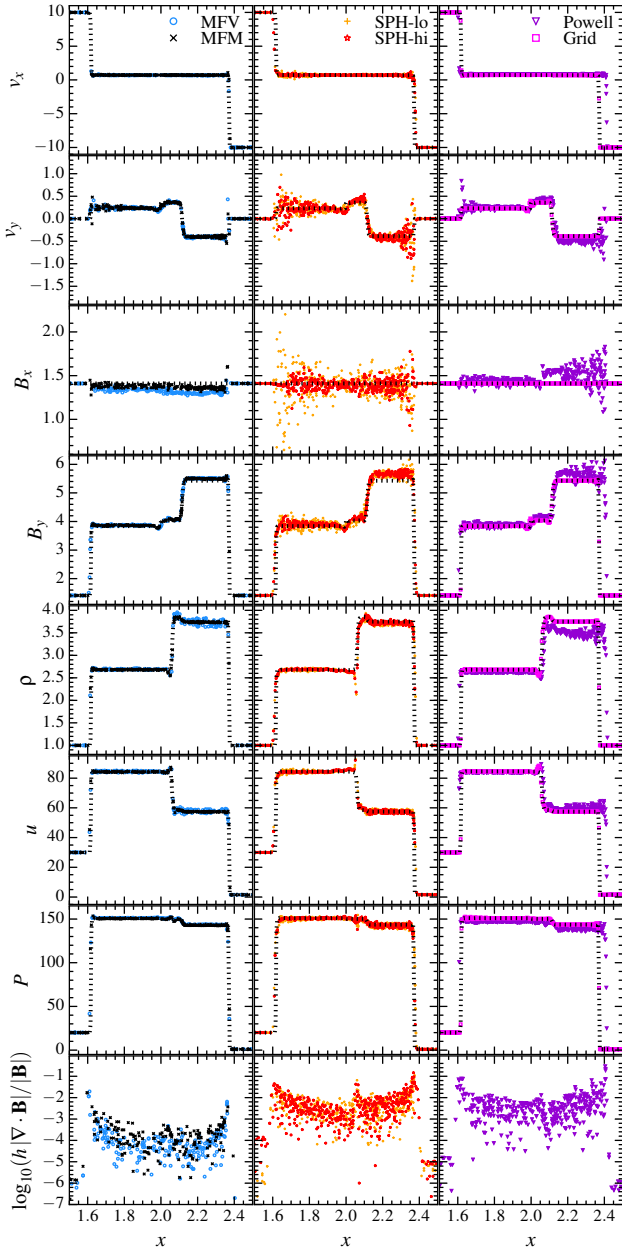


Figure 4. The Toth super-sonic shocktube (§ 3.3). The resolution is similar to the Brio-Wu test. MFM and grid/CT methods converge most rapidly to the exact solution (dotted), followed by MFV, which exhibits some residual noise in ρ around $x \sim 2.1 - 2.4$ at this resolution. MFM/MFV both control $\nabla \cdot \mathbf{B}$ errors well; the large B_y discontinuity introduces a small (percent-level) offset in B_x which converges away $\propto N^{-1}$ (nearly ideal), this is especially challenging for divergence-cleaning methods. SPH shows much larger (factor ~ 100) $\nabla \cdot \mathbf{B}$ errors, and noise; with some systematic offset in the B_y jump around $x \sim 2.1 - 2.4$ (since divergence cleaning is spread over several smoothing lengths), which converges slowly ($\propto N^{-0.4}$). The noise is reduced with larger neighbor number, but not eliminated. In all methods, the Powell scheme alone leads to systematically incorrect shock jumps in B_y and ρ ; as in Fig. 2, these do not converge.

plot only a randomly-chosen subset of 500 cells/particles for each method). Our MFM method does extremely well at this resolution; the only difference between it and high-resolution grid runs is a small ($\sim 1\%$ level) deviation in B_x introduced by $\nabla \cdot \mathbf{B}$ errors at this resolution, and some noise at the shock in the small v_y . The $\nabla \cdot \mathbf{B}$ errors are generally extremely small, $\sim 1\%$ at super-sonic shocks and $\sim 10^{-4}$ elsewhere. MFV is similar, although there is substan-

tially more noise at the same resolution in ρ and u in the post-shock region; this is seen in pure hydro in Paper I and in Gaburov & Nitadori (2011); the larger noise translates to slightly larger $\nabla \cdot \mathbf{B}$ errors at shocks, hence slower convergence in B_x . Both MFM & MFV are indistinguishable from the exact solution at 10x larger resolution in the x -direction.

However, with the Powell-only (no divergence-cleaning) mode, we see that the shock is in the wrong place! The shock jump is systematically wrong in ρ , P and B_y , and this leads to it being in the wrong place over time. Again, this appears even at infinite resolution. The noise, especially in B_x , is also much larger, and $\nabla \cdot \mathbf{B}$ errors, as expected, are factor ~ 100 larger.

In SPH, the noise is much larger, even with much larger 3D-equivalent $N_{\text{NGB}} = 120$. This is especially noticeable in v_y , B_x , and B_y . In B_y , the shock jump is also systematically over-estimated by $\sim 2 - 5\%$, owing to the much larger ($\sim 10 - 30\%$) $\nabla \cdot \mathbf{B}$ errors at the shock jump. As discussed below (§ 5), in SPH, divergence-cleaning cannot act over smaller scales than a few smoothing lengths, so the method has difficulty controlling the errors seen in the Powell-only case. The divergence errors are systematically larger by factors $\sim 10 - 100$. With $N_{\text{NGB}} = 32$ as in our MFM/MFV methods, the noise is yet larger (order-unity fractional noise in B_x , v_y).

3.4 Advection of a Field Loop: Minimizing Numerical Diffusion

The next test is a standard test of advection errors and numerical dissipation. We initialize a periodic 2D domain: inside a circle of $R = \sqrt{x^2 + y^2} < R_0 = 0.3$ about the origin, we set $(\rho, B_x, B_y) = (2, B_0 y/R, -B_0 x/R)$ with $B_0 = 10^{-3}$. Outside the circle $(\rho, B_x, B_y) = (1, 0, 0)$, and everywhere $(P, v_x, v_y, v_z, B_z) = (1, 2, 1/2, 0, 0)$; this is an equilibrium configuration that should simply be advected. In Fig. 5, we plot images of the magnetic energy density. In Fig. 6, we plot the total magnetic energy in the box as a function of time (which should remain constant at its initial value).

Advection of any configuration not perfectly aligned with the grid is challenging in grid codes; here the loop is continuously diffused away, at a rate that increases rapidly at lower resolution. In Lagrangian methods, on the other hand, stable configurations with bulk advection should be advected perfectly. In Paper I, we demonstrate that our MFM & MFV methods can advect arbitrary pressure-equilibrium hydrodynamic configurations (including arbitrary scalar quantities) to within machine accuracy. However, here the introduction of the divergence-cleaning source terms leads to some initial diffusion of \mathbf{B} in MFM/MFV. But we clearly still see the benefit of a Lagrangian method: convergence is much faster than in fixed-grid codes (even using CT); the dissipation in our 256^2 simulation with MFM/MFV is approximately equivalent to that in ATHENA at 1024^2 . In the image, we see slightly more noise; this is the expected ‘grid noise’ which is higher in meshless methods, but the diffusion is less (in particular, the ‘hole’ which appears at the center owing to numerical resistivity is minimized).

If we use Powell-only divergence subtraction, the conservation errors associated with non-zero $\nabla \cdot \mathbf{B}$ can actually lead to non-linear growth of \mathbf{B} , such that the total magnetic energy increases! The growth in this case is nearly resolution-independent, since it is sourced around the sharp discontinuity in the field at the edge of the loop. By the end of the simulation, the total magnetic energy in the Powell-only run has increased $\sim 50\%$. The noise and asymmetry in the image have grown severely.

In SPH, there is an initial, brief but unphysical growth in $|\mathbf{B}|^2$; this comes from the divergence-cleaning being less effective

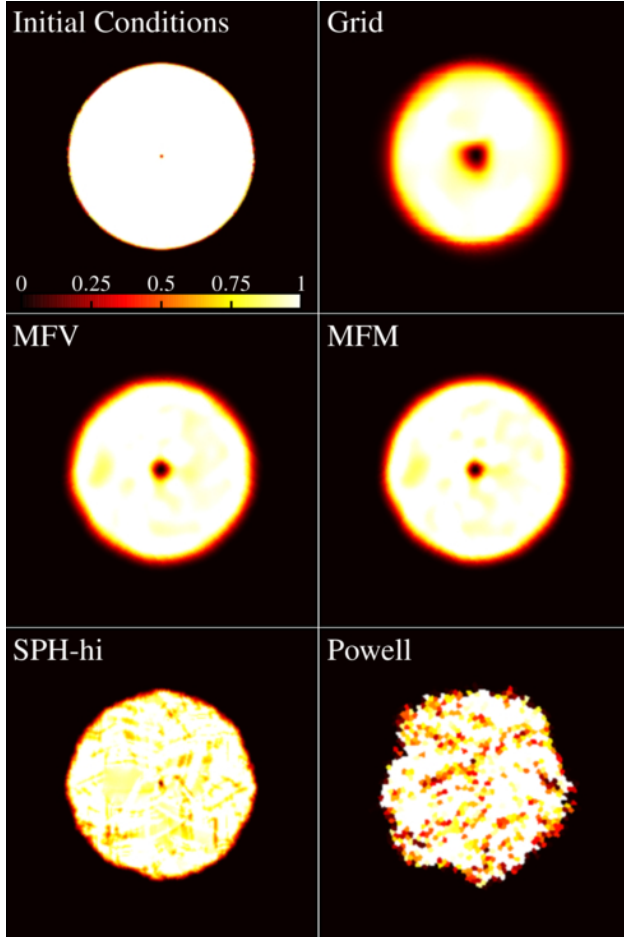


Figure 5. Field loop advection test (§ 3.4). An equilibrium, 2D field loop is advected uniformly across the domain; we plot $|\mathbf{B}|^2$ (in units of the initial loop value, as labeled) at time $t = 20$, for tests with 256^2 resolution. The initial conditions (top left) should be reproduced identically. In non-moving grid methods, even at arbitrarily high order, advection errors diffuse the loop, while numerical resistivity reduces the central field strength. In MFM/MFV/SPH, the advection errors are eliminated, and numerical resistivity at the center is reduced; however divergence-cleaning and “grid noise” from an irregular cell distribution produce some diffusion and noise (the peak value of $h|\nabla \cdot \mathbf{B}|/|\mathbf{B}|$ in any cell at any time remains $\ll 0.01$, however). The Powell-only scheme exhibits much more severe noise, because the $\nabla \cdot \mathbf{B}$ errors are transported but not damped; this leads to non-linear corruption of the solution.

than in MFM/MFV (so it behaves like the Powell case); however once enough diffusion and particle re-arrangement has occurred, the divergence-cleaning operator can work effectively, and the energy decays at approximately the same rate as our MFM/MFV calculations.

3.5 Hawley-Stone Current Sheet: Numerical Stability

This test follows Hawley & Stone (1995). In a 2D periodic domain with $-0.5 < x < 0.5$, $-0.5 < y < 0.5$, we initialize $(\rho, P, v_x, v_y, v_z, B_x, B_z) = (1, \beta/2, A \sin(2\pi y), 0, 0, 0, 0)$ and $\gamma = 5/3$, with $B_y/(4\pi)^{1/2} = 1$ for $|x| > 0.25$ and $B_y/(4\pi)^{1/2} = -1$ otherwise. This is not a good test of algorithm accuracy, since the non-linear solution depends sensitively on the numerical dissipation in different methods. However, it is a powerful test of code robustness. Qualitatively, the solution should exhibit rapid reconnection along the initial current sheet, which will launch nonlinear polarized Alfvén waves, that generate magnetosonic waves, while mag-

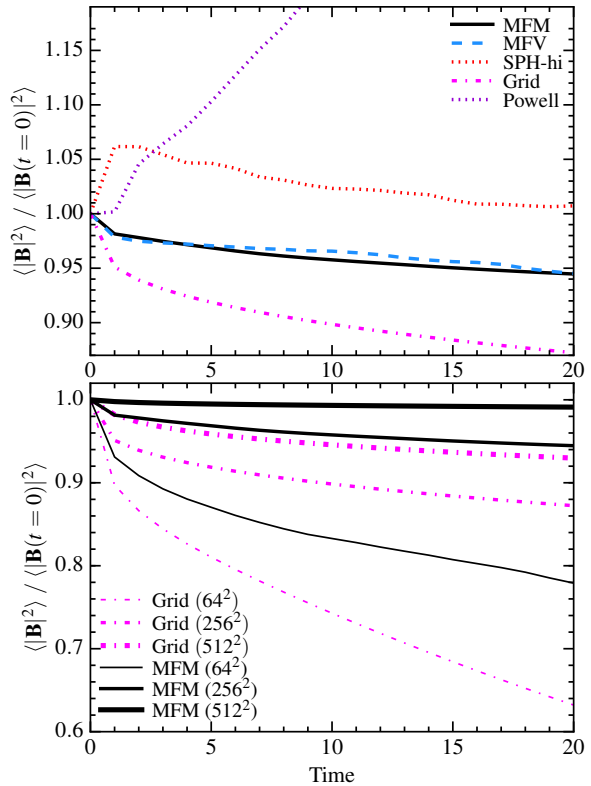


Figure 6. Quantitative decay of the box-averaged magnetic energy in the field loop test (Fig. 5), owing to numerical diffusion/resistivity. At infinite resolution, methods preserve the initial $\langle |\mathbf{B}|^2 \rangle$. Because they are Lagrangian, MFM/MFV/SPH methods show much less dissipation than high-order grid methods at the same resolution (default runs here are 256^2 , but we compare $64^2 - 512^2$ MFM/grid runs for reference). SPH shows spurious initial growth of $\langle |\mathbf{B}| \rangle$ as divergence-cleaning acts on zeroth-order kernel errors, but the subsequent decay rate is close to MFM/MFV. Otherwise on this test SPH is not as sensitive to N_{NGB} . Powell-only methods are unstable on this problem, and lead to artificial field amplification.

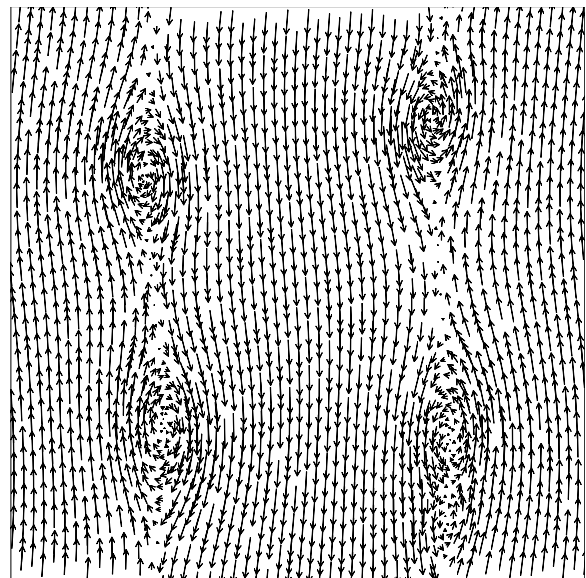


Figure 7. Hawley-Stone current sheet (§ 3.5). We plot magnetic field lines (arrows indicate local field strength and direction) at time $t = 5$ with $\beta = 0.1$, $A = 0.1$, in MFM, MFV, SPH, and grid-methods produce very similar results for these parameters. Reconnection along the current sheets leads to magnetic “islands” which grow and merge. Our new mesh-free methods are able to stably evolve the current sheet indefinitely, with $h|\nabla \cdot \mathbf{B}|/|\mathbf{B}| \ll 10^{-2}$ for all cells at all times.

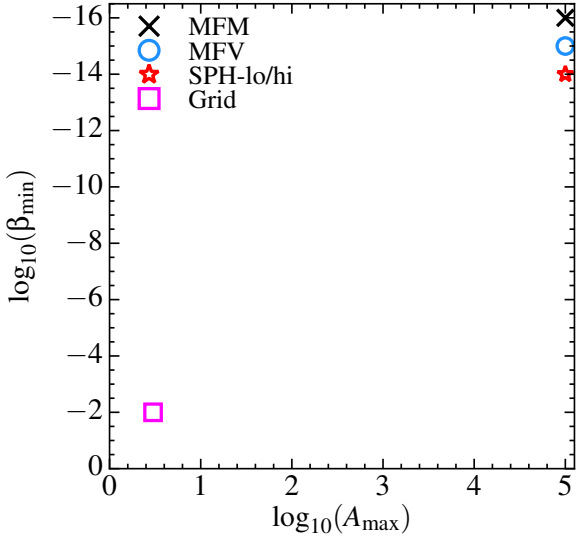


Figure 8. Stability limits of the current sheet problem in Fig. 7. Given an initial pressure $P = \beta/2$, and velocity perturbation with amplitude A , we consider the minimum β and maximum A for which the problem can be evolved stably to time $t = 10$ (further to the top-right is more-stable). In the grid-based CT method of ATHENA, the total-energy formulation of the code, coupled with high-accuracy subtraction needed for accurate CT, and advection errors when the fluid moves over the grid, mean that the method will crash (negative pressures result) for $\beta \leq 0.01$ or $A \geq 3$. Combining the dual-energy formalism from Paper I, with a Lagrangian method that moves with the fluid, and using divergence-cleaning instead of CT, we are able to stably evolve the system until β reaches machine-error levels $\sim 10^{-16}$, and arbitrarily large $A \gtrsim 10^5$ (we have not considered larger A only because the simulations become too expensive, not because they crash).

netic islands form, grow, and merge. For smaller β and larger A , it becomes more difficult for algorithms to evolve without crashing or returning unphysical solutions (e.g. negative pressures in the Riemann problem).

Fig. 7 shows the magnetic topology at time $t = 5$ in a run with $\beta = 0.1$, $A = 0.1$. For these parameters, MFM, MFV, SPH, and grid methods (here, ATHENA) all look very similar.¹⁰ The real test arises when we vary β and A ; in Fig. 8, we plot the maximum A and minimum β which we are able to use in each algorithm before the code crashes or returns an unphysical result. ATHENA crashes after some small early-time evolution for $\beta \leq 0.01$ or $A \geq 3$. The low- β problem most likely owes to the fact that the method evolves total energy: when the magnetic energy dominates, this causes serious difficulty recovering the correct internal energy (since we must subtract two large numbers), eventually producing negative temperatures. Here we use a dual-energy formalism described in Paper I, which does not conserve total energy to machine error, but can handle essentially arbitrary ratios. So for our SPH, MFM, MFV implementations, β_{\min} is limited by essentially machine error ($\beta_{\min} \sim 10^{-14} - 10^{-16}$, depending on the formulation). For A , we find similar results; the increased stability owes both to the same dual-energy formalism above, but also to the Lagrangian method, which eliminates the advection errors that, in grid-based codes, become larger with the local fluid velocity. In non-moving grid codes, eventually, at any resolution, there is some bulk velocity which will wipe out the correct physical solution completely (necessitating still-higher resolution); this is avoided in Lagrangian methods.

¹⁰ For extensive description of this test problem in ATHENA, see <http://www.astro.virginia.edu/VITA/ATHENA/cs.html>

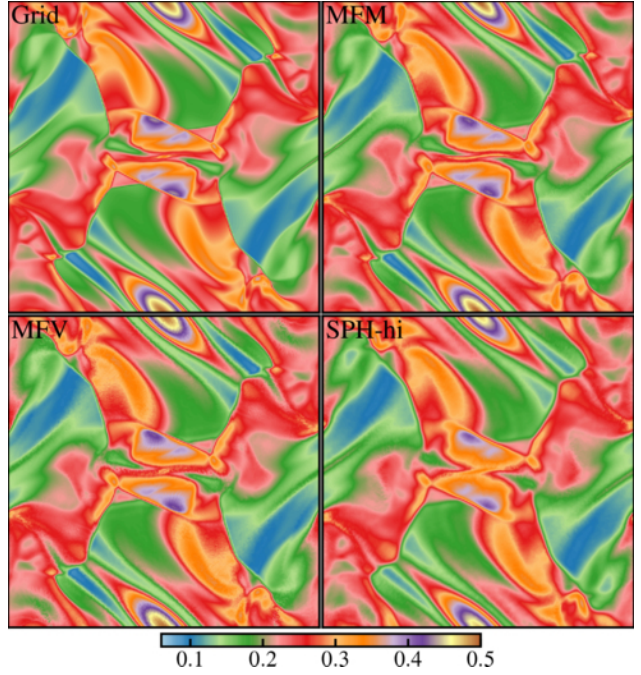


Figure 9. The Orszag-Tang vortex (§ 3.6). We show images of density ρ (in code units, as labeled) at time $t = 0.5$, in runs with 256^2 elements (particles/cells). All methods develop the major qualitative features, though there is some additional smoothing in SPH. Note that the contact discontinuities and shocks are captured sharply in MFM/MFV methods.

We explore only values of A up to $\sim 10^5$ in this test because the timestep becomes so small that it is impractical to evolve the system to late non-linear times, but we suspect the robustness of the algorithms should hold to similar machine error levels (i.e. allowing $A \sim 10^{16}$).

3.6 Orszag-Tang Vortex: Shock-Capturing & Super-Sonic MHD Turbulence

The Orszag-Tang vortex is a standard MHD test which captures a variety of MHD discontinuities, and develops super-sonic MHD turbulence, which is particularly challenging for many methods. In a periodic 2D domain of unit size, we take $\gamma = 5/3$ and set $(\rho, P, v_x, v_y, v_z, B_x, B_y, B_z) = (25/(36\pi), 5/(12\pi), -\sin(2\pi y), \sin(2\pi x), -\sin(2\pi y)/(4\pi)^{1/2}, \sin(4\pi x)/(4\pi)^{1/2}, 0)$.

Fig. 9 compares images of the resulting density field at $t = 0.5$; Fig. 10 quantitatively compares these by plotting the density and x , y components of \mathbf{B} in a slice through $y = 0.3125$ at the same time. All runs here have 256^2 resolution. In all the methods here, all of the key qualitative features are captured, including several complicated shocks, discontinuities, and sharp features. Non-moving grid, MFM, and MFV solutions are essentially indistinguishable; they have converged very well to the exact solution already, with only a slight smoothing of the sharpest features (as expected). Their “effective resolution” appears identical. However, if we boost the system by a constant velocity, at fixed resolution the stationary-grid solution degrades; for a $v_x = 10$ boost it is more comparable to a 64^2 run. Obviously the Lagrangian methods avoid this source of error. Divergence errors are well-controlled even in super-sonic shocks.

SPH does nearly as well, although the features in \mathbf{B} are more smoothed (similar to a 100^2 MFM/MFV/grid result). On this problem, there is not a dramatic difference, interestingly, between SPH with normal versus large neighbor numbers. As we saw in the shocktube tests, the divergence errors are larger by a factor of several in SPH compared to MFM/MFV.

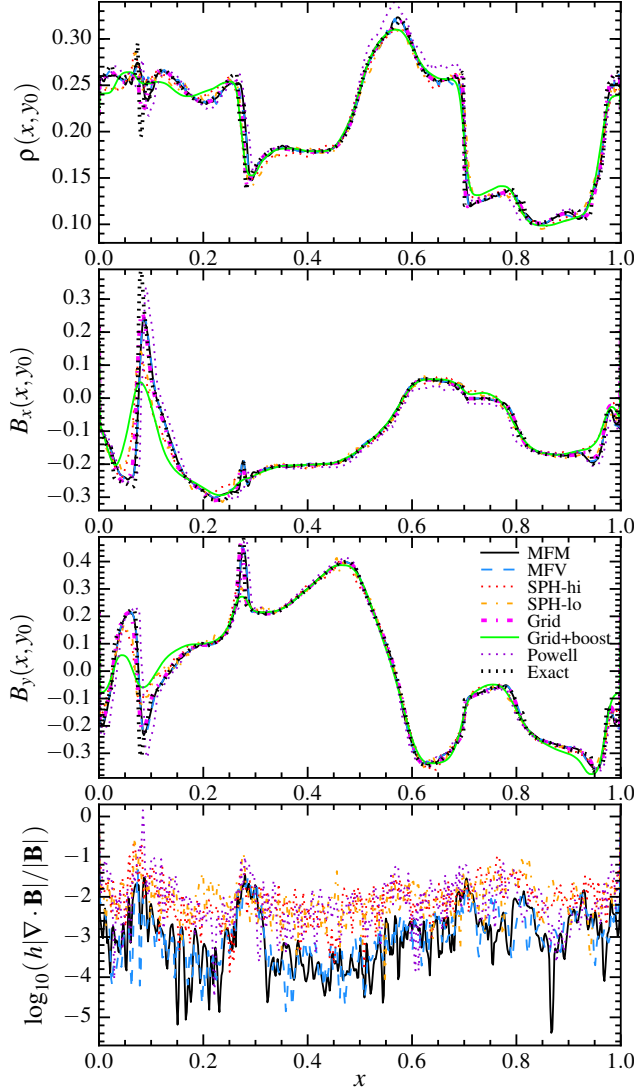


Figure 10. Comparison of the Orszag-Tang problem from Fig. 9. We plot density ρ , magnetic field components B_x , B_y , and $\nabla \cdot \mathbf{B}$, in horizontal slices at $y_0 = 0.3125$. With 256^2 cells, MFM, MFV, and grid methods have converged well to the exact solution (except for some small smoothing of the sharpest features). Here, the “exact” line is a 2048^2 ATHENA PPM CT result; at resolution $> 512^2$, MFM/MFV/unboosted-ATHENA results are indistinguishable. SPH performs well but shows further smoothing which converges more slowly. We also consider a grid simulation where the fluid is given an additional boost (a uniform $v_x = 10$); the Lagrangian (MFM/MFV/SPH) methods are invariant to these boosts. But in grid codes the boost produces a smoothing of the \mathbf{B} features at $x \sim 0 - 0.2$; these require grid resolution $> 1024^2$ to converge away. Using only Powell divergence subtraction leads to a systematic error in ρ which is small, but does not converge away.

If we use a Powell-only cleaning scheme, the results are not too badly corrupted by $\nabla \cdot \mathbf{B}$ errors; however we do see some systematic offsets, particularly in ρ around $x \sim 0.6$, and the position of the \mathbf{B} jumps around $x \approx 0.1$, that do not appear to converge away.

Fig. 11 demonstrates the convergence in our MFM method (MFV results are nearly identical here). As we increase the resolution, we clearly see good convergence towards the exact solution in *all* features here. Quantitatively, the convergence in the L_1 and L_2 norms of the plotted quantities is first-order, as expected due to the presence of shocks (the same is true in ATHENA). Compare this to older SPH MHD implementations, which only saw convergence in

some features, while others converged slowly or not at all (a well-known issue in SPH; Stasyszyn et al. 2013).

We have also considered the pure driven-turbulent box problems from Paper I (rms Mach numbers ~ 0.3 and ~ 8), as well as the ABC dynamo (Arnold et al. 1981) with small initial seed fields; we confirm that the turbulent power spectra and growth rate of magnetic energy in the box agree well between MFM, MFV, and grid methods. This echoes our conclusions for the pure hydrodynamic case in Paper I. With Powell-only cleaning, however, the growth rate of the magnetic energy in the highly super-sonic case is artificially high (growing faster than the flow-crossing time, indicating a clear numerical artifact). In SPH, the results depend on neighbor number, in a manner that we demonstrate in detail for the MRI test problem below.

3.7 The Magnetic Rotor: Torsional MHD Waves

Next we consider the MHD rotor, a standard problem from Bal-Sara & Spicer (1999) used to test strong torsional Alfvén waves. A 2D domain of unit size and $\gamma = 7/5$, is initialized with uniform $P = 1$, $\mathbf{B} = (5/\sqrt{4\pi}, 0, 0)$. Inside a circle of size $R_0 = 0.1$, $\rho = 10$ and $\mathbf{v} = (-2y/R_0, 2x/R_0, 0)$; this is surrounded by a ring-shaped transition region from $R_0 < R < R_1 = 0.115$ with $\rho = 1 + 9f(R)$, $\mathbf{v} = (-2yf(R)/R, 2xf(R)/R, 0)$ with $f(R) = (R_1 - R)/(R_1 - R_0)$. At $R > R_1$, $\rho = 1$ and $\mathbf{v} = (0, 0, 0)$.

As with the Orszag-Tang vortex, Figs. 12-13 plot images of the magnetic energy density and field values in horizontal slices, at time $t = 0.15$. Again, all methods capture the key qualitative features. MFM/MFV and grid methods are very similar. Grid methods converge slightly more rapidly on the sharp \mathbf{B} field “spikes” at $x = 0.3, 0.7$ if the bulk velocity is nil, but if the fluid is boosted appreciably, the density spikes are noticeably more smoothed. In either case, MFM, MFV, and grid methods exhibit convergence at the same order. Divergence errors are again well-controlled, even around large discontinuities in \mathbf{B} .

Here, for SPH, using the same neighbor number as MFM/MFV (3D-equivalent 32 neighbors) leads to significant noise, and some systematic errors in \mathbf{B} around $x \sim 0.15 - 0.3, 0.7 - 0.85$. These are resolved if a large neighbor number is used. However in both cases significant smoothing of the local extremum in the magnetic pressure (the brown patches at $y \approx 0.5 \pm 0.15$ in Fig. 12) is evident, and $\nabla \cdot \mathbf{B}$ is less accurately suppressed.

With only Powell-cleaning, significantly more noise is evident in the image; moreover, the systematic offset of the discontinuity positions in B_x is clear, and this does not converge away.

3.8 Magnetized Blastwave: Strong Shocks & Grid-Alignment Effects

Next we consider a strong blastwave in a magnetic field; this is another standard problem, which tests the ability of the code to handle strong shocks and preserve symmetry. In the hydrodynamic version of this test, it is also very challenging for grid-based codes to avoid strong grid-alignment and preferential propagation of shocks along the grid (see Paper I); however these effects are reduced by the asymmetric forces in the MHD problem.

We initialize a 2D periodic domain of unit size with $\gamma = 5/3$, zero velocity, $\rho = 1$, $\mathbf{B} = (1/\sqrt{2}, 1/\sqrt{2}, 0)$, and pressure $P = 10$ within a circle at the center of initial size $R < R_0 = 0.1$ and $P = 0.1$ outside. Figs. 14-15 show images and slices through the solution at time $t = 0.2$, for 256^2 runs. Visually, the MFM/MFV, SPH (with high neighbor number), and grid (with zero boost to the fluid) solutions look similar. The blast expands correctly, with the cavity growing more rapidly in the direction along the field lines. There

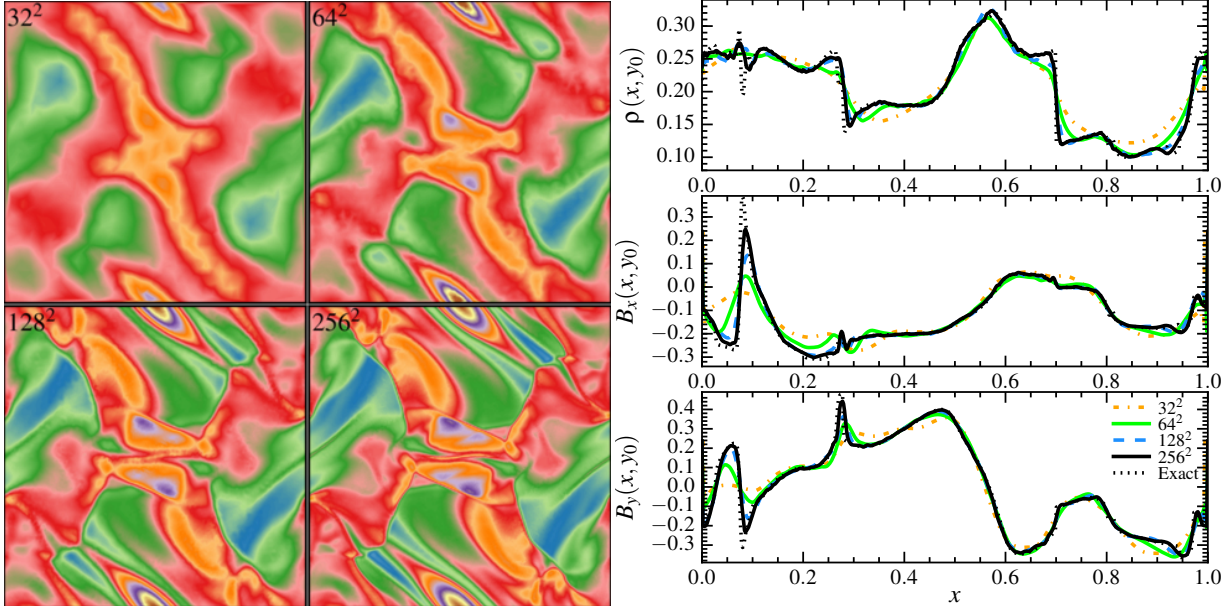


Figure 11. Resolution study of the Orszag-Tang vortex in our MFM method (MFV is essentially identical). We show both images as Fig. 9 and slices as Fig. 10, for several resolutions. Most major features are present even at low resolution; convergence with higher resolution is clear for all features. The formal L_1 and L_2 convergence accuracy is close to ideal scaling $\propto N^{-1}$ for this problem (given that it includes shocks and discontinuities).

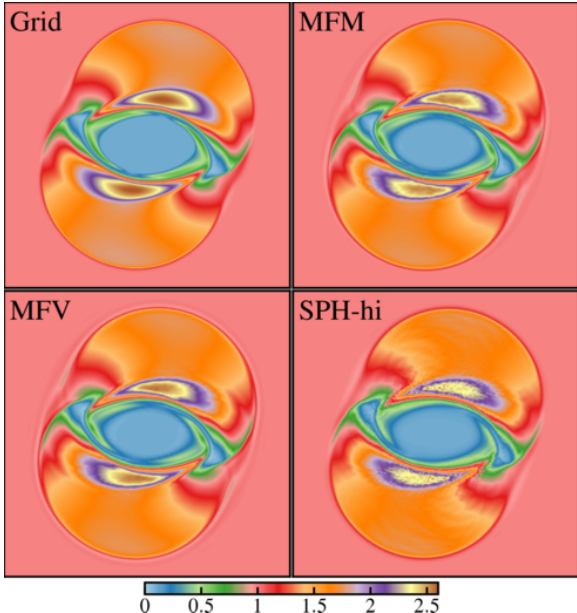


Figure 12. Magnetic rotor (§ 3.7). We show images as Fig. 9 of the magnetic pressure $|\mathbf{B}|^2/2$ (in code units, as labeled), for runs with 256^2 resolution. Most features appear identical; however note some difficulty in SPH capturing the pressure extrema at $y \approx 0.5 \pm 0.15$, and additional noise in SPH (especially with low neighbor number). With Powell-only cleaning, similar errors and noise appear.

is some additional detail visible in the high-density regions in the Lagrangian solutions (the “dimpling” in the upper-right and lower-left); this is real and appears at slightly higher resolution in the grid calculation as well. The SPH solution is slightly more smoothed along the shock fronts. Here we also show the Powell-only and boosted-grid results; unlike the Orszag-Tang and rotor problems, here the differences are plainly visible by-eye. The Powell case develops incorrect features; the boosted-grid case loses symmetry.

Quantitatively, we see these effects in Fig. 15. Note that MFM/MFV methods exhibit very small $\nabla \cdot \mathbf{B}$ values; SPH exhibits

larger $\nabla \cdot \mathbf{B}$, but still quite small. In general, different methods agree fairly well quantitatively. However, for the Powell-only case, the value of B_x , in particular, is seriously wrong in the upper-right portion of the solution. We emphasize that the error is *worse* if we re-simulate this with Powell-only cleaning but a resolution of 1024^2 . The failure of this method to guarantee the correct shock jumps corrupts the entire late-time solution. Note that, in SPH (using the full Dedner et al. (2002) cleaning), the magnitude of the $\nabla \cdot \mathbf{B}$ errors is not much smaller than our Powell-only run, but this incorrect behavior does not appear. This emphasizes that the *magnitude* of $h|\nabla \cdot \mathbf{B}|/|\mathbf{B}|$ is not, by itself, the whole story; non-linear errors are damped by the Dedner et al. (2002) approach (at the cost of some additional local diffusion) which would otherwise build up coherently at later times. Even quite large values of $\nabla \cdot \mathbf{B} \sim 0.1 - 1$ can be tolerated, if the algorithm includes a proper damping formulation (as our MFM/MFV/SPH implementations do).

3.9 MHD Rayleigh-Taylor & Kelvin-Helmholtz Instabilities: Fluid Mixing in MHD

Fluid mixing instabilities are astrophysically important and historically challenging for SPH methods; the hydrodynamic forms of these are discussed at length in Paper I. In MHD, non-zero $|\mathbf{B}|$ suppresses the growth of small-scale modes. If magnetic fields are too strong, no interesting modes grow. If fields are too weak, the case is essentially hydrodynamic. But there is an interesting, MHD-specific regime when the fields strengths are near-marginal; we consider this in a Rayleigh-Taylor (RT) problem.

We take initial conditions from Paper I and Abel (2011): in a 2D domain with $0 < x < 1/2$ (periodic boundaries) and $0 < y < 1$ (reflecting boundaries), we take $\gamma = 1.4$, $\mathbf{B}/\sqrt{4\pi} = (0.07, 0, 0)$, and $\rho(y) = \rho_1 + (\rho_2 - \rho_1)/(1 + \exp[-(y - 0.5)/\Delta])$ with $\rho_1 = 1$, $\rho_2 = 2$, $\Delta = 0.025$. Initial pressures are assigned to produce a gradient in hydrostatic equilibrium with a uniform gravitational acceleration $g = -1/2$ in the y direction (at the interface, $P = \rho_2/\gamma = 10/7$ so $c_s = 1$). An initial y -velocity perturbation $v_y = \delta v_y (1 + \cos(8\pi(x + 1/4))) (1 + \cos(5\pi(y - 1/2)))$ with

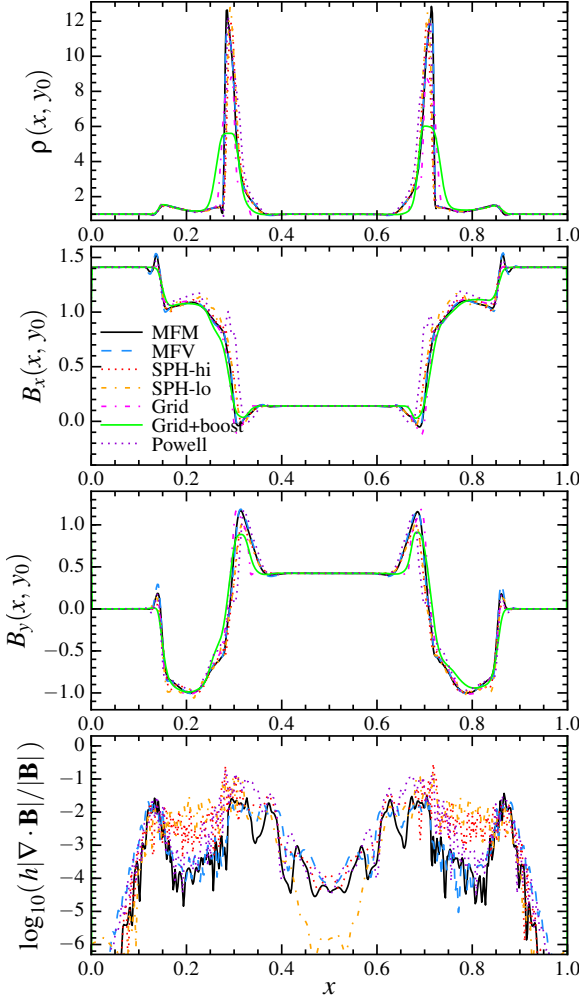


Figure 13. Density and magnetic fields in a slice through $y_0 = 1/2$ in the MHD rotor problem in Fig. 12. The qualitative differences between methods are the same as in Fig. 10 (the ‘‘grid+boost’’ run uses the same bulk $v_x = 10$). MFM/MFV/grid methods agree well. Note that boosted grid methods smooth the pressure spikes significantly, and Powell-only cleaning leads to systematically incorrect shock positions.

$\delta v_y = 0.025$ is applied in the range $0.3 < y < 0.7$ (otherwise the velocities are zero).¹¹

Fig. 16 shows the resulting density field at intermediate and late times, in a 128×256 simulation. In MFM, MFV, grid/AMR with non-moving fluid, and SPH (with sufficiently large neighbor number), the linear growth of the field is essentially identical; this is consistent with our pure-hydro results in Paper I. Even the non-linear, late-time results agree reasonably well (although there is some symmetry-breaking in SPH which owes to less-accurate $\nabla \cdot \mathbf{B}$ -cleaning, even at large neighbor number). There is slightly more ‘‘grid noise’’ in MFV at this resolution (which leads to small differences in the late-time evolution). Just like in the pure hydrodynamic case, in SPH, the results are very sensitive to neighbor number: if a smaller neighbor number is used (say, the same as we use in our MFM/MFV methods), then the initial seed mode is too

¹¹ Following the method in Paper I, we use the routines generously provided by R. O’Leary to construct the mesh-free initial conditions, then re-interpolate this onto the ATHENA grid. This is critical to ensure that the same ‘‘seed’’ grid noise is present in both methods, which in turn is necessary to see similar behavior in the late-time, non-linear phase of evolution.

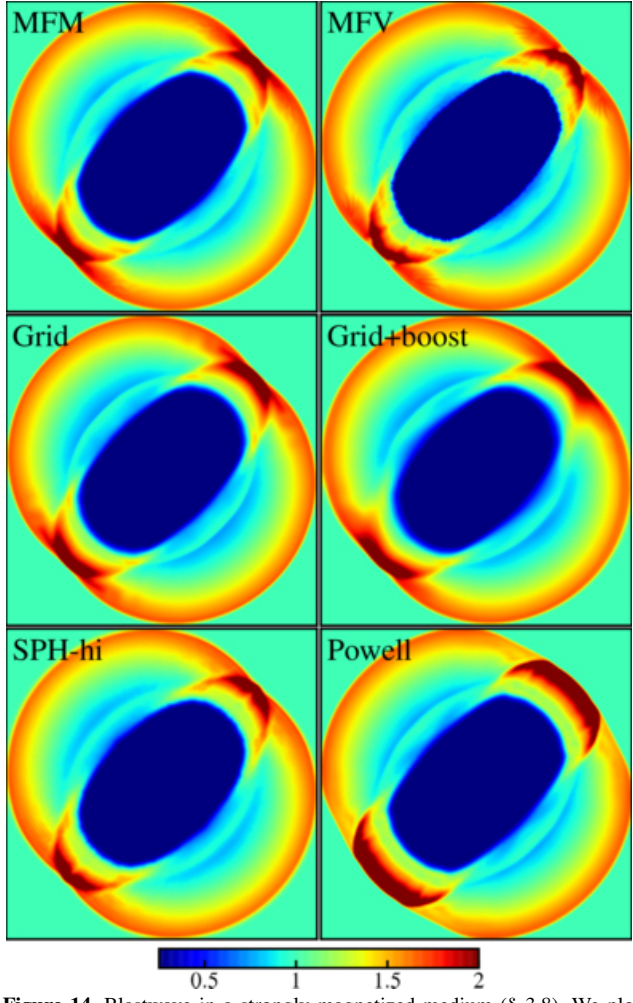


Figure 14. Blastwave in a strongly magnetized medium (§ 3.8). We plot density ρ (as labeled) in 256^2 simulations. The blastwave expands asymmetrically along field lines (initial $\mathbf{B} = (1/\sqrt{2}, 1/\sqrt{2}, 0)$), as expected. All methods capture the key behaviors; Lagrangian methods capture slightly more detail in the high-density regions, but with enhanced grid noise. Stationary-grid methods converge more slowly when the fluid is boosted (here, $v_x = 10$); the errors break the symmetry of the solution noticeably at this resolution, but they do eventually converge away. Using only Powell/8-wave methods (no $\nabla \cdot \mathbf{B}$ -damping) leads to physically incorrect shapes of the high-density features in the top-right and bottom-left corners; these *do not* converge away with resolution.

weak – it is overwhelmed by the zeroth-order errors in the method, and no modes grow. Similarly, if we boost the fluid by a constant velocity in stationary-grid methods, advection errors break symmetry and dramatically suppress the growth of the mode at this resolution (much higher resolution is required to match the accuracy of the Lagrangian methods). All of this is consistent with our results from the hydrodynamic case in Paper I.

If we consider the Powell-only case, the *linear* mode evolution appears reasonable – the growth rates are only slightly suppressed. However, in the *non-linear* phase, the solution is totally corrupted! The non-linear errors accumulate, if only Powell-type schemes are used (once again, because in this method, divergence errors are only transported, not suppressed), until they overwhelm the real solution. Clearly, tests restricted to the linear regime are not sufficient to validate divergence-cleaning schemes.

In SPH, we also find another difficulty unique to MHD. Numerical stability in SPH requires somewhat ad-hoc artificial dissipation.

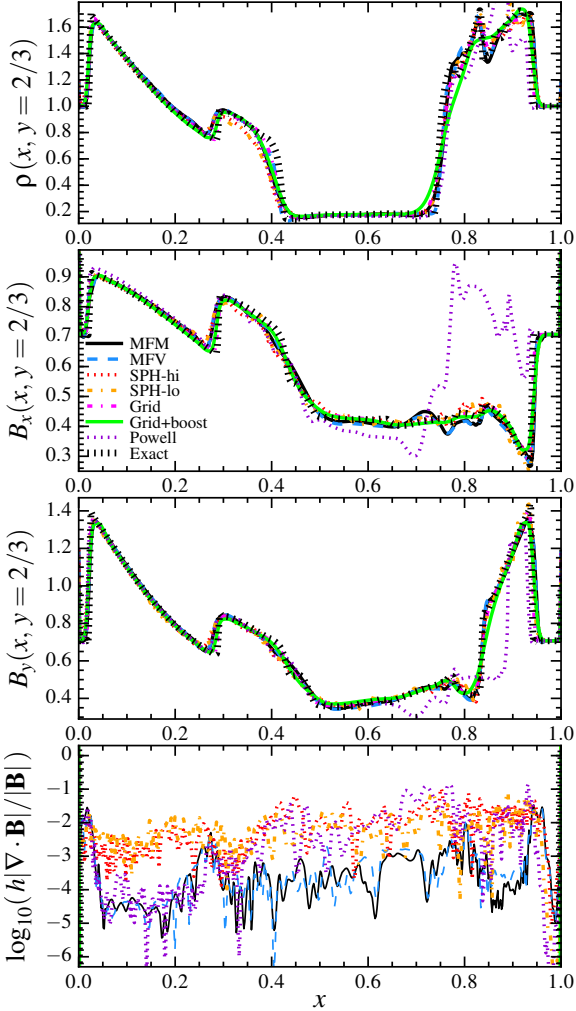


Figure 15. Slices through the MHD blastwave in Fig. 14. Most methods agree well; the convergence is good at this resolution except for SPH without a large neighbor number, or grids if the fluid is moving. The errors from the Powell-only (no-cleaning) method are dramatic: in B_x , we see factor $\sim 2-3$ systematically incorrect results.

pation terms for \mathbf{B} , the “artificial resistivity.” As discussed in Appendix A, and Rosswog & Price (2007); Tricco & Price (2013), this carries ambiguities that are not present in hydrodynamics: the appropriate “signal velocity” for the resistivity could be the sound speed, Alfvén velocity, or magnetosonic speed, and in some cases resistivity should be applied in rarefactions. The correct answer depends on the type of MHD discontinuity. In Godunov methods such as MFM/MFV/grid codes, the correct form of the dissipation is provided by the appropriate solution to the Riemann problem. But in SPH, even with the state-of-the-art “switches” used here, this is difficult to assign correctly. By default, we use the Alfvén velocity in this switch. But Tricco & Price (2013) show that this can lead to too-low a resistivity in super-sonic MHD turbulence, in turn producing shock breakup and serious noise (see their Fig. 7). They recommend increasing the dissipation by using the fast magnetosonic speed v_{fast} instead. However, if we do that for this problem, it produces excessive dissipation of the magnetic field around the contact

discontinuity.¹² This makes the problem behave (incorrectly) like the pure-hydrodynamic case.

In Fig. 17, we show full 2D maps of the divergence $h|\nabla \cdot \mathbf{B}|/|\mathbf{B}|$. In MFM/MFV, these are extremely well-controlled, with median values $< 10^{-4}$ and maxima $< 10^{-2}$. In our default SPH implementation, they are larger by a factor of a few. In the “ v_{fast} AR” SPH run, we see much larger values along the contact discontinuity. These are not, however, caused by poor $\nabla \cdot \mathbf{B}$ -control; rather, excessive dissipation of \mathbf{B} around the discontinuity leads to a local sharp depression of $|\mathbf{B}|$ (the denominator), as opposed to $|\nabla \cdot \mathbf{B}|$. In the Powell runs the divergence errors are (as expected) much larger.

We have also compared the magnetized Kelvin-Helmholtz instability, shown in Fig. 18. The initial conditions follow McNally et al. (2012) (see also Paper I), a 2D setup with 256^2 resolution elements following two streams with $P = 5/2$, $\gamma = 5/3$, and $(\rho, v_x) = (1, -0.5)$ and $(2, 0.5)$, with a 1% amplitude initial seed mode and small interface region between the streams. We add a uniform $\mathbf{B} = (0.1, 0, 0)$, about a factor ≈ 2 below the critical value which suppresses the instability, and show results at $t = 1.6$ and $t = 3.2$ (where the KH growth time is ≈ 0.7). Here, we obtain qualitatively identical conclusions to our RT test. In the linear and even non-linear stages, MFM/MFV and non-boosted grid results agree well, with more small-scale structure in the non-linear stages in the meshless methods (owing to increased grid noise). Quantitatively, the total magnetic energy in the box grows, with excellent agreement between these methods and converged solutions until $t \approx 2.5$ (well into the non-linear phase). However, the $v_x = 10$ boost completely suppresses mode growth in stationary grid methods at this resolution. In SPH, a reasonable, answer can be obtained with sufficiently high neighbor number *and* an appropriate choice for the artificial resistivity, but the instability is totally suppressed if we use typical neighbor numbers and behaves as if the field were much weaker in the “ v_{fast} AR” case. Comparing $\nabla \cdot \mathbf{B}$, we see the same behavior around the contact discontinuity as in the RT test; the relative performance of different methods is essentially identical, although in all cases the $\nabla \cdot \mathbf{B}$ errors are systematically smaller by a factor of a couple.

Finally, we have also compared an MHD version of the “blob” test from Agertz et al. (2007), with an initially azimuthal equipartition field inside a cold cloud, in pressure equilibrium with a hot wind. As expected the field strongly suppresses the non-linear RT and KH instabilities that tend to disrupt the cloud in the hydrodynamic case (for a detailed study, see Shin et al. 2008). Our qualitative conclusions (comparing different methods) are identical to the tests above.

3.10 Magneto-Rotational Instability: Can Meshless Methods Capture the MRI?

We next consider the magneto-rotational instability (MRI), one of the most important and historically challenging MHD phenomena. We consider a 2D axisymmetric shearing box defined as in Guan & Gammie (2008); this is a locally-Cartesian box where the x coordinate represents the radial direction R , and the other coordinate is the vertical direction z (azimuthal axisymmetry is assumed). Boundary conditions are periodic in z and shear-periodic in x :

¹² For the test in Fig. 16 labeled “ v_{fast} AR,” we keep everything about our SPH MHD method identical (including the “switch” and maximum viscosity $\alpha_B = 0.1$), except replace the Alfvén velocity in Eq. A9 with the fast magnetosonic speed.

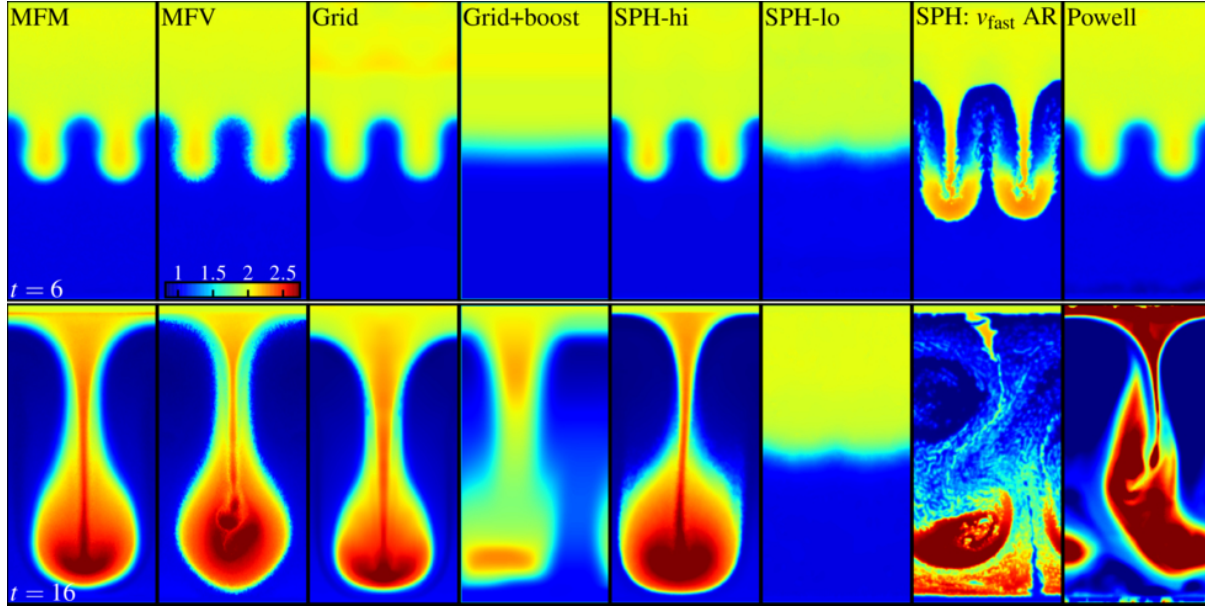


Figure 16. Magnetic Rayleigh-Taylor instability (§ 3.9). We show the density ρ (as labeled), in both early (*top*, $t = 6$) and late-time (*bottom*, $t = 16$) results at 128×256 resolution. MFM, MFV, and grid methods (with no bulk motion) all converge to the correct solution. In the early stages they are nearly identical; even in late stages there is little difference (small differences appear at late times in MFV owing to growth of the slightly-larger grid noise at early times). As in the pure-hydro case, in non-moving grid methods, “boosting” the fluid grid by a uniform velocity slows down mode growth and breaks symmetry, unless significantly higher resolution is used. In SPH, reasonable results can be obtained if large neighbor numbers are used (although some large-scale asymmetry appears in the non-linear solution because of imperfect $\nabla \cdot \mathbf{B}$ -cleaning); with smaller neighbor number (the same as used in MFM/MFV methods), low-order errors in SPH dominate and no mode grows. However, the SPH results are also very sensitive to the form of the artificial dissipation (artificial resistivity or AR) employed: we compare the results if we use the fast magnetosonic velocity v_{fast} in AR, as advocated by Trippo & Price (2013) (which reduces noise in super-sonic problems), instead of our default choice (the Alfvén velocity). For details, see Appendix A. This produces too much dissipation around the contact discontinuity, which damps the \mathbf{B} -field to sub-critical values; so the instability behaves (incorrectly) like the pure-hydro case.

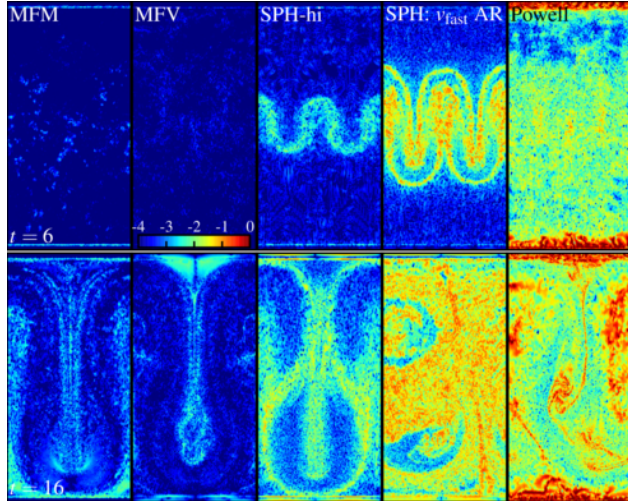


Figure 17. Divergence errors in the MHD RT instability from Fig. 16. We plot $\log_{10}(h|\nabla \cdot \mathbf{B}|/|\mathbf{B}|)$ (as labeled), for the same times as Fig. 16. The grid methods here use CT so $\nabla \cdot \mathbf{B} = 0$ to machine precision. MFM/MFV methods maintain $\log_{10}(h|\nabla \cdot \mathbf{B}|/|\mathbf{B}|) < -2$ (for every particle/cell) even into the late non-linear evolution (most of the values at > -4 are boundary effects, in fact). In SPH, the zeroth-order errors around a contact discontinuity lead to less-accurate cleaning in these regions. In the v_{fast} artificial resistivity (AR) case, $h|\nabla \cdot \mathbf{B}|/|\mathbf{B}| \sim 1$ around these discontinuities; this is not because $\nabla \cdot \mathbf{B}$ is large, but because the AR over-damps \mathbf{B} at the discontinuity. In the Powell case, order-unity errors appear at late times.

$f(x, z) = f(x + n_x L_x, z + n_z L_z)$ for all values f except the azimuthal velocity $v_\phi = v_y(x, z) = v_y(x + n_x L_x, z + n_z L_z) + n_x q \Omega L_x$, where $q = -(1/2) d \ln \Omega^2 / d \ln R = 3/2$ for a Keplerian disk, n_x and n_y are integers representing the box periodicity, and Ω is the mid-plane

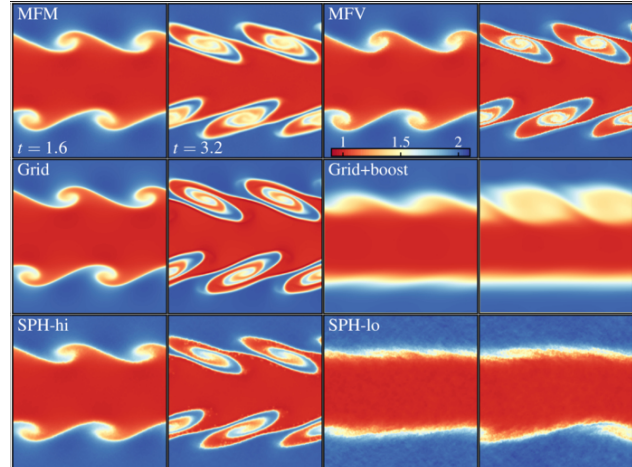


Figure 18. Magnetic Kelvin-Helmholtz (KH) instability (§ 3.9). We show density ρ (as labeled) in the non-linear phases $t = 1.6$ and $t = 3.2$ (KH growth timescale ≈ 0.7), at 256^2 resolution. Differences between methods resemble the RT test (Fig. 16). MFM, MFV, and non-boosted grid results agree well into the non-linear growth phase (where different grid noise effects lead to small departures). Boosting the fluid in the grid case or using typical neighbor numbers for SPH break symmetry and suppress the instability at this resolution. Divergence errors in each case closely resemble those in Fig. 17 around the contact discontinuities.

orbital frequency. In this approximation, the momentum equations are also modified with the source terms $D(\rho \mathbf{v})/Dt = -2(\Omega \hat{z}) \times (\rho \mathbf{v}) + 2\rho q \Omega^2 x \hat{x}$. We initialize a box of unit size ($-0.5 < x < 0.5$, $-0.5 < z < 0.5$) and $\Omega = 1$, with $(\rho, P, v_x, v_y, v_z, B_x, B_y, B_z) = (1, 1, 0, \delta v, -qx, 0, 0, B_0 \sin(2\pi x))$, where $B_0 = \sqrt{15}/(8\pi m)$ is set so that the most unstable wavelength $\lambda_{\text{MRI}} = 1/m$ corresponds

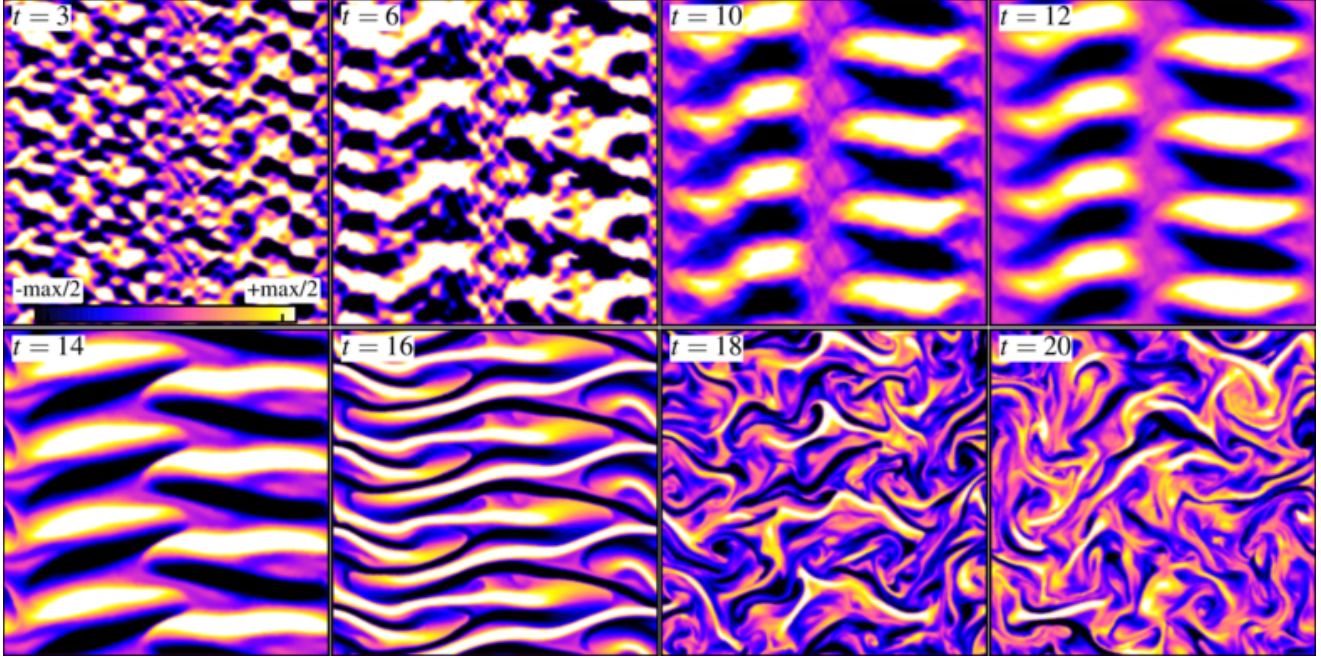


Figure 19. Magneto-rotational instability (MRI; § 3.10) test problem. We show the results from a 2D axisymmetric shearing box (horizontal/vertical axes correspond to radial/vertical coordinates), with vertical B_z set so the fastest-growing modenumber is $m = 4$. We plot the azimuthal/toroidal component B_y of the magnetic field (the behavior of the radial component is similar, but with reversed sign), in an MFM calculation at 256^2 resolution (units are scaled to the maximum/minimum values in each frame as labeled, since the absolute value of B_y grows exponentially). The initial seed noise is amplified on the correct timescale, and from times $t \sim 5 - 16$, the dominant $m = 4$ mode pattern is clearly visible. At late times, the non-linear modes break up into turbulence, as expected. MFM, MFV and high-order CT-based grid methods (see Guan & Gammie 2008) produce similar results.

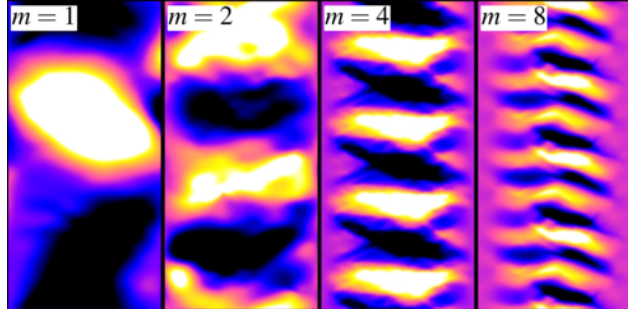


Figure 20. MRI, as Fig. 19 (same colorscale; just showing the $0 < x < 0.5$ half of the box), at times when the linear mode dominates, for runs with initial B_z set so that the fastest-growing mode corresponds to $m = 1, 2, 4, 8$, as labeled (MFM shown, MFV is nearly identical). In each case, the correct mode is clearly visible. We find approximately 4 cells/particles are required across each “node” in the linear direction to resolve the correct mode growth, the same as the number of cells in PPM grid methods.

to a mode number m . Here δv is set to a uniform random number in the range ± 0.005 for each cell, to seed the instability.

Fig. 19 shows the results at various times from a 256^2 MFM calculation with $m = 4$. We see the expected behavior; the random B -field fluctuations seeded by the velocity perturbation grow, and quickly are dominated by the fastest-growing ($m = 4$) mode, until at late times the non-linear modes break up into MRI turbulence. The same behavior appears in MFV, grid, and even SPH methods. In Fig. 20, we compare results when the linear mode dominates, for runs with initial B_z set such that $m = 1, 2, 4, 8$, with MFM at the same resolution. In each case, we see the correct mode grows. Fig. 21 compares different methods and resolutions (for $m = 4$). We see that MFM and MFV produce nearly identical results. Even at 32^2 resolution, a reasonable mode structure emerges. In general, with MFM/MFV methods, we find about ~ 4 resolution elements

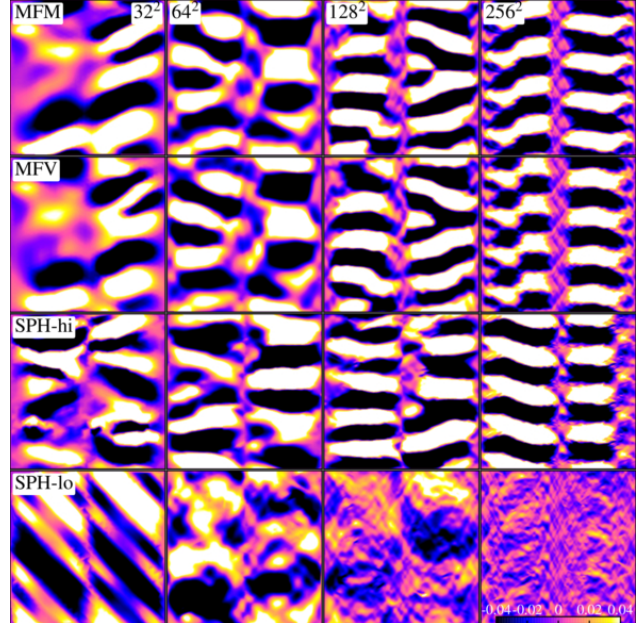


Figure 21. MRI (with mode number $m = 4$), as Fig. 19, as a function of resolution and numerical method. MFM/MFV methods are very similar, and resolve the MRI with $m = 4$ with as few as 32^2 elements. Modern SPH MHD is, in fact, also able to capture the MRI modes, if a larger neighbor number is used. If we use a smaller neighbor number in SPH, the low-order errors completely swamp the correct solution.

(particles/cells) in linear dimension across each “node” are needed to see reasonable modes (for $m = 2$, we see growth for 16^2 resolution); this is the same as in higher-order (PPM) grid-based codes using CT (see Guan & Gammie 2008).

For SPH, we see – perhaps surprisingly – reasonable behavior,

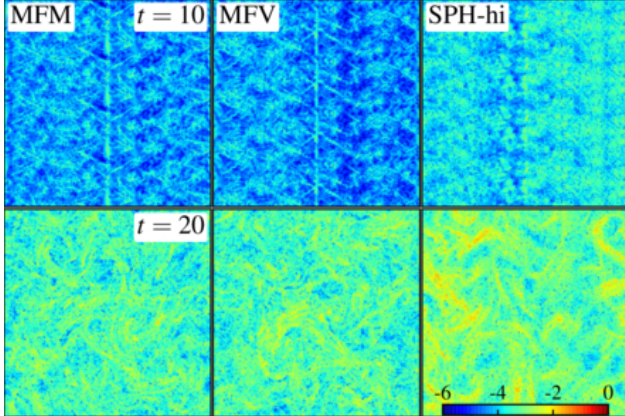


Figure 22. Divergence errors in the MRI test in Fig. 21 at 256^2 resolution. We plot $\log_{10}(h|\nabla \cdot \mathbf{B}|/|\mathbf{B}|)$ (as labeled), for two times, $t = 10$ when the fastest-growing mode dominates, and $t = 20$ when the system has broken up into turbulence (Fig. 19). In both cases, the errors are well-controlled in MFM/MFV; in SPH some regions reach larger $h|\nabla \cdot \mathbf{B}|/|\mathbf{B}| > 0.01$ in the turbulent phase; however these almost entirely correspond to regions of nearly-vanishing $|\mathbf{B}|$ (i.e. $\langle h|\nabla \cdot \mathbf{B}| \rangle / \langle |\mathbf{B}| \rangle \ll 0.01$), so the errors are not dynamically significant.

if we use large enough neighbor numbers. Compared to previous SPH MHD implementations, the fact that the new methods combine many basic hydrodynamic improvements (larger kernels to reduce noise, evolution of conserved variables, Lagrangian-derived magnetic forces, and properly-derived divergence-cleaning) leads to the ability to follow the MRI. However the noise level in SPH is higher, even with this larger neighbor number, at lower resolutions. And if we use a smaller neighbor number in SPH, comparable to what is used in our MFM/MFV methods, we see the SPH E0 errors totally dominate the solution, and prevent any mode growth.

Fig. 22 compares $h|\nabla \cdot \mathbf{B}|/|\mathbf{B}|$. Even in the late non-linear turbulence stage, these are maintained at $< 10^{-2}$ (median $\sim 10^{-4}$) in MFM/MFV, and < 0.1 (median $\sim 10^{-3}$) in SPH.

Figs. 23-24 compare the growth of the MRI modes quantitatively. We measure the amplitude of the $m = 4$ Fourier mode in radial (B_x) or azimuthal (B_y) field components (the maximum of the vertical $m = 4$ mode amplitude in the 2D Fourier transform), at each time, for the simulations above. We also compare the volume-averaged magnetic energy $\langle E_B \rangle = \langle |\mathbf{B}|^2/2 \rangle$ in the box. The linear-theory prediction is that the fastest-growing B_x and B_y modes should grow $\propto \exp(0.75t)$, so the magnetic energy should scale $\langle E_B \rangle = E_0 + \delta E \exp(1.5t)$, where E_0 is the initial energy and δE is a seed perturbation amplitude. For B_x , B_y , and E_B , we see good convergence with MFM/MFV to the correct linear growth rate at resolutions above $\sim 64^2$ for $m = 4$; this agrees well with state-of-the-art CT grid methods. At late times, the mode saturates and then the energy must decay according to the anti-dynamo theorem; this is expected. In SPH, we see no MRI growth unless we go to large neighbor numbers; we then do obtain growth, but the convergence in growth rates is slower.

In Fig. 24, we compare the late-time evolution of the magnetic energy to grid methods. The linear growth rate and peak $|\mathbf{B}|$ amplitude agree well with high-order grid-CT calculations. The late time decay rate of the magnetic energy is known to be sensitive to the numerical diffusivity of the method (see Guan & Gammie 2008, and references therein): we therefore compare three different grid codes at the same resolution (and one much higher): HAM (most diffusive), ZEUS, and ATHENA (in PPM, CT, CTU mode; least dif-

fusive). The late-time behavior in our meshless methods agrees remarkably well with ATHENA.

3.11 Collapse of a Magnetized Core: Preserving Symmetry & Launching MHD Jets

Next, we consider collapse of a magnetized proto-stellar core and launching of a proto-stellar jet. This is a less quantitative problem; however, there are several key qualitative phenomena. A rotating, weakly-magnetized, self-gravitating gas sphere is initialized. This collapses under self-gravity quasi-spherically to much higher densities, testing the ability to follow the fluid in compressions and collapse over many orders of magnitude, and whether the gravity-hydro coupling is conservative. The collapse is arrested by the formation of a disk (requiring good angular momentum conservation in the code), which slowly contracts via magnetic braking. The braking and field amplification in collapse and the subsequent disk-driven dynamo test the ability of the code to follow initially weak fields and MHD instabilities. Finally, a jet is launched: following this requires the code have good symmetry preservation, and most critically maintain low values of $\nabla \cdot \mathbf{B}$, or else the protostar will be ejected from the disk by accumulated errors (see Price et al. 2012).

Following Hennebelle & Fromang (2008), we initialize a 3D box of size-length 0.15 pc, in which the hydrodynamic forces are periodic but gravity is not. We initialize a constant-density sphere of radius $R_0 = 0.015$ pc and mass $1M_\odot$, in a uniform, non-moving background (filling the box) with factor ≈ 360 lower density. The sphere is set in rigid-body rotation such that the orbital time is 4.7×10^5 yr; this corresponds to a ratio of kinetic-to-potential energy $\text{KE}/|\text{PE}| \approx 0.045 \ll 1$. The magnetic field is initialized to a constant value B_0 , aligned with the angular momentum vector of the sphere. At all times, the system is forced to obey the baryotropic equation of state $P = (0.2 \text{ km s}^{-1})^2 \rho \sqrt{1 + (\rho/\rho_0)^{4/3}}$, with $\rho_0 = 10^{-14} \text{ g cm}^{-3}$. The value of the field B_0 is chosen to correspond to different mass-to-magnetic flux ratios, defined in the traditional fashion relative to the “critical” value quasi-stability of a spherical cloud, $\mu = (M/\Phi)/(M/\Phi)_{\text{crit}}$ where $(M/\Phi) \equiv M/(\pi R_0^2 B_0)$ and (in our units) $(M/\Phi)_{\text{crit}} \equiv 0.126 G^{-1/2}$. With M fixed, $\mu \propto B_0^{-1}$, and for our choices $\mu = 10$ corresponds to $B_0 = 61 \mu G$.

Fig. 25 shows the results from our MFM method, for various values of μ (B_0), using 60^3 total cells/particles in the box, or $\approx 50^3$ cells in the collapsing sphere (we use equal-mass particles, so the initial packing is denser in the sphere). The times are chosen to be some (short) time after a jet forms, in each case close to $t \sim 4 \times 10^4$ yr $\sim t_{\text{ff}}$, where $t_{\text{ff}} \equiv \sqrt{3}/(2\pi G\rho)$ is the gravitational free-fall time. Fig. 27 shows the same for MFV.

Even at this (modest) resolution, we are able to see all of the key behaviors above over a wide range of μ . As expected, for $\mu \lesssim 1$, a stable, thick disk forms, which does not spin up the field sufficiently to launch a jet. But for larger $\mu > 1$ (where the disk collapses rapidly), a jet is launched and propagates well into the diffuse medium as accretion onto the protostar continues. The collimation and strength of the jets vary with μ as expected, and are consistent with AMR simulations using CT and run with much higher resolution (see Hennebelle & Fromang 2008). A more quantitative exploration of this is an interesting scientific question, but outside the scope of our study here. We stress that as the fields become weaker, this problem becomes more challenging, since any excess numerical dissipation will tend to suppress field amplification and jet-launching. This is well-known from grid-based studies using Riemann solvers with different diffusivity. What is remarkable is that we are able to see jets even at $\mu \gtrsim 10$ at this resolution. For weaker fields than about $\mu \sim 20$, various authors have noted

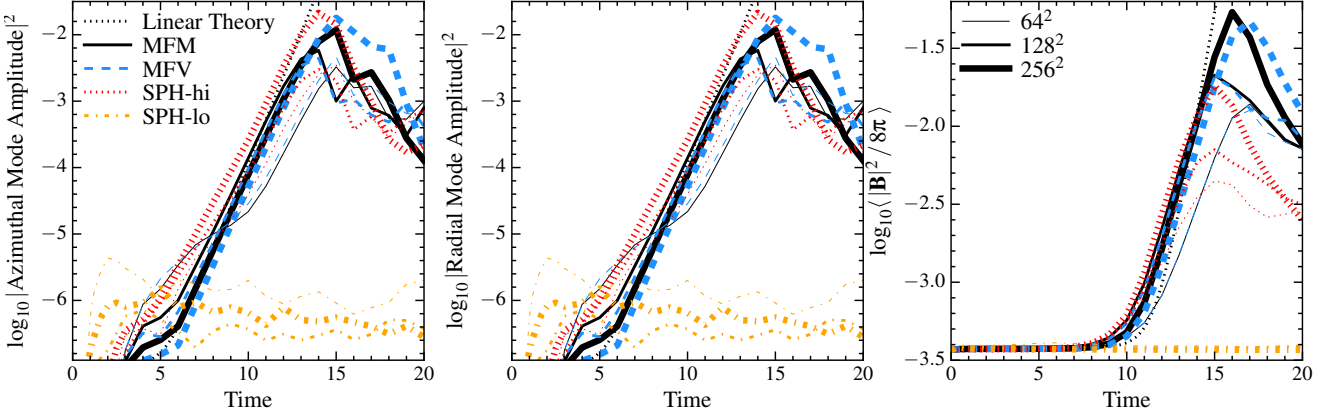


Figure 23. Growth of the $m = 4$ MRI modes in Figs. 19–21. We measure the $m = 4$ Fourier amplitude in the azimuthal (B_y ; left) and radial (B_x ; center) magnetic fields, as well as the average magnetic energy ($\langle |B|^2/8\pi \rangle$ in the box (right)). We compare each to the expectations of linear theory (dotted black line). We compare three different resolutions (64^2 , 128^2 , 256^2 , in progressively thicker lines). MFM/MFV methods give similar results; in both cases the simulations converge to the correct linear growth rate quickly at resolutions above $\sim 64^2$. This agrees well with state-of-the-art grid CT codes. The peak mode amplitude also increases with resolution; once the MRI breaks into turbulence, the field amplitude declines, as it should. For SPH, we see no MRI at *any* resolution unless we use a large neighbor number. With sufficiently large neighbor number, we obtain growth, but convergence to the correct growth rate is slower (even at 256^2 , the growth rate is suppressed by $\sim 30\%$).

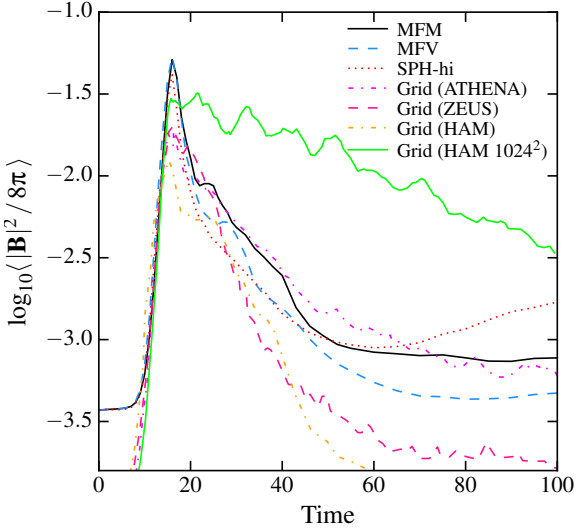


Figure 24. Late-time evolution of the magnetic energy, for the $m = 4$ case, at 256^2 resolution. We compare results from three different unsplit, CT-based grid codes in Guan & Gammie (2008). The 2nd-order HAM code is most diffusive, while the 3rd-order PPM ATHENA is least-diffusive (ZEUS is intermediate). In all cases, the linear growth rates and peak amplitudes are similar and agree well with our meshless methods; however the decay rate is sensitive to the details of numerical dissipation. Our meshless results at fixed resolution are most similar to ATHENA, the least-diffusive of the grid-based codes considered.

that the magnetic field becomes insufficient to stabilize the disk, which then fragments; we see this in our weak-field case. However, even here, we see that each fragment/protostar is launching its own “mini-jet,” which then precesses owing to the orbital motion of the fragments!

To see these behaviors, particularly in the weak-field case, usually requires quite high resolution ($> 128^3$) in grid-based codes (Hennebelle & Fromang 2008; Pakmor et al. 2011). In Fig. 26, we show a resolution study at fixed time in our fiducial MFM, $\mu = 10$ case. While the disk continues to show more fine structure, and the jets are launched slightly earlier (so have propagated further) at higher resolution, the presence of a jet is clearly resolved, and

the jet outflow rate and momentum are converged to within tens of percent, at 25^3 resolution; some jet is even visible at 12^3 resolution!

We can see these behaviors even at very low resolution because this test combines many advantages of our new methods. It is clearly Lagrangian, with high-dynamic range collapse; the fact that N -body codes naturally couple to our methods with fully adaptive gravitational softening providing second-order accuracy (Paper I) means that we can follow the entire collapse without any special “switches” required in our gravity solver. The smooth, continuous adaptive resolution provided by our method avoids the low-order errors which tend to artificially damp magnetic fields, inherent to AMR refinement boundaries. Once the disk forms, it is critical that the method be able to accurately conserve angular momentum and not degrade orbits; this is especially challenging in AMR codes (assuming $\sim 50 - 100^3$ cells across the central disk, even high-order AMR methods will degrade the orbits within a couple of periods; see Paper I & de Val-Borro et al. 2006; Hahn et al. 2010; Duffell & MacFadyen 2012).

Fig. 28 demonstrates that, because they are Lagrangian and mesh-free, our methods here are trivially invariant to both (a) boosting the entire fluid (so the core is moving super-sonically through the box), and/or (b) rotating the core at an arbitrary angle to the coordinate axes. This is *not* true in non-moving grid methods: either of these changes in grid codes implies a very significant loss of “effective resolution” or accuracy at fixed resolution. Based on comparison experiments with RAMSES, we estimate that for the $\mu = 10$, rotated+boosted case in Fig. 28, achieving comparable accuracy in AMR to our $\sim 50^3$ (10^5 -element) MFM run requires $\sim 10^8$ cells.

SPH, however, has greater difficulty with this problem. Fig. 29 shows the same survey of μ at 50^3 resolution in SPH; in no case does a stable jet develop. For small initial fields ($\mu \gtrsim 10$), artificial resistivity too-efficiently dissipates the field, so the case resembles pure hydro (either weak or no jets appear). For large fields, the method has difficulty maintaining stability: the central disk breaks up, and the proto-star is ejected! These errors are resolution-dependent, however. At higher resolution, we do begin to recover the correct behavior in SPH; Fig. 30 shows the same at 100^3 resolution. Here the high- \mathbf{B} cases begin to resemble the MFM/MFV results. The low- \mathbf{B} cases still exhibit too much dissipation (too-weak

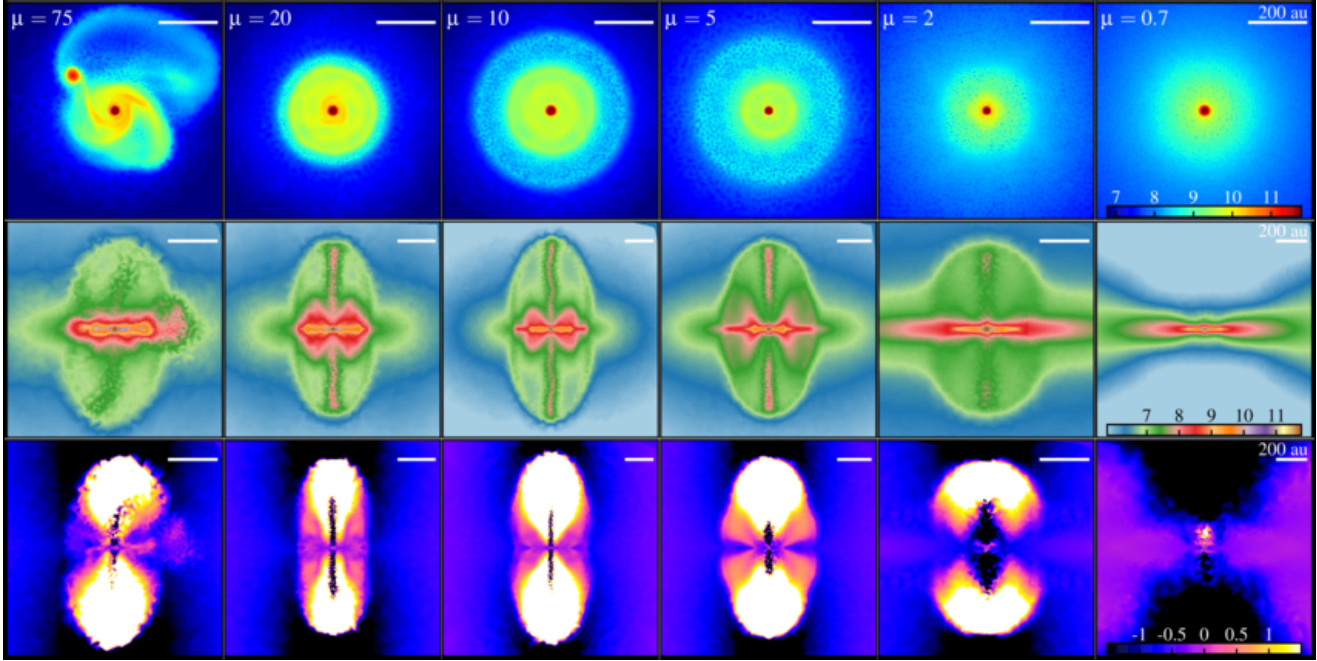


Figure 25. Proto-stellar jet test (§ 3.11). A magnetized, rotating proto-stellar core with initial mass-to-flux ratio $\mu \propto |\mathbf{B}|^{-1}$ collapses under self-gravity until it forms an accretion disk, which winds up the magnetic field and launches a jet. We show results for MFM calculations with 50^3 total particles/cells in the core, and various μ (columns labeled), just after one free-fall time of the initial core. Scale bar in each panel shows 200 au. *Top:* Density ($\log_{10}(n/\text{cm}^{-3})$), as labeled in a slice through the collapsed disk midplane (face-on). The central ‘‘protostar’’ has collapsed by a factor of $> 10^4$ in density; the disk is more extended and lower-density for stronger \mathbf{B} . For $\mu \lesssim 1$, the disk is quasi-stable, and should not form a jet. For $\mu \gtrsim 20$, the disk should fragment into multiple protostars. *Middle:* Density ($\log_{10}(n/\text{cm}^{-3})$) in a slice through the rotation axis. Here the jets are plainly visible. *Bottom:* Radial velocity ($v_r/\text{km s}^{-1}$) in a slice through the rotation axis. Even at low resolution, and very weak \mathbf{B} , our new meshless methods are able to capture jet-launching.

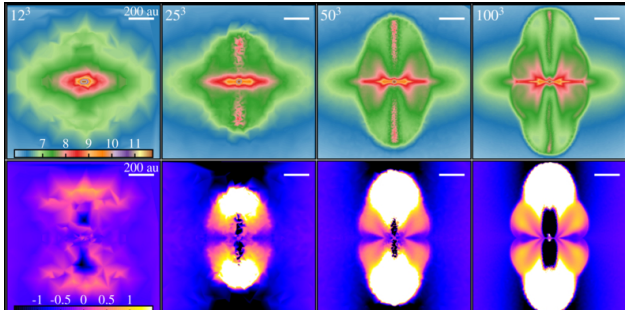


Figure 26. Resolution study of the collapsing core as in Fig. 25, using MFM (MFV is similar), with initial $\mu = 10$. We compare at fixed time ($t = 1.05 t_{\text{ff}}$). The resolution quoted is the total number of cells/particles in the collapsing spherical core. At higher resolution, additional fine-structure in the disk and outflow continue to appear; the jet also forms slightly earlier, so it has propagated further. However, there is already some (albeit weak) jet/polar outflow structure at 12^3 ; by $\sim 25^3$, the existence of a jet and much of the global structure is already resolved, and the jet momentum/mass are converged within tens of percent of the highest-resolution run. This is remarkably low resolution; usually, $> 128^3$ resolution is needed for similar convergence in grid calculations.

jets), but the field values are (very slowly) converging towards the MFM/MFV result.¹³

¹³ We have explicitly checked, for the proto-stellar jet test in SPH, whether using the Alfvén or magnetosonic velocity in the artificial resistivity (as in § 3.9) makes a large difference; it does not. Likewise the choice of ‘‘pressure’’-SPH (PSPH) versus traditional ‘‘density’’-SPH (TSPH), discussed in Paper I, is not especially significant for the core/jet problem. We have also experimented with a wide range of different artificial viscosity and conductivity parameters and find the qualitative results are similar. However, as noted in Tricco & Price (2013), it is important that the artificial

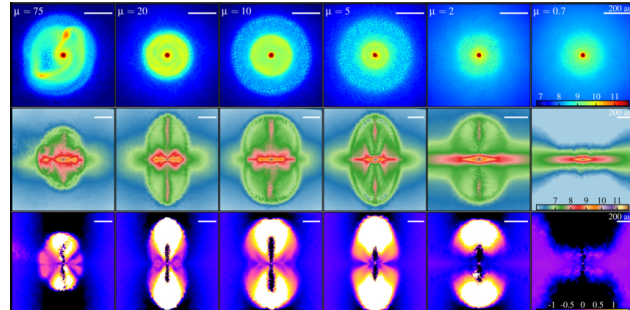


Figure 27. As Fig. 25, for MFV (shown at identical times to Fig. 25). The results are similar up to non-linear details. Note that the $\mu = 20$ case is marginally unstable to fragmentation; so small changes to the particle splitting/merging algorithm in MFV (which can seed grid noise) can lead to modest perturbations that induce earlier fragmentation (and weaker jets); the ‘‘default’’ case here allows no splitting/merging (most similar to MFM).

Fig. 31 compares the divergence errors; this illustrates the source of the instability in SPH. In MFM/MFV (essentially identical here), the errors are well-controlled at the $10^{-3} - 10^{-2}$ level (a few particles in the disk midplane reach larger values, but these are in the regime where the thin disk is completely unresolved vertically so the change in \mathbf{B} must occur across a single particle). We also clearly see that the errors decrease with resolution (the median $h|\nabla \cdot \mathbf{B}|/|\mathbf{B}|$ decreases by a factor of ~ 5 from 50^3 to 100^3 resolution). In SPH, we see much larger $\nabla \cdot \mathbf{B}$, as in many cases above – most critically, we see that where the disks have gone un-

resistivity be limited to a small maximum value; our default here is 0.1 (see Appendix A), if we raise this to 1, the \mathbf{B} fields are artificially damped away to negligible values during collapse.

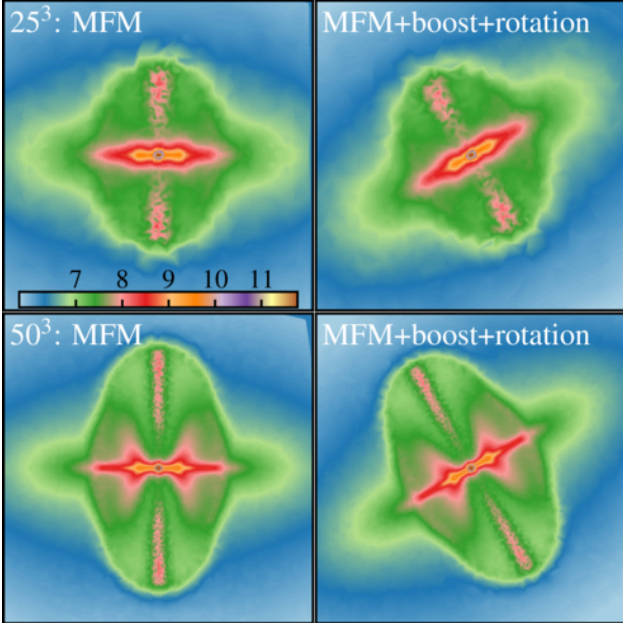


Figure 28. Effects of rotations and boosts on our meshless methods in the protostellar jet test. *Left:* Our “default” MFM run from Fig. 25 with $\mu = 10$, resolution 50^3 , zero net bulk motion and an initial angular momentum/magnetic field axis aligned with the \hat{z} direction. *Right:* Same, but with the rotation/field axis rotated 30° in the $x-z$ plane, and the entire box boosted by a uniform $\delta v_x = 10 \text{ km s}^{-1}$, $\delta v_y = \delta v_z = 2 \text{ km s}^{-1}$. Our mesh-free methods are invariant to boosts (bulk motion) of the box and rotations/grid mis-alignments at all resolutions; however these pose serious challenges for grid-based calculations.

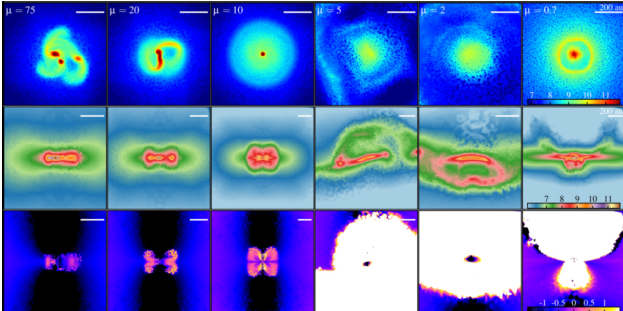


Figure 29. As Fig. 25, for SPH-hi. SPH has much greater difficulty capturing the important behaviors at low resolution. At low- $|\mathbf{B}|$, the SPH “artificial resistivity” over-damps \mathbf{B} and suppresses jets. At high- $|\mathbf{B}|$ ($\mu \ll 10$), less-accurate $\nabla \cdot \mathbf{B}$ -cleaning leads to unstable errors that disrupt the disk.

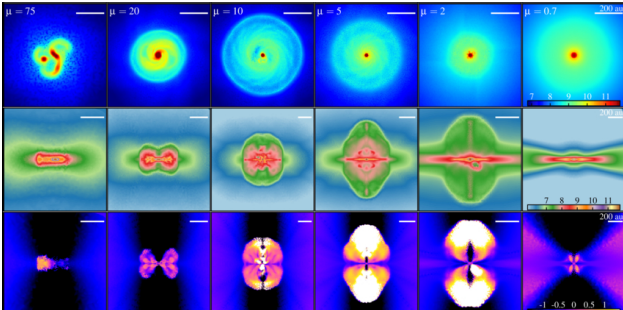


Figure 30. As Fig. 29, for SPH-hi but at higher resolution (100^3). At higher resolution, SPH is better able to control $\nabla \cdot \mathbf{B}$ errors and jets emerge at high- \mathbf{B} ($\mu < 10$); however the SPH numerical resistivity still over-damps the weak-field case.

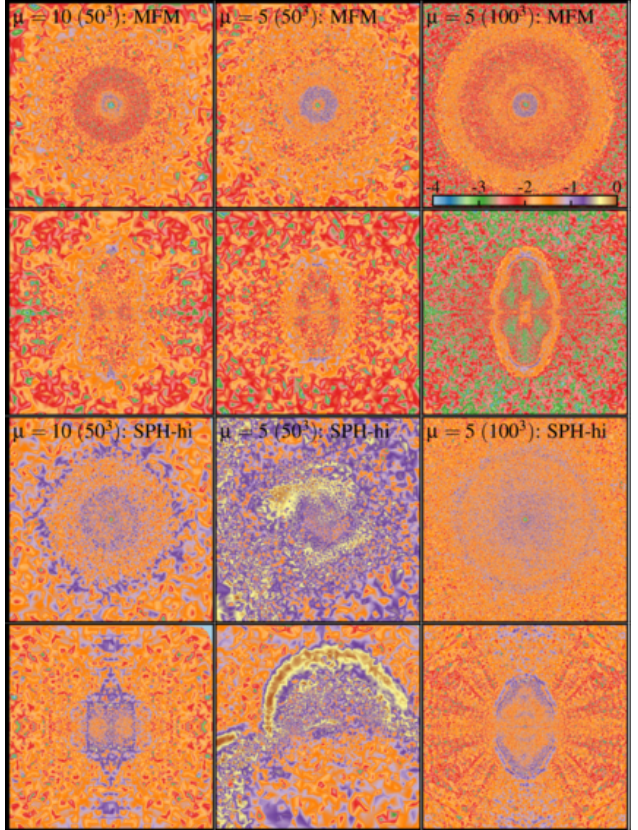


Figure 31. Divergence errors for some of the protostellar core tests. We show face-on (*upper*) and edge-on (*lower*) slices as Figs. 25–30, for MFM (*top*; MFV is similar) and SPH-hi (*lower panel*). The unstable behavior in SPH at low resolution is clearly related to poor control of the $\nabla \cdot \mathbf{B}$ -errors. We show two μ values at 50^3 resolution and compare $\mu = 5$ at higher (100^3) resolution. In all cases $\nabla \cdot \mathbf{B}$ errors decrease with resolution.

stable and “kicked out” the protostars corresponds (in every case) to $h|\nabla \cdot \mathbf{B}|/|\mathbf{B}| \gg 1$. This is consistent with previous studies (Bürzle et al. 2011; Price et al. 2012). Because the $\nabla \cdot \mathbf{B}$ errors decrease with resolution, going to higher-resolution suppresses this and allows stable evolution of the jets.

3.12 MHD Zeldovich Pancake: Testing Cosmological MHD Integration & Extremely High Mach Number Shocks

We now consider an MHD Zeldovich pancake, following a single Fourier mode density perturbation in an Einstein-de Sitter space, to test the code’s ability to deal with cosmological integrations, small-amplitude perturbations, large Mach numbers, and anisotropic cell arrangements. We initialize a linear perturbation following Zel’dovich (1970), with parameters chosen to match Li et al. (2008), in a periodic box with side-length $L = 1$ and $\gamma = 5/3$. Assume the unperturbed fluid elements have uniform density with co-moving position q along \hat{x} as $z \rightarrow \infty$, then co-moving positions and fluid quantities at the initial redshift $z_i = 20$ of the simulation are $x = q - A \sin(kq)/k$, $\rho = \rho_0/(1 - A \cos(kq))$, $v_{\text{pec}} = -H_0 \sin(kq)/k$, where $A = (1 + z_c)/(1 + z_i)$, $k = 2\pi/L$, $\rho_0 = 3H_0^2/(8\pi G)$ the critical density, and $z_c = 1$ is the redshift of caustic formation. In our particular (arbitrary) code units, $H_0 \approx 0.18$, and the initial $u = 9.3 \times 10^{-8}$ and $\mathbf{B} = B_0 \hat{y}$ (comoving). We consider a weak and strong field case, with $B_0 = 1.25 \times 10^{-4}$ and 7.7×10^{-3} , respectively. These are rather unconventional units, but we note that the solution can trivially be rescaled; it depends only on the dimensionless parameters z_c and the initial $\beta = P_{\text{thermal}}/P_{\text{magnetic}}$.

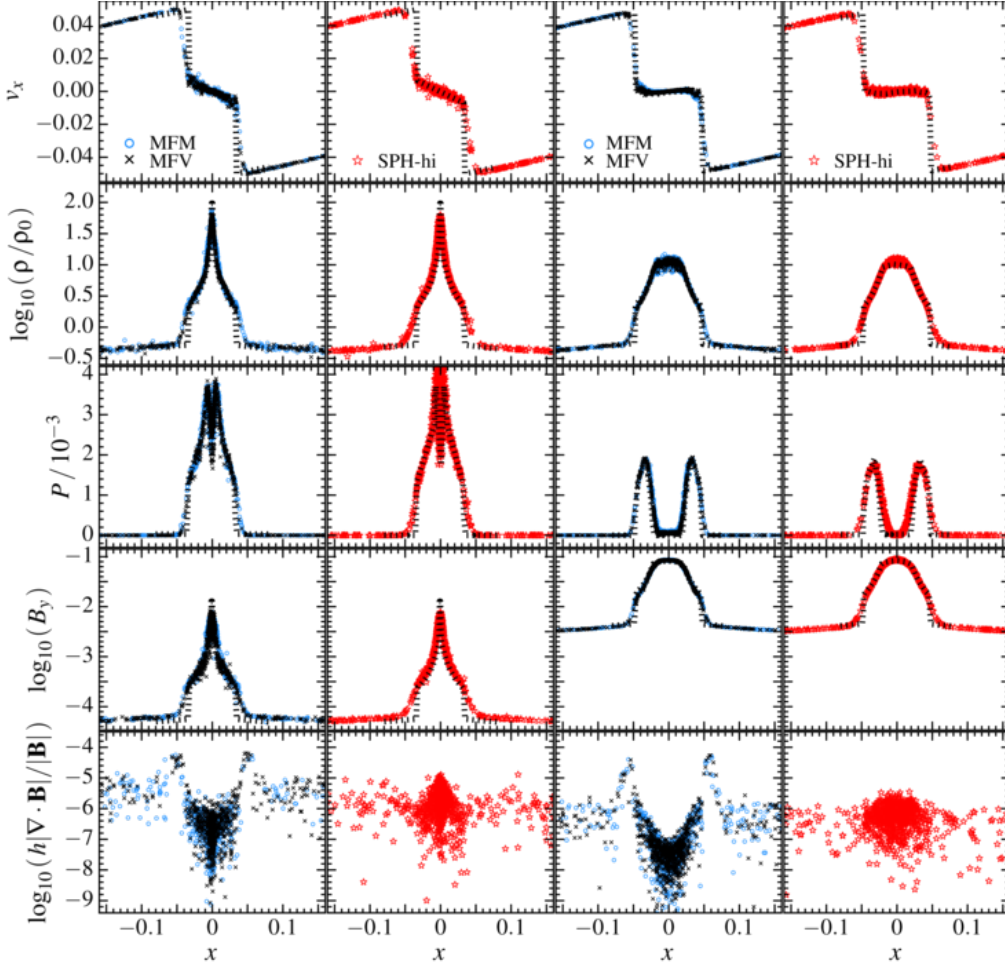


Figure 32. Magnetic Zeldovich pancake (§ 3.12) at $z = 0$. An initially small (linear) sinusoidal density perturbation collapses along one dimension (\hat{x}) in a 3D cosmological expansion, forming a caustic at $z = 1$, with a small initial perpendicular magnetic field $\mathbf{B} = B_0 \hat{y}$. We plot velocity in the collapse direction (v_x), density ρ (relative to the box-mean, ρ_0), pressure P , and field B_y . All cells/particles are plotted; the resolution is $\sim 100^3$. *Left:* Weak-initial field case. Here the results are similar to the pure-hydro case (see Fig. 30) in Paper I; B_y grows via compression in the center and declines adiabatically with the Hubble flow outside the shock. *Right:* Strong-initial field case. Here, the shock center is magnetically dominated, flattening the density peak and generating a pressure cavity. In both cases, MFM/MFV converge well to the exact solution (here, a 2048^3 -equivalent, one-dimensional grid-based PPM, CT calculation from ENZO) – a 1D, 512-element MFM calculation is indistinguishable from the exact solution. At lower (100^3) resolution, the outer, lower-density shock at $x = \pm 0.03$ is broadened by ~ 2 particles in the linear direction (about the same as obtained in second-order grid methods). The inner region, including the detailed shape of the central density and \mathbf{B} -field, are already well-converged. The shape and boundaries of the low pressure cavity in the strong-field case are well-resolved, but the lowest value of the *thermal* pressure converges slowly in the central region where $P_{\text{thermal}} \ll |\mathbf{B}|^2/2$ (i.e. where it is dynamically insignificant). In SPH, shocks are broadened by about twice as many particles in the linear direction, and the density peak shape converges slightly more slowly. The shape of the boundaries of the central pressure cavity in the strong-field case converge significantly more slowly than in MFM/MFV/grid codes. The $\nabla \cdot \mathbf{B}$ errors are negligible in this problem.

The perturbation should grow linearly along the \hat{x} direction under self-gravity, until it goes non-linear and eventually collapses into a shock (caustic) at $z = 1$.

At early times, the flow is smooth and obeys a known linear solution; we confirm that our MFM/MFV methods reproduce this with second-order convergence (even in cosmological integration with self-gravity coupled to MHD). In Fig. 32 we plot the results at $z = 0$. There are now clear strong shocks (pressure jumps of factors $\sim 10^8$) and factor ~ 1000 compressions. At various locations, the kinetic, thermal, and magnetic energy form an extremely disparate hierarchy: in the weak-field case $\rho |\mathbf{v}_{\text{ram}}|^2 \sim 10^{10} \rho c_s^2 \sim 10^{14} |\mathbf{B}|^2$, or in the strong-field case, $\rho |\mathbf{v}_{\text{ram}}|^2 \sim 10^9 |\mathbf{B}|^2 \sim 10^{15} \rho c_s^2$. As a result, Eulerian codes which evolve only the total energy almost invariably crash or produce unphysical results (e.g. subtraction of very large numbers giving negative pressures). The Lagrangian nature of our method greatly reduces these errors, and the dual-energy formal-

ism (Paper I; Appendix D) allow the method to deal smoothly with disparate hierarchies.

Another key aspect of the 3D test is that it involves highly anisotropic compressions: the gas collapses by a factor of ~ 1000 along \hat{x} , but there is no collapse in the other directions. We discuss this at length in Paper I: for AMR methods, this makes it very expensive to achieve the same resolution as our mesh-free methods, because (since grid cells are cubical), refinement must take place along the \hat{y} and \hat{z} dimensions with the collapse; for moving-mesh methods, it requires very careful and accurate cell refinement and regularization schemes (which can introduce other errors). But it is handled continuously and naturally in our mesh-free Lagrangian schemes. For the same total number of resolution elements, this allows our Lagrangian methods to achieve a factor ~ 10 better spatial resolution along \hat{x} in the central regions, compared to AMR (in 3D).

In the weak-field case, we confirm the results from Paper I:

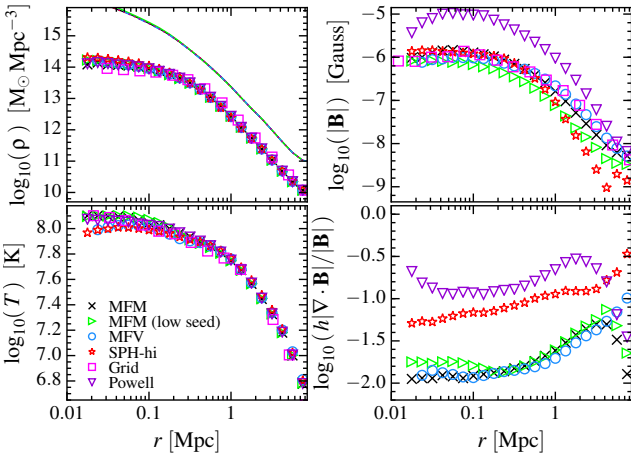


Figure 33. Magnetic Santa Barbara cluster (§ 3.13). A high-resolution sub-volume of a cosmological simulation is followed; it forms a cluster-mass dark matter halo; we show radially averaged profiles at $z = 0$. *Top Left:* Gas density (symbols) and dark matter density (lines). *Bottom Left:* Temperature. SPH shows slightly lower central- T (see Paper I). *Top Right:* Magnetic field. The central rms $|\mathbf{B}| \sim \mu\text{G}$, independent of the numerical method. With Powell-only cleaning, however, the magnetic energy is artificially amplified (as in the field loop problem) to order-of-magnitude excessive values. In SPH, excess artificial resistivity leads to some excessive damping at large radii. The “low seed” run features a seed field a factor $\sim 10^5$ weaker than the default run: the final \mathbf{B} is nearly independent of the seed. *Bottom Right:* Divergence errors. Absolute values in $|\nabla \cdot \mathbf{B}|$ are taken *before* averaging: the mean $|\langle h \nabla \cdot \mathbf{B} / |\mathbf{B}| \rangle| \sim 10^{-8}$ is approximately 6 orders of magnitude smaller. In MFM/MFV, the well-resolved ($< 1 \text{ Mpc}$) region maintains small divergence errors. In SPH the errors are factor ~ 5 larger.

the method can handle large energy hierarchies; arbitrarily strong shocks are resolved across ~ 2 linear cells/particles for MFM/MFV, and smeared across a factor $\sim 2 - 3$ larger range in SPH; co-moving integration with self-gravity is accurate; and because of their ability to handle asymmetric cell/particle distributions, the Lagrangian methods converge more rapidly in high-density regions compared to AMR. In the strong-field case, we also confirm that trace \mathbf{B} -fields are correctly amplified, and recover the correct jumps and rarefactions.

On this particular test, we obtain similar results with the Powell et al. (1999)-only divergence cleaning. The reason is that there is negligible field in the \hat{x} direction, and the growth of the perpendicular B_y component is driven by simple, effectively one-dimensional compression/expansion.

3.13 The MHD Santa Barbara Cluster: Cosmological MHD Integration in Turbulent Flows & Divergence-Control

Next we consider the MHD “Santa Barbara Cluster” from (Frenk et al. 1999); the hydrodynamic case is again in Paper I. The test is a “zoom-in” where we initialize a high-resolution Lagrangian region in a low-resolution Einstein-de Sitter cosmological background, which collapses to form an object of a rich galaxy cluster mass at $z = 0$. The cluster ICs are in Frenk et al. (1999); a periodic box of side-length $64 h^{-1} \text{ Mpc}$ is initialized at redshift $z = 49$, in a flat Universe with dark matter density $\Omega_{\text{DM}} = 0.9$, baryonic $\Omega_b = 0.1$, Hubble constant $H_0 = 50 \text{ km s}^{-1} \text{ Mpc}^{-1}$. The gas is non-radiative with $\gamma = 5/3$ and initial $T = 100 \text{ K}$. We add to this a trace initial seed field $\mathbf{B} = B_0 \hat{z}$. The initial \mathbf{B} direction and magnitude should be unimportant, provided it is small.

Fig. 33 shows the resulting profiles of density, temperature, magnetic field, and $\nabla \cdot \mathbf{B}$ at $z = 0$, across simulations using different methods (the average $|\mathbf{B}|$ and $h|\nabla \cdot \mathbf{B}|/|\mathbf{B}|$ values plotted in Fig. 33

are magnetic energy weighted averages). The grid result here is taken from high-order (PPM unsplit CTU) AMR simulations using CT in Miniati & Martin (2011). The dark matter density profile (essentially determined by the N -body solver) is nearly identical in all runs, as expected (as is the final pressure profile, given by hydrostatic equilibrium). There are some very small differences in the central gas density, temperature, and entropy; these are discussed extensively in Paper I.

In all methods, for a wide range of B_0 , \mathbf{B} is amplified to $\sim \mu\text{G}$ in the cluster core. In our “default” runs, we seed $B_0 = 10^{-8} \text{ G}$ ($4 \times 10^{-12} \text{ G}$ co-moving). This gives plasma $\beta \equiv P_{\text{gas}}/P_{\text{mag}} \geq 50$ everywhere in the ICs, so the magnetic pressure is unimportant. As long as this is true, the final \mathbf{B} profile is nearly independent of B_0 . We have verified this in all methods: for $B_0 \gtrsim 10^{-7} \text{ G}$, the initial $\beta \sim 1$ and the hydrodynamic properties (ρ, T) as well as maximum $|\mathbf{B}|$ begin to change. For sufficiently small B_0 , in practice, numerical resistivity and truncation errors will swamp the field and suppress growth: we obtain similar final \mathbf{B} profiles for minimum $B_0 \geq (10^{-14}, 10^{-11}, 10^{-9}, 10^{-12}) \text{ G}$ in (MFM, MFV, SPH, AMR), respectively. The fact that we can use such small minimum B_0 (comparable to roundoff errors) in MFM reflects the extremely low numerical dissipation of advected quantities inherent to the method. The large value in SPH reflects the artificial resistivity errors discussed above, whereby fields with $\beta \gg 100$ tend to be artificially over-damped. Even for $B_0 = 10^{-8} \text{ G}$, we already see some SPH over-damping in the cluster outskirts.

In MFM/MFV methods, $\nabla \cdot \mathbf{B}$ is well-controlled, with mean *absolute* values of $h|\nabla \cdot \mathbf{B}|/|\mathbf{B}| \approx 0.01$ in the resolved region of the cluster. The errors rise towards the outskirts owing to (1) decreasing resolution there, and (2) boundary effects (the setup of this “zoom in” involves no gas outside the initial Lagrangian region, so there are vacuum boundaries on one side of many particles). The median $h|\nabla \cdot \mathbf{B}|/|\mathbf{B}|$ is $\sim 10^{-4} - 10^{-3}$. In SPH, the errors are less well-controlled, reaching ~ 0.1 ; however this appears to have little or no effect on the solution.

With Powell-only cleaning, however, the field is artificially amplified to order-of-magnitude larger values in the cluster core; this is essentially the compounded version of the erroneous growth seen in the field loop test. This is qualitatively different from the behavior seen in any runs with cleaning, despite the fact that $h|\nabla \cdot \mathbf{B}|/|\mathbf{B}|$ (while large) is not much larger than our with-cleaning SPH runs. Once again, this emphasizes that in Powell-only cleaning, the *non-linear* error terms can integrate unstably (i.e. build coherently). In contrast, with a properly-applied Dedner et al. (2002) divergence-damping, these terms are stabilized and Tricco & Price (2012) show that the \mathbf{B} field cannot artificially self-amplify (rather, the sense of the errors will be to produce additional numerical dissipation, just like most other sources of error). So even if $\nabla \cdot \mathbf{B}$ is nominally the *same* over the course of a simulation, runs with Dedner et al. (2002) cleaning will avoid many of the more serious instabilities of Powell-only cleaning.

3.14 Simulated Galaxies: Testing Code Robustness in Multi-Physics Applications

We now consider a “stress test” of the methods here, adding magnetic fields to simulations of galaxies using state-of-the-art physics models. Specifically, we consider three initial conditions: (1) an isolated (non-cosmological) galaxy (with a pre-existing stellar disk and bulge, gas disk, and dark matter halo), designed to represent a starburst/M82-like system (model **Sbc** in Hopkins et al. 2012c, with a $1 \mu\text{G}$ seed field); (2) a cosmological “zoom-in” simulation of a dwarf galaxy (with $z = 0$ halo mass $10^{10} M_\odot$; model

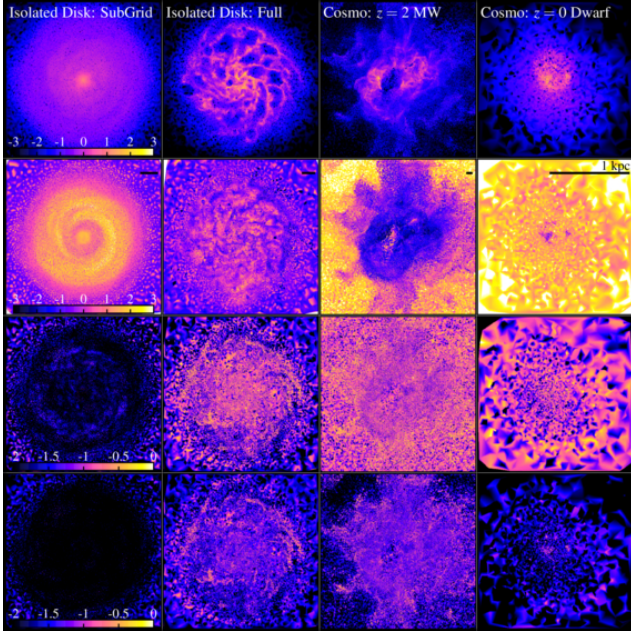


Figure 34. Galactic disk test (§ 3.14). We simulate a galaxy disk (gas, stars, and dark matter) with full self-gravity, star formation, cooling & gas chemistry, and stellar feedback/mass return in SNe, stellar winds, and radiation (photo-heating and radiation pressure). We consider four galaxy models: an isolated (non-cosmological) starburst disk, with either the sub-grid Springel & Hernquist (2003) “effective equation of state” model for the ISM (*left*; this does not explicitly treat the small-scale ISM turbulence and multiphase structure), or the “full” FIRE physics modules from Hopkins et al. (2014) (*second from left*; these explicitly treat the multi-phase, supersonically turbulent ISM), as well as a cosmological zoom-in simulation of a Milky Way mass galaxy run to $z = 2$ with the full FIRE physics (*second from right*; undergoing a major merger at this time), and a cosmological zoom-in of a dwarf with the FIRE physics (*right*; at $z = 0$). *Top:* Gas density $\log_{10}(n/\text{cm}^{-3})$, in a slice through the galaxy midplane, as labeled. *Second Row:* Plasma $\log_{10}(\beta)$ ($\beta \equiv P_{\text{thermal}}/P_{\text{magnetic}}$), in the same slice. The \mathbf{B} values reach approximate equipartition with the thermal+turbulent energy, producing a wide range in β . *Third Row:* Divergence error $\log_{10}(h|\nabla \cdot \mathbf{B}|/|B|)$. These are reasonably controlled but can reach local values $\gtrsim 10\%$, because particles are being re-arranged by gravity and feedback on timescales much faster than the fast magnetosonic “response time” for divergence-cleaning. *Bottom:* $\log_{10}(h|\nabla \cdot \mathbf{B}|/\sqrt{|\mathbf{B}|^2 + 8\pi P_{\text{thermal}}})$. This shows the divergence error relative to the total hydrodynamic pressure; here typical values are $\lesssim 10^{-2}$ – the large nominal values of $|\nabla \cdot \mathbf{B}|/|B|$ generally appear only in regions where the magnetic fields are dynamically irrelevant.

m10 in Hopkins et al. 2014, with a $10^{-10}\mu\text{G}$ seed field); and (3) a “zoom-in” of a Milky Way-like system, run to $z = 2$ (model **m12i** in Hopkins et al. 2014; $10^{-10}\mu\text{G}$ seed field). We intentionally study low-resolution versions of each – using a factor of ~ 64 fewer particles than the “production runs” in those papers – in order to maximize the numerical challenge. For each galaxy, we activate the full suite of physics from the FIRE (Feedback In Realistic Environments) simulations described in Hopkins et al. (2011, 2012b, 2013a) and Faucher-Giguere et al. (2015). This includes: self-gravity; gas cooling and chemistry; star formation; cosmological expansion; the interaction of gas, stars, and dark matter; energy, mass, momentum, and metal injection from supernovae and stellar winds; and radiation-matter interactions in the form of photo-ionization, photo-electric heating, and radiation pressure.

We emphasize that there is no simple “correct” solution for the \mathbf{B} -field evolution in these tests, and our concern here is not whether this particular model of the physics is correct or complete

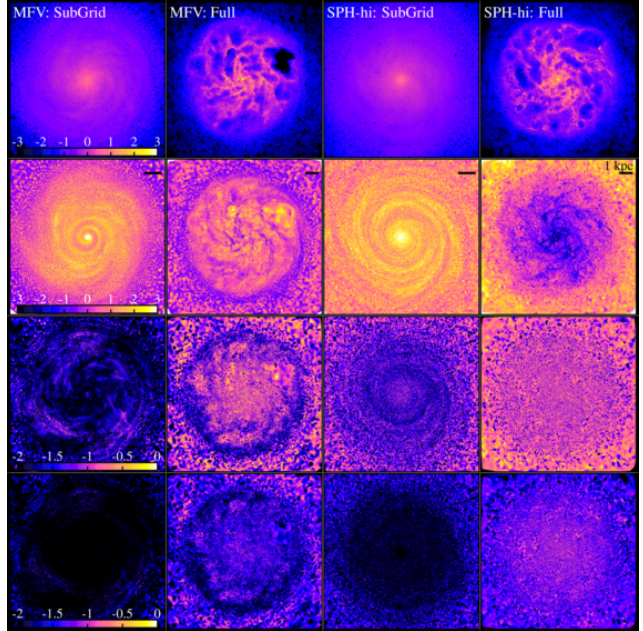


Figure 35. As Fig. 34, but for our MFV and SPH-hi methods. Here we just compare the isolated disk, with the simplified sub-grid (“smoothed ISM”) physics or “full ISM” (multiphase, turbulent) physics, as labeled. The gas density distributions, star formation rates, and galactic outflow rates are similar (for the same physics) in each method, although SPH predicts somewhat stronger/weaker fields in the inner/outer regions of the galaxy. SPH has larger divergence errors by a factor of $\sim 3 - 10$, consistent with our previous tests.

(we know, in fact, that these examples are under-resolved). Rather, we test (1) whether or not the algorithms we have developed can run (at all), without crashing or returning unphysical solutions; and (2) how well they control the divergence errors. This is extremely challenging: essentially every numerically difficult situation our test problems have considered above will occur here (and often be poorly-resolved). In addition, gas is discontinuously added & removed from the system (by stellar mass loss and star formation), and non-MHD forces (gravity and stellar feedback) are constantly re-arranging the particles/cells on timescales much faster than the local magnetosonic crossing times.

Fig. 34 shows the results for our MFM runs, and Fig. 35 compares MFV and SPH for a subset of the initial conditions. With the “full” FIRE physics, all the runs develop a multi-phase, supersonically turbulent medium, with strong galactic outflows (for details, see Hopkins et al. 2012a, 2013b,c). The \mathbf{B} fields are amplified to values in very rough equipartition with the thermal+turbulent energy of the disk: in cold molecular clouds ($T = 100\text{ K}$, $v_{\text{turb}} \sim 10\text{ km s}^{-1}$, $n \sim 10 - 10^3\text{ cm}^{-3}$), this implies $|\mathbf{B}| \sim 10 - 100\mu\text{G}$ and small plasma $\beta \sim 10^{-2}$, while in SNe-heated bubbles with $T \sim 10^7\text{ K}$ and $n \sim 0.01$ we find β as large as $\sim 10 - 100$. The algorithms are stable under arbitrarily long integration.

In general, we find that $\nabla \cdot \mathbf{B}$ is reasonably well-controlled, with mean values of $h|\nabla \cdot \mathbf{B}|/|B| \sim 0.03 - 0.1$ in MFM/MFV, and somewhat larger $\sim 0.1 - 0.2$ in SPH. Although still within this range, the errors are clearly larger in our cosmological zoom-in runs. This owes to two facts: they are less well-resolved, and they are less dynamically relaxed systems (being perturbed by mergers, accretion, etc). However, we stress that these relatively high values of $h|\nabla \cdot \mathbf{B}|/|B|$ are totally dominated by the regions where the magnetic fields are dynamically irrelevant (i.e. where $|\mathbf{B}|$ is small). In these regions, the fields are passive, and our divergence cleaning

scheme has essentially no time to “respond” to the constant, super-sonic, turbulent particle rearrangement. We therefore instead plot $h|\nabla \cdot \mathbf{B}|/\sqrt{|\mathbf{B}|^2 + 8\pi P_{\text{thermal}}} = h|\nabla \cdot \mathbf{B}|/|\mathbf{B}|\sqrt{1+\beta}$, which compares the $\nabla \cdot \mathbf{B}$ error to the total MHD pressure (the relevant term for the MHD forces); here we see that the errors are actually well-controlled at the $\lesssim 10^{-2}$ level. It is also worth noting that, like in Pakmor et al. (2011), the errors are “locally offsetting” – if we smooth/average the fields over a few neighboring particles, $|\nabla \cdot \mathbf{B}|$ rapidly vanishes.

We also compare a more simplified ISM/star formation model; this is the sub-grid Springel & Hernquist (2003) “effective equation of state” model. Here, the turbulence and phase structure of the ISM is not resolved, but replaced with a prescription which forms stars, kicks gas out of the galaxy in a “wind,” and pressurizes the gas such that certain large-scale properties can be recovered (this is the model used in popular large-volume simulations such as Illustris or EAGLE; Vogelsberger et al. 2013). By design, in these “sub-grid” models the small-scale phase structure and turbulence are smoothed over in the ISM (although the simulation still includes super-sonic motion, self-gravity, star formation, and galactic winds). With a smoother gas distribution, our divergence-control scheme does an excellent job maintaining errors $< 10^{-2}$. Compare this to Figs 13–15 in Pakmor & Springel 2012, who apply the Powell-only scheme to essentially the same problem in AREPO, and find mean errors $h|\nabla \cdot \mathbf{B}|/|\mathbf{B}| \approx 1$ (nearly independent of their resolution).

4 PERFORMANCE

In Paper I, we compare performance in terms of speed and memory usage, across MFM/MFV, our modern SPH-hi, and “bare-bones” SPH (the fastest but least accurate form of SPH, using no higher-order switches for diffusion, the simplest SPH forms of the hydrodynamic equations, and small neighbor numbers), and both moving-mesh and grid/AMR codes. Although performance is always problem-dependent, we found in general that speed (at fixed number of resolution elements) in MFM/MFV was comparable to (or slightly faster than) “bare-bones” SPH, and a factor of $\sim 1.5 - 2.5$ faster than SPH-hi, which is itself comparable to the speed of moving-mesh algorithms. The memory requirements are very similar across MFM/MFV/SPH-hi/SPH-lo, and substantially (factor ~ 2) lower than in moving-mesh or AMR methods.

In terms of zone-cycles per second, the MHD versions of the MFM/MFV/SPH algorithms are slower than the hydro-only algorithm by about $\approx 30\%$ (run time a factor of 1.3 larger), owing to the additional fluid quantities (and their gradients) which must be evolved and reconstructed (and extra terms in the Riemann solver/equation of motion).¹⁴ Compared to many other MHD implementations – particularly constrained-transport methods – this is extremely efficient: in ATHENA using CT the speed difference is a factor ≈ 2.3 (and in moving-mesh methods can be much larger; see Mocz et al. 2014a). The memory requirements of MFM/MFV/SPH are also somewhat higher in MHD compared to pure hydro, but only by the amount needed to carry the additional MHD quantities (\mathbf{B}, ψ), their gradients, and time derivatives.

Comparing performance across different MHD methods in our

¹⁴ To compare performance of the MHD algorithms, consider a simple test which essentially counts cycles per second. We initialize a 3D box with a standing linear wave of negligible fractional amplitude (10^{-6} ; just so the values of gradients, and solution of the Riemann problem, are not trivially vanishing), and evolve it for a short time. We consider a pure hydro case, and then add a trace magnetic field that does not alter the dynamics.

tests is non-trivial, because the non-linear dynamics are slightly different. But on all our tests, MFV and MFM are nearly identical in cost (MFV is systematically $\approx 5\%$ slower, owing to the need to calculate mass fluxes). If we consider an idealized, pure-MHD test and force identical timesteps (i.e. compare cycles per second), we find that MFM is only $\approx 5 - 10\%$ more expensive than SPH-lo (which requires no reconstruction or Riemann problem and uses the same neighbor number); however as in the hydro case, larger timesteps are allowed in MFM, so we actually find in our real runs that MFM is slightly *faster* than even SPH-lo and “bare-bones” SPH MHD with the same neighbor number. SPH-hi (with $N_{\text{NGB}} = 120$ in 3D), on the other hand, is a factor $\approx 2 - 2.5$ more expensive than MFM (because $\sim 4x$ as many neighbors are needed).

Even comparing complicated, highly non-linear problems with gravity, like the MHD Zeldovich pancake or Santa Barbara cluster, we find similar results. On these problems MFV is $\approx 10\%$ more expensive than MFM (the additional difference owes to variable particle masses in the gravity tree), and SPH-hi is a factor $\approx 2 - 2.5$ slower (for the same particle number). Furthermore, since we have shown that achieving the same accuracy in SPH requires significantly larger number of resolution elements (and convergence in SPH is slow), we conclude that, at fixed *accuracy*, our MFM/MFV methods are dramatically less expensive than SPH.

5 DISCUSSION

We have extended the mesh-free MFM and MFV finite-volume, arbitrary Lagrangian-Eulerian Godunov-type hydrodynamics methods from Paper I to include ideal MHD. We have implemented a second-order accurate, conservative formulation of these methods into our code GIZMO, together with state-of-the-art implementations of MHD in SPH. We systematically compared these methods to the results from grid codes and analytic solutions on a wide range of test problems, and find that the MFM and MFV methods are at least competitive with state-of-the-art grid MHD codes, and in many cases may have some advantages.

Critically, we find that our meshless methods can indeed capture phenomena like the MRI (with the correct growth rates and mode structure), formation of magnetically-driven jets in collapsing cores, MHD fluid-mixing instabilities (the Rayleigh-Taylor and Kelvin-Helmholtz instabilities), and both sub and super-sonic MHD turbulence. In fact we find convergence on these problems in our MFM/MFV methods is comparable to, and in some cases even faster than, AMR codes using constrained transport. This supports the similar conclusions found by Gaburov & Nitadori (2011), studying the MFV method on a smaller set of problems.¹⁵ Historically, these problems have been difficult for SPH; our new methods, however, do not suffer from the low-order errors that typically cause problems for SPH MHD. But we also show that even SPH, with the most current implementation of MHD, is able to capture most of these phenomena, albeit at the cost of larger kernels and some “by hand” adjustment of artificial dissipation parameters.

¹⁵ We note that our major extension of the work in Gaburov & Nitadori (2011) is to extend the methods to include (and test) the MFM method, as well as to conduct a systematic comparison with SPH and grid codes, on a wide variety of tests not considered in that paper. We have also made many subtle improvements of the MFV algorithm (all described here and in Paper I); these do not change the qualitative behavior on any tests, but do tend to decrease numerical noise.

5.1 The Divergence Constraint & Conservation

Most importantly, we find that, using a state-of-the-art implementation of the Dedner et al. (2002) divergence-cleaning scheme (re-discretized appropriately for our new methods), we are able to maintain $\nabla \cdot \mathbf{B} \approx 0$ to sufficient accuracy that divergence errors do not corrupt the solutions to any of our test problems. Typically, this amounts to a “worst-case” $h|\nabla \cdot \mathbf{B}|/|\mathbf{B}| \sim 0.01$ even in highly non-linear problems evolved for long times. In smooth flows and/or highly-resolved problems, more typical values are $h|\nabla \cdot \mathbf{B}|/|\mathbf{B}| \sim 10^{-4}$.

This is important: without any $\nabla \cdot \mathbf{B}$ correction, the MHD equations are numerically unstable, and most problems will either crash or converge to unphysical solutions. The simplest “fix” in the literature is to just subtract the unstable terms, the so-called Powell et al. (1999) or “8-wave” cleaning. However, we show that *the Powell cleaning alone converges to the wrong solution on most test problems*.

The problem is, in certain types of MHD discontinuities, Powell-cleaning alone produces the wrong jump conditions, even in the limit of *infinite* resolution, because the errors occur across a single resolution element and are zeroth-order. This has been shown before for a limited range of problems in fixed-grid codes; here we show the same applies to a wide range of problems in *all* the methods considered here. In the Brio-Wu and Toth shocktubes, the shock jump conditions are wrong, the same problem leads to *qualitatively* incorrect features appearing in MHD blastwaves (less dramatic versions of these errors appear in both the Orszag-Tang vortex and MHD rotor). In advection of a magnetic field loop, the field strength can grow unstably – the same errors disastrously corrupt the non-linear growth of the MHD Rayleigh-Taylor and Kelvin-Helmholtz instabilities, and lead to *orders-of-magnitude* incorrect growth of seed fields in cosmological MHD turbulence (e.g. the Santa Barbara cluster test). In the protostellar jet test, associated momentum errors can “kick” the core out of its disk.

With a good implementation of divergence-cleaning, we find that all of these errors are eliminated, provided that converged solutions are considered. This is clearly critical to almost any interesting astrophysical problem. Unfortunately, it means that a huge range of previous MHD studies, which relied only on the simpler Powell-type schemes, need to be revisited.

It is worth noting that, of the tests we explore here, a combination of the MRI, protostellar jet launching, magnetic Santa Barbara cluster, and non-linear magnetic Rayleigh-Taylor instability, appear to be the most challenging to *simultaneously* capture accurately. By comparison, many MHD methods papers focus only on a subset of problems like the MHD rotor, Orszag-Tang vortex, and shocktubes, which we find comparatively “easy” and not as useful.

5.2 MFM vs. MFV vs. Moving-Mesh Methods

In all of our tests, we find small differences between our meshless finite-volume (MFV) and meshless finite-mass (MFM) methods; those (minimal) differences are similar to what we saw in pure hydrodynamics tests in Paper I. MFV, with mass fluxes, is able to more sharply capture contact discontinuities and minimize overshoot in the density/velocity fields around them. However, the additional fluxes lead to enhanced “grid noise,” so the method is slightly more noisy.

In practice, the differences are sufficiently small that the “better” method will depend on the problem. For some purposes (e.g. cosmological simulations), it is extremely useful to maintain approximately constant particle/cell masses (because the dynamics

are dominated by gravity in an N -body solver); this is accomplished more elegantly and significantly more accurately with MFM than with MFV plus cell splitting/merging (which is more analogous to an AMR-type code). But in other cases, high resolution might be desired in low-density regions of the flow, in which case MFV (possibly used in the mode where cells do not move exactly with the fluid velocity) is more natural.

We have not presented a detailed comparison with moving-mesh codes, because a public moving-mesh MHD code capable of running the tests here is not available; however, a few of the test problems here have been considered in other studies with the moving-mesh codes AREPO, TESS, and FVMHD3D (Duffell & MacFadyen 2011; Pakmor et al. 2011; Gaburov et al. 2012). In each of these cases the results are very similar to ours here (especially similar to our MFV method). This is consistent with our extensive hydrodynamic comparison in Paper I, and expected, given that the methods are closely related.

Most importantly, on all tests both MFM/MFV methods exhibit good convergence properties and capture all of the key qualitative phenomena, even at relatively poor resolution.

5.3 Comparison to SPH MHD

Historically, it has been very difficult to capture non-trivial MHD phenomena with SPH. However, in the last few years there have been tremendous improvements to almost every aspect of the basic hydrodynamic algorithms in SPH, as well as the specific discretization of MHD (see references in § 1). As a result, we find that state-of-the-art SPMHD is, in fact, able to capture most of the important MHD phenomena studied here, including non-linear MRI, dynamo effects, magnetic jet launching, and fluid mixing instabilities.

However, convergence in SPH is still very slow; in almost every case, SPH is still significantly more noisy, less accurate, and more diffusive at fixed resolution compared to our MFM/MFV methods, and requires some “by hand” tweaking of numerical parameters to give good results on all tests. There are two fundamental problems: first, SPH requires “artificial diffusion” (viscosity, conductivity, resistivity) terms, which are somewhat ad hoc. The resistivity term in particular is challenging, as discussed in § 3.9: the correct “signal velocity” and question of whether resistivity should be applied at all is much less clear than, say, artificial viscosity, as it depends on the type of MHD discontinuity (not just whether one is present). We are unable to find a single “switch” the works best for all cases, and we show that using an even slightly less-than-ideal choice (e.g. using the magnetosonic versus Alfvén speeds for the resistivity signal velocity) can catastrophically corrupt certain problems (such a fluid mixing instabilities and/or jet launching). Similar conclusions were reached in Tricco & Price (2013). Second, and more fundamental, SPH has low-order errors which can only be suppressed by increasing the neighbor number in the kernel. This leads to an effective loss of resolution and higher diffusivity. However not increasing the neighbor number to some very large value ($\gg 100$ in 3D) leads to disastrously large errors and noise in most of our test problems. Similar problems are well-known in the pure-hydro case (see Paper I), but they are much more problematic in MHD, because of how they interact with the artificial resistivity and divergence cleaning terms. Kernel-scale noise seeded by the low-order errors produces magnetic divergences, which are then subtracted off and damped away, potentially corrupting the real solution (and preventing the algorithm from identifying “real” divergence errors). For this reason, the typical $\nabla \cdot \mathbf{B}$ errors and numerical diffusion are ~ 2 orders of magnitude larger in SPH (even

with > 100 neighbors) compared to MFM/MFV methods (with just 32).¹⁶

Still, provided sufficiently high resolution and large kernel neighbor number are used, together with care in choosing the artificial diffusion parameters specific to the problem, we conclude that “modern” SPH MHD can produce accurate solutions. And SPH MHD may still have some limited advantages in specific contexts. The artificial diffusion operators are wholly operator-split from the hydrodynamic operators; this is usually problematic, but when there are extreme energy hierarchies between kinetic, magnetic, and thermal energies, it ensures that small errors in any of the three terms do not directly appear in the others. It can handle free surfaces trivially and maintain numerical stability with vacuum boundaries; however the MHD equations will not be correct at these boundaries (the zeroth-order errors become order-unity, although they are numerically stable). And it remains the most computationally simple method we study.

5.4 Comparison to AMR

In all cases, our new mesh-free methods (MFM/MFV) appear competitive with state-of-the-art grid-based codes (e.g. third-order PPM methods, with constrained transport, and CTU-unsplit integration, as in ATHENA). We find no examples where there are qualitative phenomena that either method cannot capture, nor any examples where we cannot converge to similarly accurate solutions. Of course, there are quantitative differences in the convergence rates, and errors at fixed resolution, which depend on the method. Despite the fact that Eulerian codes can use CT-methods to maintain the divergence constraint, we identify several problem classes in which convergence is faster in our Lagrangian methods than in AMR.

Not surprisingly, these tend to be problems where advection, angular momentum conservation, self-gravity and/or following large compressions are important – these are the obvious areas where Lagrangian methods have an advantage. For example, we see significantly faster convergence on the field-loop advection problem (our MFM/MFV methods produce about the same numerical dissipation as grid methods at 4^D -higher resolution, where D is the number of dimensions.) The mesh-free algorithms are robust to arbitrary “boosts,” which degrade the non-moving grid solutions on problems with mixing and/or contact discontinuities (e.g. the Rayleigh-Taylor and Kelvin-Helmholtz instabilities, Orszag-Tang vortex, MHD rotor, and blastwave/explosion problems). The errors caused by these boosts are, of course, resolution-dependent (and will converge away in grid codes), but this means that convergence to a desired accuracy on these problems is usually faster in our MFM/MFV methods than in grid-based methods, if the fluid is being advected at super-sonic velocities. This difference also means our new methods are robust to arbitrary velocities in the current sheet test (while some stationary-grid methods will crash for modestly super-sonic motion around the sheet). Perhaps most dramatically, the protostellar core collapse/MHD jet problem combines high-dynamic range collapse, self-gravity, and evolution of a

¹⁶ Note that some authors have attempted to control the noise in SPH MHD by performing operations only on “re-smoothed” quantities (see Dolag & Stasyszyn 2009; Stasyszyn et al. 2013). This is similar in spirit to increasing the kernel size, and similarly leads to a loss of resolution and increase in numerical diffusion. But it is not clear whether the discretized equations after re-smoothing actually consistently represent the true hydrodynamic equations (they are not, mathematically, the Lagrangian-derived SPH equations), so it remains unclear whether such methods can actually converge (at any resolution) to the correct solution.

global thin disk (angular momentum conservation) – as a result, convergence is much faster in MFM/MFV than in AMR methods. Qualitative phenomena (e.g. the jet momentum/mass) start to converge at resolutions as low as 10^4 cells/particles, compared to at least $0.3 - 1 \times 10^7$ cells in AMR (“effective” resolutions of $\gtrsim 20,000^3$).¹⁷ And the resolution demands become more severe in AMR if the disk is rotated and/or moving with respect to the coordinate axes: like in Paper I with a simple Keplerian disk problem, this requires $\gg 512^3$ resolution in AMR in the disk for good behavior, plus a comparable number of elements along the jet, to prevent it from numerically grid-aligning (artificially bending) and being destroyed. In contrast, our new methods are trivially invariant to such rotations and boosts, at any resolution.

Of course, on other problems, grid methods converge more rapidly. In smooth, pressure-dominated flows, the “grid noise” is minimized in truly fixed-grid (non-AMR) methods, so convergence in the highly sub-sonic regime (Mach numbers $\lesssim 0.01$) is usually faster. On shock-tube type problems (e.g. the Brio-Wu & Toth problems above), where our errors are dominated by the noise introduced by divergence-cleaning and non-zero $\nabla \cdot \mathbf{B}$ errors, we see significantly faster convergence in grid-based codes that can use constrained transport to eliminate these errors entirely (a similar factor $\sim 4^D$ as above). And of course, by virtue of *not* being Lagrangian, in high-dynamic range problems Eulerian codes will better-resolve low-density regions of the flow.

In short, we see no “inherently” superior method between AMR and our new mesh-free methods, simply differences in the accuracy achievable at fixed resolution or computational cost, which are highly problem-dependent.

5.5 Areas for Improvement & Future Work

This is a first study, and there are many potential areas for improvement. Several possibilities discussed in Paper I (more accurate quadrature rules, generalizing to higher-order fluid reconstructions, better-optimized kernel functions) apply as well to the MHD case.

The most dramatic improvement to the meshless methods here, however, would come from incorporating constrained transport. Recently, Mocz et al. (2014a) demonstrated that constrained transport could be successfully incorporated into moving-mesh algorithms; there is no conceptual reason why the algorithm described there cannot be applied to our MFM/MFV methods, since they are conservative finite-volume schemes with a well-defined set of effective “faces” and a partition of unity. In contrast, there is no clear way to generalize this to SPH (given the inherent zeroth-order inconsistency in SPH derivative operators, it is not clear whether it is possible under any circumstances to derive a CT-SPH method). However, the method in Mocz et al. (2014a) has not yet been extended to three dimensions and to adaptive timesteps, in a efficient manner which can run in competitive time. Therefore we have not

¹⁷ It is a common mistake to refer to “kernels” in mesh-free methods as “resolution elements” the same way single-cells are referred to in grid codes. This is wrong. In our MFM/MFV methods, the correct identification is to think of each particle as equivalent to a cell in a grid code (with about the same “effective resolution per cell/particle”). The kernel represents the number of neighbors in causal contact for hydrodynamics; so the correct analogy is to the *stencil* used in a grid code (number of neighbors with adjacent faces, plus those needed for gradient calculations). Our default choice for MFM/MFV, then, of ≈ 32 in 3D, is actually quite similar to what is obtained in moving Voronoi-mesh, AMR, and higher-order (PPM) Cartesian grid codes.

considered it here, but it is certainly worthy of more detailed exploration in future work.

Absent a complete CT implementation, some progress might be made using locally divergence-free gradient representations, or (similarly) vector potentials. Previous efforts have been made in this area in both SPH MHD and discontinuous Galerkin methods (see e.g. Miyoshi & Kusano 2011; Mocz et al. 2014b; Stasyszyn & Elstner 2015). These can offer some improvements; however, they usually sacrifice consistency and/or conservation, and by only providing locally divergence-free terms, it is by no means clear that they actually reduce the relevant errors driving numerical instability. But again, further study is needed.

In SPH, some errors (e.g. the zeroth-order errors) are inherent to the method. Others, however, could be decreased. There has been considerable work on improved switches for the artificial viscosity; similar work is needed for the artificial resistivity. In particular, it would greatly expand the flexibility of the method if a switch were devised which could correctly interpolate between the relevant propagation speeds of the resistivity (which depends on the type of MHD discontinuity).

ACKNOWLEDGMENTS

We thank Paul Duffell, Jim Stone, Evgenii Gaburov, Ryan O’Leary, Romain Teyssier, and many others for enlightening discussions and the initial studies motivating this paper. Support for PFH was provided by the Gordon and Betty Moore Foundation through Grant #776 to the Caltech Moore Center for Theoretical Cosmology and Physics, an Alfred P. Sloan Research Fellowship, NASA ATP Grant NNX14AH35G, and NSF Collaborative Research Grant #1411920. Numerical calculations were run on the Caltech compute cluster “Zwicky” (NSF MRI award #PHY-0960291) and allocation TG-AST130039 granted by the Extreme Science and Engineering Discovery Environment (XSEDE) supported by the NSF.

REFERENCES

- Abel, T. 2011, MNRAS, 413, 271
 Agertz, O., et al. 2007, MNRAS, 380, 963
 Arnold, V. I., Zeldovich, Y. B., Ruzmaikin, A. A., & Sokoloff, D. D. 1981, Soviet Physics JETP, 54, 1083, also: Zh. Eksp. Teor. Fiz. 81, 2052-2058.
 Balsara, D. S., & Spicer, D. S. 1999, Journal of Computational Physics, 149, 270
 Barnes, J. E. 2012, MNRAS, 425, 1104
 Bate, M. R., Tricco, T. S., & Price, D. J. 2014, MNRAS, 437, 77
 Børve, S., Omang, M., & Trulsen, J. 2001, ApJ, 561, 82
 Brio, M., & Wu, C. C. 1988, Journal of Computational Physics, 75, 400
 Bürzle, F., Clark, P. C., Stasyszyn, F., Dolag, K., & Klessen, R. S. 2011, MNRAS, 417, L61
 Cullen, L., & Dehnen, W. 2010, MNRAS, 408, 669
 Cunningham, A. J., Frank, A., Varnière, P., Mitan, S., & Jones, T. W. 2009, ApJS, 182, 519
 de Val-Borro, M., et al. 2006, MNRAS, 370, 529
 Dedner, A., Kemm, F., Kröner, D., Munz, C.-D., Schnitzer, T., & Wesenberg, M. 2002, Journal of Computational Physics, 175, 645
 Dehnen, W., & Aly, H. 2012, MNRAS, 425, 1068
 Dilts, G. A. 1999, International Journal for Numerical Methods in Engineering, 44, 1115
 Dolag, K., & Stasyszyn, F. 2009, MNRAS, 398, 1678
 Duffell, P. C., & MacFadyen, A. I. 2011, ApJS, 197, 15
 —. 2012, ApJ, 755, 7
 Evans, C. R., & Hawley, J. F. 1988, ApJ, 332, 659
 Faucher-Giguere, C.-A., Hopkins, P. F., Keres, D., Muratov, A. L., Quataert, E., & Murray, N. 2015, MNRAS, 449, 987
 Frenk, C. S., et al. 1999, ApJ, 525, 554
 Fromang, S., Hennebelle, P., & Teyssier, R. 2006, A&A, 457, 371
 Gaburov, E., Johansen, A., & Levin, Y. 2012, ApJ, 758, 103
 Gaburov, E., & Nitadori, K. 2011, MNRAS, 414, 129
 García-Senz, D., Cabezon, R. M., & Escartín, J. A. 2012, A&A, 538, A9
 Guan, X., & Gammie, C. F. 2008, ApJS, 174, 145
 Hahn, O., Teyssier, R., & Carollo, C. M. 2010, MNRAS, 405, 274
 Hawley, J. F., & Stone, J. M. 1995, Computer Physics Communications, 89, 127
 Hennebelle, P., & Fromang, S. 2008, A&A, 477, 9
 Hopkins, P. F. 2013, MNRAS, 428, 2840
 —. 2014, MNRAS, in press, arXiv:1409.7395
 Hopkins, P. F., Cox, T. J., Hernquist, L., Narayanan, D., Hayward, C. C., & Murray, N. 2013a, MNRAS, 430, 1901
 Hopkins, P. F., Keres, D., Murray, N., Hernquist, L., Narayanan, D., & Hayward, C. C. 2013b, MNRAS, in press, arXiv:1301.0841
 Hopkins, P. F., Keres, D., Murray, N., Quataert, E., & Hernquist, L. 2012a, MNRAS, 427, 968
 Hopkins, P. F., Keres, D., Onorbe, J., Faucher-Giguere, C.-A., Quataert, E., Murray, N., & Bullock, J. S. 2014, MNRAS, 445, 581
 Hopkins, P. F., Narayanan, D., & Murray, N. 2013c, MNRAS, in press, arXiv:1303.0285
 Hopkins, P. F., Quataert, E., & Murray, N. 2011, MNRAS, 417, 950
 —. 2012b, MNRAS, 421, 3522
 —. 2012c, MNRAS, 421, 3488
 Lanson, N., & Vila, J.-P. 2008a, SIAM J. Numer. Anal., 46, 1912
 —. 2008b, SIAM J. Numer. Anal., 46, 1935
 Li, S., Li, H., & Cen, R. 2008, ApJS, 174, 1
 Liu, M., Xie, W., & Liu, G. 2005, Applied Mathematical Modelling, 29, 1252
 Luo, H., Baum, J. D., & Löhner, R. 2008, Journal of Computational Physics, 227, 8875
 Maron, J. L., & Howes, G. G. 2003, ApJ, 595, 564
 Maron, J. L., McNally, C. P., & Mac Low, M.-M. 2012, ApJS, 200, 6
 McNally, C. P., Lyra, W., & Passy, J.-C. 2012, ApJS, 201, 18
 Mignone, A., Bodo, G., Massaglia, S., Matsakos, T., Tesileanu, O., Zanni, C., & Ferrari, A. 2007, ApJS, 170, 228
 Mignone, A., & Tzeferacos, P. 2010, Journal of Computational Physics, 229, 2117
 Miniati, F., & Martin, D. F. 2011, ApJS, 195, 5
 Miyoshi, T., & Kusano, K. 2005, Journal of Computational Physics, 208, 315
 —. 2011, Plasma and Fusion Research, 6, 1124
 Mocz, P., Vogelsberger, M., & Hernquist, L. 2014a, MNRAS, 442, 43
 Mocz, P., Vogelsberger, M., Sijacki, D., Pakmor, R., & Hernquist, L. 2014b, MNRAS, 437, 397
 Monaghan, J. J. 1997, Journal of Computational Physics, 136, 298
 —. 2000, Journal of Computational Physics, 159, 290
 Morris, J. P. 1996, Publications of the Astronomical Society of Australia, 13, 97
 O’Shea, B. W., Bryan, G., Bordner, J., Norman, M. L., Abel,

- T., Harkness, R., & Krutsuk, A. 2004, eprint, arXiv:astro-ph/0403044
- Pakmor, R., Bauer, A., & Springel, V. 2011, MNRAS, 418, 1392
- Pakmor, R., & Springel, V. 2012, MNRAS, in press, arXiv:1212.1452
- Powell, K. G., Roe, P. L., Linde, T. J., Gombosi, T. I., & De Zeeuw, D. L. 1999, Journal of Computational Physics, 154, 284
- Price, D. J. 2008, Journal of Computational Physics, 227, 10040
- Price, D. J., & Bate, M. R. 2008, MNRAS, 385, 1820
- Price, D. J., & Monaghan, J. J. 2005, MNRAS, 364, 384
- . 2007, MNRAS, 374, 1347
- Price, D. J., & Rosswog, S. 2006, Science, 312, 719
- Price, D. J., Tricco, T. S., & Bate, M. R. 2012, MNRAS, 423, L45
- Read, J. I., & Hayfield, T. 2012, MNRAS, 422, 3037
- Read, J. I., Hayfield, T., & Agertz, O. 2010, MNRAS, 405, 1513
- Ritchie, B. W., & Thomas, P. A. 2001, MNRAS, 323, 743
- Rosswog, S., & Price, D. 2007, MNRAS, 379, 915
- Ryu, D., & Jones, T. W. 1995, ApJ, 442, 228
- Saitoh, T. R., & Makino, J. 2009, ApJL, 697, L99
- . 2013, ApJ, 768, 44
- Shin, M.-S., Stone, J. M., & Snyder, G. F. 2008, ApJ, 680, 336
- Springel, V. 2005, MNRAS, 364, 1105
- Springel, V. 2010, MNRAS, 401, 791
- Springel, V., & Hernquist, L. 2002, MNRAS, 333, 649
- . 2003, MNRAS, 339, 289
- Stasyszyn, F. A., Dolag, K., & Beck, A. M. 2013, MNRAS, 428, 13
- Stasyszyn, F. A., & Elstner, D. 2015, Journal of Computational Physics, 282, 148
- Stone, J. M., Gardiner, T. A., Teuben, P., Hawley, J. F., & Simon, J. B. 2008, ApJS, 178, 137
- Swegle, J. W., Hicks, D. L., & Attaway, S. W. 1995, Journal of Computational Physics, 116, 123
- Teyssier, R. 2002, A&A, 385, 337
- Tiwari, S., & Kuhnert, J. 2003, in Lecture Notes in Computational Science and Engineering, Vol. 26, Meshfree Methods for Partial Differential Equations, ed. M. Griebel & M. Schweitzer (Springer Berlin Heidelberg), 373–387
- Toro, E. F. 1997, Riemann solvers and numerical methods for fluid dynamics : a practical introduction (Berlin, New York: Springer)
- . 1999, Riemann solvers and numerical methods for fluid dynamics: a practical introduction, 2nd edn. (Springer Berlin Heidelberg), xix + 624
- Tóth, G. 2000, Journal of Computational Physics, 161, 605
- Tricco, T. S., & Price, D. J. 2012, Journal of Computational Physics, 231, 7214
- . 2013, MNRAS
- van Leer, B. 1984, SIAM Journal on Scientific and Statistical Computing, 5, 1
- Vogelsberger, M., Genel, S., Sijacki, D., Torrey, P., Springel, V., & Hernquist, L. 2013, MNRAS, in press, arXiv:1305.2913
- Wadsley, J. W., Veeravalli, G., & Couchman, H. M. P. 2008, MNRAS, 387, 427
- Whitehurst, R. 1995, MNRAS, 277, 655
- Zel'dovich, Y. B. 1970, A&A, 5, 84
- Zhu, Q., Hernquist, L., & Li, Y. 2014, ApJ, in press, arxiv:1410.4222

APPENDIX A: THE SMOOTHED-PARTICLE MHD IMPLEMENTATION IN GIZMO

As noted in the text, the magnetic terms in our implementation of SPMHD follows that in the series of papers by Tricco & Price (2012, 2013). The full SPH hydrodynamics algorithms in GIZMO are given explicitly in Paper I. This includes both our implementation of “traditional” SPH and “modern” PSPH. We note that the additions for MHD are independent of whether TSPH or PSPH is used, but we will adopt the modern PSPH formulation as our “default.”

With the hydrodynamics in place, the additions for MHD in SPH are as follows. First, note that we directly evolve the conservative quantities \mathbf{VB} and $m\psi$, as in the MFM and MFV methods. This has several advantages over explicitly evolving \mathbf{B} and ψ – namely, it improves the overall conservation properties of the code, eliminates significant errors associated with compression/expansion of the particles/fluid elements, reduces noise from poor particle order, allows us to write several of the key equations in manifestly anti-symmetric form (allowing conservation to be maintained even under individual time-stepping), and greatly simplifies some of the hydrodynamic calculations. We see no advantage, in *any* test in this paper, in directly evolving \mathbf{B} in SPH, and many advantages to the \mathbf{VB} approach. With this in mind, the primitive variables \mathbf{B} and ψ are constructed in SPH from the conserved variables as follows:

$$\mathbf{B}_i \equiv \frac{(\mathbf{VB})_i}{V_i} \equiv \frac{\bar{\rho}_i}{m_i} (\mathbf{VB})_i \quad (A1)$$

$$\psi_i \equiv \frac{(m\psi)_i}{m_i} \quad (A2)$$

$$\bar{\rho}_i \equiv \sum_j m_j W(\mathbf{x}_i - \mathbf{x}_j, h_i) \quad (A3)$$

where $\bar{\rho}_i$ is the usual SPH density estimator (constructed from neighbors, hence distinct from the actual density field evaluated at the position of particle i in our MFM/MFV methods).

The conserved variable (\mathbf{VB}) is evolved according to:

$$\frac{d(\mathbf{VB})_i}{dt} = \sum_j \frac{m_i m_j}{\Omega_i \bar{\rho}_i^2} (\mathbf{v}_j - \mathbf{v}_i) (\mathbf{B}_i \cdot \nabla_i W_{ij}(h_i)) \quad (A4)$$

$$+ \sum_j (\mathbf{B}_i - \mathbf{B}_j) \frac{m_i m_j (\alpha_i^B + \alpha_j^B) c_{ij}^B}{(\bar{\rho}_i + \bar{\rho}_j)^2} \delta W_{ij} \quad (A5)$$

$$+ \sum_j m_i m_j \left[\frac{\psi_i}{\Omega_i \bar{\rho}_i^2} \nabla_i W_{ij}(h_i) + \frac{\psi_j}{\Omega_j \bar{\rho}_j^2} \nabla_j W_{ij}(h_j) \right] \quad (A5)$$

$$\Omega_i \equiv 1 - \sum_j \frac{m_j}{\bar{\rho}_i} \left(W_{ij}(h_i) + \frac{|\mathbf{x}_{ij}|}{\nu} \frac{\partial W(|\mathbf{x}_{ij}|/h_i)}{\partial |\mathbf{x}_{ij}|} \right) \quad (A5)$$

$$\alpha_i^B \equiv \text{MIN} \left[\alpha_{\max}^B, \text{MAX} \left(\frac{h_i |\nabla \otimes \mathbf{B}_i|}{|\mathbf{B}_i|}, \alpha_{\min}^B \right) \right] \quad (A6)$$

$$|\nabla \otimes \mathbf{B}_i| \equiv \left[\sum_j \sum_k \left| \frac{\partial B_i^{(k)}}{\partial x_j} \right|^2 \right]^{1/2} \quad (A7)$$

$$\delta W_{ij} \equiv (\nabla_i W_{ij}(h_i) + \nabla_j W_{ij}(h_j)) \cdot \hat{\mathbf{x}}_{ij} \quad (A8)$$

$$c_{ij}^B \equiv \text{MAX} \left[\frac{\alpha_c^B}{2} (v_{A,i} + v_{A,j}), \frac{1 - \alpha_c^B}{2} (v_{ij}^{\text{fast}} + v_{ji}^{\text{fast}}) \right] \quad (A9)$$

$$(v_{ij}^{\text{fast}})^2 \equiv \frac{1}{2} \left[c_{s,i}^2 + v_{A,i}^2 + \sqrt{(c_{s,i}^2 + v_{A,i}^2)^2 - 4 c_{s,i}^2 v_{A,i}^2 (\hat{\mathbf{B}}_i \cdot \hat{\mathbf{x}}_{ij})^2} \right] \quad (A10)$$

Here $\mathbf{x}_{ij} \equiv \mathbf{x}_i - \mathbf{x}_j$, ν is the number of spatial dimensions, \otimes denotes the outer product, $\nabla \otimes \mathbf{B}$ is the $\nu \times \nu$ gradient matrix of

\mathbf{B}_i computed using our second-order consistent matrix gradient method (and $|\nabla \otimes \mathbf{B}|$ is the Frobenius norm of the matrix), $\hat{\mathbf{x}}$ is the unit vector $\mathbf{x}/|\mathbf{x}|$, v_{ij}^{fast} is the fast magnetosonic wave speed between particles, $c_{s,i}$ is the particle sound speed (usually computed as $c_{s,i} \equiv (\gamma P_i/\bar{\rho}_i)^{1/2}$), and v_A is the usual Alfvén speed.

The first term in $d(\mathbf{V}\mathbf{B})_i/dt$ is the induction equation. The precise form of this is derived *exactly* from the SPMHD Lagrangian; any other form will introduce errors in conservation and potential numerical instabilities (see Tricco & Price 2012). The Ω terms here and throughout are derived from the same Lagrangian approach following Springel & Hernquist (2002), and account for variations in the “smoothing length” h between particles.¹⁸

The second term in $d(\mathbf{V}\mathbf{B})_i/dt$ is the artificial resistivity (Price & Monaghan 2005). Just like artificial viscosity and conductivity in the pure hydrodynamic case (still present here), artificial dissipation terms are necessary in SPH for all hydrodynamic quantities to account for discontinuities. However unlike artificial viscosity, artificial resistivity is still needed in rarefactions to prevent numerical instability, so this term is always “active” between neighbors (independent of whether they are approaching or receding). The form here is motivated by (although significantly different from) the dissipation in a Riemann problem; the important aspect is the “switch” α^B , which one would like to have a large value when there is a sharp discontinuity in \mathbf{B} , and a vanishing value in smooth flows. This is approximately accomplished by using the switch proposed in Tricco & Price (2013): $\alpha^B \propto h |\nabla \otimes \mathbf{B}|/|\mathbf{B}|$. In Tricco & Price (2013), the authors show this is considerably more accurate, and less diffusive away from shocks, than the “standard” (constant- α^B) approach.¹⁹

Note that, in the artificial resistivity term, the appropriate “signal velocity,” c_{ij}^B , is ambiguous (the physically correct value depends on actually solving the relevant Riemann problem to determine the type of MHD shock). Tricco & Price (2013) adopt the mean fast magnetosonic speed, Price & Monaghan (2005) adopt the RMS Alfvén speed; here we adopt a compromise. When $v_A \gg c_s$, we find the Tricco & Price (2013) speed usually gives better results (the same conclusion they reached in their test problems). However, when $c_s \gg v_A$, and there is particle disorder (either because of motion induced by external forces or near discontinuities), the problem is that the zeroth-order SPH errors always seed non-trivial ($\sim 1\%$ -level) α_i^B , so even if there is a smooth, continuous gradient in \mathbf{B} , the resistivity is triggered and the magnetic fields are damped on a sound-crossing time. For some of the problems in this paper, for example the MHD RT and KH instabilities and the SB cluster, this suppresses the *mean* field by an order of magnitude, and leads to a qualitatively incorrect solution. This is remedied if a wavespeed which vanishes with $|\mathbf{B}|$ (e.g. a multiple of the Alfvén speed) is used. We therefore allow for the use of either wavespeed in principle, with the parameter α_c^B in Eq. A9, but adopt $\alpha_c^B = 1$ as our “default” (i.e. simply set c_{ij}^B to the mean Alfvén speed). However in

¹⁸ The functional form of the Ω terms is slightly different here versus in Tricco & Price (2012), because we use the particle number density n_i , rather than $\bar{\rho}_i$, to determine the SPH smoothing length, but this has almost no effect on our results in any test problem. The two formulations are identical if particle masses are equal, which is also usually the case.

¹⁹ We actually further improve on this formalism, by using our matrix-based gradients to determine $\nabla \otimes \mathbf{B}$. Just like with the higher-order artificial viscosity switches proposed in Cullen & Dehnen (2010), the use of second-order consistent gradients (as opposed to the zeroth-order inconsistent SPH gradient estimator) greatly improves the accuracy of the switch (helping it trigger in the “correct” locations).

the tests described in § 3.9, we consider $\alpha_c^B = 0$, i.e. setting c_{ij}^B to the mean fast magnetosonic speed.

The third term in $d(\mathbf{V}\mathbf{B})_i/dt$ is the divergence-cleaning term, $\propto \nabla \psi$. The particular functional form is again Lagrangian-derived; as pointed out in Tricco & Price (2012), this is especially important, since not just any form of the gradient estimator can be used. Rather, it is necessary to use one which operates in appropriate conjugate pairs with the gradients used for the $\nabla \cdot \mathbf{B}$ estimation and pressure-gradient (hydrodynamic force) operations, or else the resulting cleaning scheme will be numerically unstable, and simply fail to clean the “correct” divergences.

The conserved variable $(m\psi)$ is evolved according to:

$$\frac{d(m\psi)_i}{dt} = v_{\text{sig},i}^2 \sigma_h \frac{m_i}{\Omega_i \bar{\rho}_i} \sum_j m_j (\mathbf{B}_i - \mathbf{B}_j) \cdot \nabla_i W_{ij}(h_j) \quad (\text{A11})$$

$$- (m\psi)_i \frac{\sigma_p v_{\text{sig},i}}{f_{\text{kern}} h_i}$$

The first term in $d(m\psi)_i/dt$ is the corresponding source term for the divergence-cleaning field (the hyperbolic term). Again, the functional form inside the summation is strictly tied to the functional form of the cleaning in $d(\mathbf{V}\mathbf{B})_i/dt$.²⁰ The second term in $d(m\psi)_i/dt$ is the parabolic damping.²¹

In both of these, $v_{\text{sig},i}$ is the maximum signal velocity calculated between all neighbors, as described in the text. This signal velocity is modified compared to the standard hydrodynamic case by the replacement of the sound speed $c_{s,i}$ with the fast magnetosonic speed v_{ij}^{fast} between particles. That replacement applies for all places where the signal velocity appears – for example, in the artificial viscosity terms, and calculation of the CFL condition/timesteps.

The only remaining equation is the magnetic force:

$$\frac{d(m\mathbf{v})_i}{dt} \Big|_{\mathbf{B}} \equiv \sum_j m_i m_j \left[\frac{\mathbf{M}_i}{\Omega_i \bar{\rho}_i^2} \cdot \nabla_i W_{ij}(h_i) + \frac{\mathbf{M}_j}{\Omega_j \bar{\rho}_j^2} \cdot \nabla_i W_{ij}(h_j) \right] - \mathbf{B}_i \sum_j m_i m_j \left[\frac{\mathbf{B}_i}{\Omega_i \bar{\rho}_i^2} \cdot \nabla_i W_{ij}(h_i) + \frac{\mathbf{B}_j}{\Omega_j \bar{\rho}_j^2} \cdot \nabla_i W_{ij}(h_j) \right] \quad (\text{A13})$$

$$\mathbf{M}_i \equiv \frac{\mathbf{B}_i \otimes \mathbf{B}_i}{\mu_0} - \frac{|\mathbf{B}_i|^2}{2\mu_0} \mathbf{I} \quad (\text{A14})$$

where \mathbf{M} is the Maxwell stress tensor and \mathbf{I} is the identity matrix. The first term here is the usual MHD acceleration $d\mathbf{v}/dt \propto$

²⁰ Here we follow the “difference” formulation from Tricco & Price (2012), which they show provides the greatest stability and minimizes errors among the formulations they compare.

²¹ Note that, in closer analogy to grid-based methods, we evolve $(m\psi)$, and not, for example, $(V\psi)$ as in Tricco & Price (2012). This produces an essentially identical set of equations for the ψ evolution in SPH, except that we do not require the additional advection term

$$-\frac{(V\psi)_i}{2\Omega_i \bar{\rho}_i^2} \sum_j m_i m_j (\mathbf{v}_i - \mathbf{v}_j) \cdot \nabla_i W_{ij}(h_i) \quad (\text{A12})$$

in the evolution equation for $(V\psi)$ in Tricco & Price (2012). Like them, we found that this term does nothing to improve behavior on our tests, and can de-stabilize the cleaning procedure in simulations where the velocity divergence is large (e.g. cosmological runs); therefore, we prefer the $(m\psi)$ formulation. Also following Tricco & Price (2012), we have experimented with an artificial dissipation term for ψ . However, because in SPMHD there is no ψ flux, we find (as these authors did) that this produces no improvement in performance on any test problems here, and only increases the numerical diffusion.

$\rho^{-1} \nabla \cdot \mathbf{M}$; again, the particular functional form of the gradient operator derives necessarily from the SPH Lagrangian (see Price & Monaghan 2005; note it is essentially identical to the form of the Lagrangian-derived SPH hydrodynamic force in Springel & Hernquist 2002, with \mathbf{M} replacing the pressure P). The second term is the Børve et al. (2001) implementation of Powell 8-wave cleaning – namely, subtracting the unphysical part of the equation of motion proportional to $\nabla \cdot \mathbf{B}$. As in the main text, this is necessary to prevent catastrophic numerical instability (here in the form of the tensile instability).

There are now four numerical parameters that must be set: the artificial resistivity terms α_{\min}^B , α_{\max}^B , and the divergence-cleaning terms σ_p , σ_h . The divergence-cleaning parameters are discussed extensively in the text; we find a best compromise on all problems in this paper using the “default” values $\sigma_h = 1$, $\sigma_p = 0.1$. For the artificial resistivity terms, unless otherwise specified we take $\alpha_{\min}^B = 0.005$, $\alpha_{\max}^B = 0.1$. We have experimented extensively with these, and find these are best compromise values. The $\alpha_{\max}^B = 0.1$ choice follows Tricco & Price (2013); a much larger value (e.g. $\alpha_{\max}^B \sim 1$) completely diffuses away the fields in several of our test problems (e.g. the RT instability, MHD rotor, SB cluster, protostellar core collapse) and dramatically over-smooths shock jumps in others (e.g. the Zeldovich and Toth problems), leading to systematically incorrect solutions. But if $\alpha_{\max}^B \ll 0.1$, the method is incapable of properly capturing strong, magnetically-dominated shocks. The lower limit is less important; $\alpha_{\min}^B \ll 0.1$ is important to prevent excess diffusion that suppresses field growth in e.g. the proto-stellar disk problem, but $\alpha_{\min}^B > 0$ greatly reduces the noise and post-shock oscillations that seed low-order SPH errors.

This completes the SPMHD implementation.

APPENDIX B: COSMOLOGICAL INTEGRATION OF DIVERGENCE-CLEANING

The modifications in our code necessary for cosmological integrations are described in detail in Paper I. These are, for the most part, unchanged. As described therein, it is easy to show that if we define appropriate co-moving units, the cosmological expansion is automatically handled, and the Riemann problem is locally unchanged, provided we convert into physical variables before solving it. This is identical in MHD. For the magnetic field \mathbf{B} , we consider the co-moving field $\mathbf{B}_c = a^2 \mathbf{B}$, where $a = 1/(1+z)$ is the usual scale factor. This is invariant under pure adiabatic expansion in a Hubble flow in ideal MHD. Since we evolve the conserved variable $(V\mathbf{B})$, and the volume/length units are also co-moving, we simply have $(V\mathbf{B})_c = a^{-1} (V\mathbf{B})$. For the divergence-cleaning field ψ , the “correct” co-moving units are slightly more ambiguous; how ψ behaves in a Hubble-flow expansion actually depends on the ratio of timescales (whether, for example $c_s > v_A$, because ψ depends on the fastest wavespeed). We have experimented with simply assuming $\psi_c = a^3 \psi$ (the appropriate choice in the typical cosmological case, when either c_s or the inter-particle fluid velocity $|\mathbf{v}|$ is much larger than v_A), or $\psi_c = a^{5/2} \psi$ (appropriate if v_A dominates), or explicitly solving for the evolution terms from expansion; in practice we find this makes no detectable difference to any problem, since the physical ψ -field growth and decay time to respond to evolving $\nabla \cdot \mathbf{B}$ ($\sim h/c_h$, where h is a resolution element and c_h the fastest wave speed) is always vastly shorter than the cosmological expansion/Hubble time.

APPENDIX C: THE DAMPING SPEED

In § 2, we note that the divergence-wave is damped with a source term $(m\psi)_i / \tau_i$, where usually $\tau_i \equiv h_i / (\sigma_p c_{\tau,i})$ with $c_{\tau,i}$ the damping wave speed. There is no *a priori* obvious choice for this speed, and the ability of the scheme to damp divergence does not depend sensitively on the choice. Of course, much too large a value compared to other characteristic speeds in the problem will mean that ψ cannot grow (and therefore cannot remove divergences), while much too small a value can lead to a “lag” in the response of the cleaning to $\nabla \cdot \mathbf{B}$.

We have therefore considered a variety choices:

$$c_{\tau,i} = \frac{1}{2} v_{\text{sig},i}^{\text{MAX}} \quad (C1)$$

$$c_{\tau,i} = v_{f\psi,i} \equiv \sqrt{c_{s,i}^2 + v_{A,i}^2 + \left(\frac{2\psi_i}{v_{\text{sig},i}^{\text{MAX}}} \right)^2} \quad (C2)$$

$$c_{\tau,i} = v_{\text{fastest}} \equiv \text{MAX}_i \left[\frac{1}{2} v_{\text{sig},i}^{\text{MAX}}, \left(c_{s,i}^2 + v_{A,i}^2 \right)^{1/2} \right] \quad (C3)$$

$$c_{\tau,i} = f_{\text{kern}} h_i \tau_{\text{fastest}}^{-1} \quad (C4)$$

$$\tau_{\text{fastest}}^{-1} \equiv \text{MAX}_i \left[\frac{v_{\text{sig},i}^{\text{MAX}}}{2 f_{\text{kern}} h_i}, \frac{1}{f_{\text{kern}} h_i} \left(c_{s,i}^2 + v_{A,i}^2 \right)^{1/2} \right] \quad (C5)$$

$$c_{\tau,i} = \text{MAX} \left[\frac{1}{2} v_{\text{sig},i}^{\text{MAX}}, v_{f\psi,i}, \epsilon_h v_{\text{fastest}} \right] \quad (C6)$$

The first is the standard signal velocity $v_{\text{sig},i}^{\text{MAX}}/2$ (this is the default choice in SPH MHD). We find this works well in every problem here, although in some cases it produces excess dissipation of the fields because it operates too slowly for some subset of particles when ψ is very large (since the speed at which ψ can induce changes in \mathbf{B} is not accounted for with this velocity).

The second ($v_{f\psi,i}$) is the particle-based fastest-possible magnetosonic speed, with the additional term $2\psi_i/v_{\text{sig},i}^{\text{MAX}}$. This term can be thought of as representing the “potential magnetic energy” in the ψ field – while usually negligible compared to the Alfvén speed v_A , it is certainly possible, on some problems, that ψ grows until it reaches values $|\psi_i| \gg |\mathbf{B}|/|\mathbf{v}_{\text{sig}}|$ – this is clearly in the limit where damping of the ψ field is desired. Therefore we find this choice works much better than the pure magnetosonic speed. This choice works comparably well to $v_{\text{sig},i}^{\text{MAX}}$, but is less than ideal in some cases where the particles have super-sonic local approach velocities (not accounted for here).

The third choice (v_{fastest}) is the default choice in Dedner et al. (2002), namely the fastest wavespeed and/or signal velocity in the entire domain. This works well on idealized test problems – including almost all of the tests in this paper; however, it makes little sense for high-dynamic range problems like cosmological or galaxy/star formation simulations. In those cases the medium is highly multi-phase, so there is a huge range of local fastest wavespeeds, often in regions which are not even in causal contact. We therefore find that this produces too-efficient damping (hence less-efficient cleaning) in the slowly-evolving regions of these problems.

The fourth choice (τ_{fastest}) is similar to the maximum wavespeed v_{fastest} , but instead sets τ_i directly to the minimum across all particles (independent of whether they have small/large local volumes h_i). In a uniform-grid code this is identical to v_{fastest} . Here we find it works comparably well, again in idealized test problems, but has the same problems in inherently multi-scale problems.

The final choice, therefore, represents our best attempt at a “compromise” between these. We take the maximum of either the

signal velocity $v_{\text{sig},i}^{\text{MAX}}/2$, the local magnetosonic speed (plus ψ) $v_{f\psi,i}$, and some multiple with $\epsilon_h \ll 1$ of v_{fastest} . We adopt this as our default for all problems here, with $\epsilon_h = 0.01$. However we stress that *all* of our qualitative results are robust to any of the choices above for $c_{\tau,i}$ – we find only minor quantitative differences (in many of the test problems here, these are completely indistinguishable).

APPENDIX D: ADDITIONAL FLUX-LIMITERS FOR DIVERGENCE-CLEANING OPERATIONS

In Paper I we describe our slope-limiting procedure for reconstruction; the same is used here. However, in a couple of cases (e.g. the isolated galaxy disk and Santa Barbara cluster), some additional flux limiters greatly help in improving numerical stability. These are specific to the divergence-cleaning (ψ) terms, so do not directly affect our reconstruction of the physical quantities. They will alter how efficiently the $\nabla \cdot \mathbf{B}$ errors are cleaned; while this is important, it is not the only consideration for stability.

In particular, numerical instability can arise owing to the “mixing” terms between ψ and B which appear in the updated values $\bar{B}'_{x,ij}$ and $\bar{\psi}_{ij}$ in the Riemann problem (see Eq. 14). In the limit where there is large particle disorder (e.g. poorly-resolved, turbulent shocks) and the particles are being rapidly re-arranged by non-MHD forces, or if boundary particles are only able to find a couple of neighbors (if vacuum boundaries, which are not recommended for MHD, are used) then one can have $|\psi| \gg v_{\text{sig}}^{\text{MAX}} |\mathbf{B}_i|$ and the implicit instantaneous update of B ($\sim (\psi_L - \psi_R)/c_h$) in the Riemann problem can be unstable (since small residuals in ψ which are not completely damped by the time particles locally re-arrange can lead to large changes in \bar{B}).

One solution would be to simply drop these terms. However, this prevents the divergence-cleaning from acting across single-particle discontinuities, which (as discussed in the text) can lead to incorrect jumps. We find a more accurate, robust, and flexible solution, which works well for all problems in this paper, is to simply apply an additional set of limiters for ψ .

In the Riemann problem, we modify Eq. 14 to be:

$$\bar{B}'_{x,ij} = \frac{1}{2} (B'_{x,L} + B'_{x,R}) + \frac{\alpha_{\psi,ij}}{2 \tilde{c}_{h,ij}} (\psi_L - \psi_R) \quad (\text{D1})$$

$$\bar{\psi}_{ij} = \frac{1}{2} (\psi_L + \psi_R) + \bar{\psi}_{ij}^B \quad (\text{D2})$$

$$\begin{aligned} \bar{\psi}_{ij}^B &\equiv \alpha_{\psi,ij} \frac{\tilde{c}_{h,ij}}{2} (B'_{x,L} - B'_{x,R}) \\ \alpha_{\psi,ij} &\equiv \text{MIN} \left[1, \alpha_{\psi}^0 \frac{\tilde{c}_{h,ij} |B'_{x,L} + B'_{x,R}|}{|\psi_L - \psi_R|} \right] \end{aligned} \quad (\text{D3})$$

This is a flux-limiter on the implicit 1D Riemann problem between B' and ψ at a discontinuity (or equivalently, we can think of it as limiting the slope of the ψ discontinuity). The coefficient α_{ψ}^0 should be < 1 for stability; the precise value is (like all limiters) set by a balance between stability and diffusion. Our experiments prefer $\alpha_{\psi}^0 = 0.75$. For the source terms for \mathbf{B} which are $\propto (V \nabla \psi)_i^*$

in Eq. 11, we also modify

$$(V \nabla \psi)_i^* \equiv - \sum_j \bar{\psi}_{ij} \mathbf{A}_{ij} \rightarrow (V \nabla \psi)_i^* + \alpha_{\psi,i}^B (V \nabla \psi)_{i,B}^* \quad (\text{D4})$$

$$(V \nabla \psi)_{i,0}^* \equiv - \sum_j \frac{(\psi_L + \psi_R)_{ij}}{2} \mathbf{A}_{ij} \quad (\text{D5})$$

$$(V \nabla \psi)_{i,B}^* \equiv - \sum_j \bar{\psi}_{ij}^B \mathbf{A}_{ij} \quad (\text{D6})$$

$$\alpha_{\psi,i}^B \equiv \text{MIN} \left[1, \frac{10 \zeta^2}{|(V \nabla \psi)_{i,B}^*|^2} \right] \quad (\text{D7})$$

$$\zeta \equiv \left| \frac{d(V \mathbf{B})_i}{dt_0} \right|^2 + \left| 0.1 \frac{0.5 v_{\text{sig},i} (V \mathbf{B})_i}{h_i} \right|^2 \quad (\text{D8})$$

where $d(V \mathbf{B})_i/dt_0$ represents the value of $d(V \mathbf{B})_i/dt$ calculated for element i including all other fluxes and source terms *except* $(V \nabla \psi)_{i,B}^*$. Similarly, in the source term for ψ (Eq. 11), $d\psi/dt \propto (V \nabla \cdot \mathbf{B})_i^* c_{h,i}^2$, we limit the effective value of $(V \nabla \cdot \mathbf{B})_i^*$ allowed to a maximum $= 100 V_i |\mathbf{B}_i|/h_i$. The pre-factor is of course arbitrary but should be $\gg 1$. Finally, we check each timestep whether $|\psi_i| > \alpha v_{\text{max}} |\mathbf{B}_i|$ with $\alpha = 10 \gg 1$ and $v_{\text{max}} = \text{MAX}(0.5 v_{\text{sig},i}, v_{\text{fastest}}, \sqrt{c_{s,i}^2 + v_{A,i}^2})$; if it exceeds this value, we impose $d\psi/dt = \text{MAX}(0, d\psi/dt)$ ($\psi < 0$) or $d\psi/dt = \text{MIN}(0, d\psi/dt)$ ($\psi > 0$). This just corresponds to increasing the (already arbitrary) ψ -damping rate super-linearly when ψ becomes very large.

Even in the Santa Barbara and galaxy disk problems, these limiters almost never act. Usually, when they do, the particles are in a situation (e.g. at vacuum boundaries) where the fluxes are unresolved and should not, in any case, be trusted. Therefore, the fact that this limiting procedure allows somewhat higher $\nabla \cdot \mathbf{B}$ errors (by making the ψ -based cleaning less aggressive) is a small price to pay for maintaining numerical stability.

APPENDIX E: A TWO-WAVE FORMULATION OF THE DIVERGENCE CLEANING TERMS IN THE RIEMANN PROBLEM

As discussed in the text, in Eq. 14, the normal component of \mathbf{B} and the divergence-cleaning term ψ are implicitly updated according to the solution of an independent one-dimensional Riemann problem, before solving the MHD Riemann problem. The solution given there assumes a single wavespeed $\tilde{c}_{h,ij} = \text{MAX}[v_{f,L}, v_{f,R}]$ (the maximum of the fast magnetosonic speed on left and right sides of the problem) for the divergence-cleaning wave at the discontinuity between the left and right states. Following a solution proposed by E. Gaburov (private communication), we could instead assume two independent wavespeeds, $c_L = v_{f,L}$ and $c_R = v_{f,R}$ on either side of the discontinuity. This yields the solution

$$\bar{B}'_{x,ij} = \frac{1}{c_L + c_R} [c_L B'_{x,L} + c_R B'_{x,R} + \psi_L - \psi_R] \quad (\text{E1})$$

$$\bar{\psi}_{ij} = \frac{1}{c_L + c_R} [c_R \psi_L + c_L \psi_R + c_L c_R (B'_{x,L} - B'_{x,R})] \quad (\text{E2})$$

This trivially reduces to the solution in Eq. 14 for $c_L = c_R$. We have considered this formulation, instead of the default in the text, for all test problems in this paper. In all cases, the differences are small. The two-wave formulation introduces some additional dissipation and/or grid noise, depending on the problem, however it is also more stable in situations with large particle disorder (essentially because it provides an up-wind weighting of the ψ and normal- \mathbf{B} terms).